A Computational modelling study of the catalytically active perovskite $LaCoO_3$

Saira Khan

Davy-Faraday Research Laboratory, The Royal Institution of Great Britain
Department of Chemistry, University College London

London, January 2007

A thesis submitted for the degree of Doctor of Philosophy

ProQuest LLC
789 East Eisenhower Parkway
P.O. Box 1346
Ann Arbor, MI 48106-1346

ABSTRACT

Atomistic and quantum mechanical computational modelling of the bulk and surface structures of the catalytically active perovskite $LaCoO_3$ have been undertaken to develop a better understanding of the processes involved during catalytic oxidation. Two catalytically important effects have been studied; firstly the creation of oxygen vacancies resulting from Sr^{2+} doping at the La^{3+} site or reduction of Co^{3+} and secondly substitution by Ce^{4+}at the La^{3+} site.

Bulk atomistic calculations were carried out using the GULP code to compare the Mott Littleton and supercell models. Results for the former, which represent the dilute defect case, suggested that, generally, for the various defect reactions studied, interactions between nearest neighbours determines structure stability as anticipated from simple electrostatic considerations. In contrast, the supercell calculations, which represent a higher concentration of defects, showed that interaction between defect clusters is also important. In addition, calculations for Ce doping confirmed that Ce has only limited solubility in bulk $LaCoO_3$.

However, since catalysis is a surface process the above defect calculations were repeated at the surface of $LaCoO_3$ using the MARVIN code. For the oxygen vacancy creation reactions, there is a general tendency that the smaller the cation defect-vacancy separation, the lower the energy of the cluster. In addition, there are clear indications that oxygen vacancies are more easily created at the surface than in the bulk. The results also confirm that the presence of defects strongly influences crystal morphology and surface chemistry. For cerium doping, computational modelling has shown that Ce is more soluble at the surface of $LaCoO_3$ compared to the bulk. This result has been discussed in terms of its impact both on low temperature, suprafacial and high temperature, intrafacial oxidation catalysis.

Quantum mechanical supercell simulations were carried out on bulk stoichiometric and oxygen vacancy containing $LaCoO_3$ using $DMol^3$ to study electronic effects. These bulk calculations showed that the low spin is favoured compared to the high spin. For the defect calculations the high spin ferromagnetic state was the most

favoured. These simulations have also shown that, in the presence of oxygen vacancies, electrons are localised on cobalt.

CONTENTS

List of Figures

CHAPTER 2

CHAPTER 3

CHAPTER 4

CHAPTER 5

CHAPTER 6

CHAPTER 7

CHAPTER 8

List of Tables

CHAPTER 2

CHAPTER 3

CHAPTER 4

CHAPTER 5

CHAPTER 6

CHAPTER 7

Copyright

Acknowledgements

First of all, I would like to thank my parents, my brother, sister-in-law, and my sister for their loving support throughout my education, whose continual affection and loving care are incalculable and have allowed me to attain this academic achievement. Thanks also to my husband and his family especially my mother-in-law, for both their emotional and practical support without which I would have been unable to cope sufficiently. Above all, I would like to thank my daughter for the happiness and joy she has bought to my life.

I dedicate this thesis to my beloved mother, Musarrat Ara Amjad (late) for the motivation and support she provided me to obtain this achievement.

There are many people who I wish to thank, many if not all for the following mixture of attributes and qualities; including their guidance, support, friendship, thoughts, criticism, truthfulness and honesty. The following list is not in any particular order of preference as you have all helped me in your own way. Firstly, I would like to thank Professor Richard Catlow, for the opportunity to do this PhD and for his valuable discussions and ideas, which have helped me throughout it. I would also like to give special thanks to Professor Richard Oldman for his unfailing guidance, support and friendship as my supervisor whose instruction and support provided me with a good understanding for my PhD. I would also like to express great thanks to Drs: Sam French, Alexei Sokol and Furio Cora for their interesting ideas, views and discussions throughout my time at the Royal Institution. As my PhD was a case studentship I would also like to thank Dr Sean Axon for his discussions and views, which helped me, progress my PhD. I would also like to give my heartfelt thanks to all my friends at the Royal Institution who were a great help throughout my PhD especially Misbah and Judy. Last but not least I'd like to thank Johnson Matthey and EPSRC for their generous grant.

CHAPTER 1

GENERAL BACKGROUND

Perovskites are a large family of crystalline ceramics that derive their name from a specific mineral known as perovskite. They are probably the most abundant minerals on earth and can be used for different applications such as magnetic, electric, optical, ferroelectric, piezoelectric, superconducting and catalytic.

The focus of this study is on catalysis and perovskite oxides are known to play a significant role in the use of heterogeneous catalysis, which has fundamental importance in the chemical industry and in other technologically relevant areas. For example, the oxidation of carbon monoxide (CO) to form carbon dioxide (CO_2) is the key reaction in car exhaust catalytic converters. This reaction was initially done by noble metals but this was very expensive. Therefore an alternative was required and it was shown that perovskites can be considered a good catalytic material as they can be synthesised at a lower cost and these oxides have a great catalytic activity to adsorb molecular oxygen at the surface and therefore encourage the oxidation of CO.

Nitrogen oxides are serious air pollutants, which are formed in many high temperature combustion processes including combustion engines. There has been a lot of research to suppress the release of these compounds in the atmosphere. This can be done by the catalytic reduction of NO using carbon monoxide or ammonia or by the catalytic decomposition of NO into nitrogen and oxygen, which is why perovskites are also important in exhaust gas depollution processes. Perovskites have been considered important alternatives to supported noble metals (Pt/Al_2O_3, Pt/SiO_2), since they are easier to synthesise and are thermally stable at high temperatures.

Catalytic combustion of methane is an alternative to conventional flame combustion, providing efficient energy generation and reducing harmful gas emissions. For wide implementation of this technology, thermally and mechanically stable catalysts are required. It is well known that perovskites exhibit high activity in methane combustion and simultaneously show high thermal stability (up to 1100°C). Catalytic

oxidation offers several advantages over thermal oxidation, since the oxidation reaction takes place 200-400°C lower. These advantages include: fuel economy resulting from lower operating temperatures, lower NO formation, and the economic and operational benefits of smaller and lighter units. Again perovskites are considered important because they are cheaper than precious metals.

The toxic emission of volatile organic compounds (VOCs) and halogenated volatile organic compounds (HVOCs) to the atmosphere from stationary and mobile sources constitutes a serious hazard to human health. They cause the formation of ozone and photochemical smog, which in turn damage agriculture, lakes and forests. Control of hazardous hydrocarbon emissions is amongst the highest priority. Currently, research efforts have been undertaken on the development of more efficient clean-up devices. Combustion technologies such as thermal and catalytic oxidation have an extensive history of providing reliable control of VOCs. For this application the thermal stability of perovskites becomes important.

Perovskites which can rapidly conduct oxygen ions (O^{2-}) can be used as solid electrolytes in a number of industrial applications including oxygen gas sensors, oxygen pumps, exhaust catalysts and solid oxide fuel cells (SOFC's). Recently these oxides have received attention as high temperature oxygen ion and proton conductors for use in electrochemical applications, hydrogen membranes and hydrogen sensors.

Perovskites are flexible systems as their properties may be adjusted or enhanced for specific applications by chemical doping. For example, Sr^{2+}doping at the La site in $LaCoO_3$ is used to enhance its ionic conductivity and catalytic performance by the creation of oxygen vacancies, which may influence oxygen adsorption and anion mobility. In this study, atomistic simulation and quantum mechanical techniques have been used to investigate bulk and surface defect calculations for one of the most important catalytically active perovskites $LaCoO_3$, with the aim of developing a better understanding of the role of oxygen vacancies in catalysis and the role of the cation dopant in modifying catalytic properties.

CHAPTER 2

2. PEROVSKITES AND OXIDATION CATALYSIS

Perovskites are important mixed oxides with many different uses including magnetic, electric, optical, ferroelectric, piezoelectric, superconducting and catalytic applications. These properties are critically dependent on the details of the perovskite structure[1]. Therefore, in this chapter, we will discuss the perovskite structure and identify the different possible defect structures, which can be created. We will then concentrate on oxidation catalysis, where initially the different mechanisms for catalytic oxidation will be explained and a brief description of oxygen adsorption and surface interactions will follow. Finally, we will briefly outline some experimental results for methane combustion, CO oxidation and ammonia oxidation.

2.1 Perovskite Structure

The ideal perovskite structure is cubic with space group $Pm3m$[2]. Its formula is ABX_3, where A is the larger cation, B is the smaller cation and X is the anion. In this structure the B cation is in the 6-fold and the A cation is in the 12-fold coordinated by the anion. **Figure 2.1** shows the structure with the A cation in the centre of the unit cell[2].

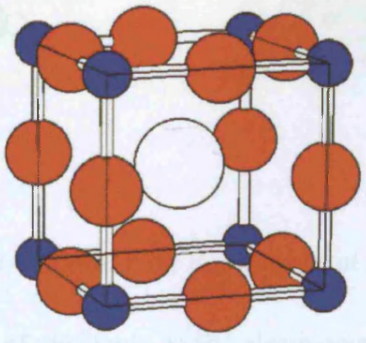

Figure 2.1 *Perovskite structure with the A cation (white) in the centre and the B cation (blue) at the corners of the unit cell and the anions (red)*[2].

The stability of the structure can be determined by a tolerance factor (t) defined by Goldshmidt from the sizes of the ions[3].

$$t = (r_A + r_x)/\sqrt{2}(r_B + r_x), \qquad (2.1)$$

where r_A, r_B and r_x are the radii for the respective cationic and anionic ions. t would be equal to 1 for the ideal cubic perovskite structure in a hard sphere model. Generally the majority of the t-values for perovskite structures are between $0.75<t<1.0$ with r_A >0.9Å and r_B>0.51Å[3].

For the ideal cubic structure t = 1, but when t deviates from 1 the structure is commonly distorted and the two most common distortions are rhombohedral and orthorhombic as in **Figure 2.2**[3]. For $0.9<t<1.0$ in the rhombohedral case the anions are displaced and there are slight distortions. Orthorhombic distortions and co-operative buckling of corner shared octahedra occur when $0.75<t<0.9$[3].

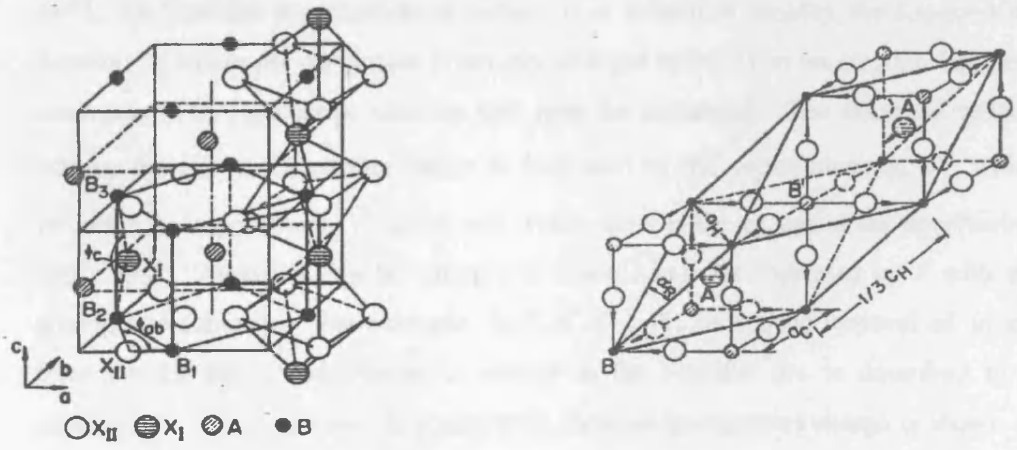

Figure 2.2 *(a) Orthorhombic distortion (b) Rhombohedral distortion*[3]

Apart from the influence of the ionic radii, electroneutrality is required for the stability of the structure, i.e. the sum of the charges of A and B must equal the total charge of the anions. In oxides, the different charge distribution of the ions can be in the form $A^{+1}B^{+5}O_3$, $A^{+2}B^{+4}O_3$ and $A^{+3}B^{+3}O_3$. The majority of the perovskites which have been used as high temperature proton conductors in hydrogen membranes and

hydrogen sensor technologies are of the $A^{+2}B^{+4}O_3$ type, for example $ACeO_3$ and $AZrO_3$ (A= Ba, Sr)[4,5]. $A^{+3}B^{+3}O_3$ perovskites, where A is typically La and B is a first row transition element such as Co, Fe or Mn, have important applications in solid oxide fuel cells as ionic conductors, ceramic oxygen membranes as well as heterogeneous catalysis, which will be the focus of this study.

2.2. Defect Structure

In a perfect crystal all the atoms occupy regular lattice sites in the crystal lattice, which can only occur at absolute zero[6]. At room temperature, crystals necessarily contain defects, which in a real system are also present due to impurities. Perovskites can be generally divided into two groups, stoichiometric and non-stoichiometric materials.

Non-stoichiometric structures can either be oxidative or reductive. These materials contain defects in the form of either lattice vacancies *(V)* or electron holes (*h*) or traps *(e)*[6]. To describe the creation of defects it is helpful to employ the Kroger-Vink notation in which *(h)* designates positively charged holes when an electron has been removed. The superscript notation will now be explained. The chemical species occupy the site in the perfect lattice as indicated by the superscript e.g. O_O^x which indicates an unperturbed O^{2-} lattice site where the x is the charge at the unperturbed lattice site. Vacancies can be cationic or anionic and are indicated by V with the appropriate subscript. For example, for $LaCoO_3$, V_{La} shows the removal of an ion from the La site. The change in charge at the specific site is described by a superscript. A unit decrease in positive (or increase in negative) charge is shown by the superscript '. So the notation for the removal of a *La* atom from the $LaCoO_3$ lattice is given by V_{La}'''. Similarly an oxygen vacancy involving the removal of an O^{2-} ion from the crystal is less negative (i.e. effected position) compared to the ideal structure, indicated by a superscript dot•, i.e. the oxygen vacancy is represented by $V_O^{\bullet\bullet}$[6].

Electron holes and traps involve a change in the charge of the lattice species which

can either be positive or negative. Therefore the change in charge from Co^{3+} to Co^{4+} can be indicated by $h_{Co}^{\bullet}$, . Similarly the change of Co^{3+} to Co^{2+} can be shown by $e_{Co}^{'}$, the latter can be described as an electron trap[6]. In the following sections we will discuss the examples of $LaMnO_3$ and $LaCoO_3$.

2.2.1 Oxidativative Non-Stoichiometric Perovskites

For oxidative non-stoichiometric compounds cation vacancies or oxygen interstitials need to be created. The cation vacancy can occur either at the A site or B site. Computational studies have shown that for $BaTiO_3$ the cation vacancy at the B site is energetically more favourable and therefore Ti vacancies are created[7]. However, for the $LaMnO_3$ structure it is more favourable to create $V_{La}^{\bullet}$ compared to $V_{Mn}^{'''}$ [7,8]. To balance the cation vacancy there needs to be oxidation either at the A or B site. For the La based perovskites it is energetically more favourable for the oxidation to occur at the B site. The oxidative non-stoichiometric structure can be represented as $La^{3+}Mn^{3+}/Mn^{4+}O_{3+\delta}$ showing the two oxidation states of the B cation and the oxygen content in the non- stoichiometrc perovskite (δ). Typically δ lies between +/- 0.1 spanning oxidative and reductive non-stoichiometry. This oxygen content can be changed by varying the O_2 partial pressure in contact with the perovskite at high temperatures. Thus Kamata *et al* showed that a sample composition of $LaMnO_{3.08}$ at 1200°C and a partial oxygen pressure of 10^{-5}Pa loses oxygen and becomes reductively non-stoichiometric $LaMnO_{2.95}$ at partial pressure of oxygen$10^{-6.65}$Pa [9].

2.2.2 Reductive Non-Stoichiometric Perovskites

For reductive non-stoichiometric compounds, oxygen vacancies are created (although cation involvement could in principle provide charge compensation), in response to the cations decrease in oxidation state or the introduction of dopants (see below)[10]. For example in $LaCoO_3$, La^{3+} is stable so the reduction in oxidation state occurs at the B site, i.e. Co preferentially changes from 3+ to 2+. For every oxygen vacancy, 2 Co^{2+} ions are needed. The reductive non-stoichiometric formula can be shown as $La^{3+}\ Co^{2+}/Co^{3+}O_{3-\delta}$. Reductive non-stoichiometry can be created by reducing the O_2 partial pressure in contact with the perovskite. The driving force for creating these non-stoichiometric compounds depends not only on the oxygen partial pressure but on

the redox characteristics of the B site transition metal [10].

2.2.3 Doping Perovskites

Defects can also be created by cation doping. Aliovalent doping at the A site causes a change in the average A site cation charge which is analogous to the B site redox process for example Co^{3+} to Co^{2+} in $LaCoO_3$. For example in $LaCoO_3$, doping Sr^{2+} at the La^{3+} site or reduction of Co^{3+} to Co^{2+} at the B site causes the creation of oxygen vacancies. In the same way, doping of a cation with a tetravalent cation (Ce^{4+}) at the La site is equivalent to the oxidation of the A site which can be counterbalanced by the reduction Co^{3+} to Co^{2+} at the B site.

ABO_3 perovskite structures are of considerable importance as their properties can be tailored to specific applications by subtle changes in chemical doping at the A or B cation sites, which leads to applications in areas ranging from ionic conductivity to heterogeneous catalysis, which will be discussed in detail in **Sections 2.2.3.1** and **2.2.3.2**. The cation dopants can either be divalent or tetravalent. In the following we will discuss divalent doping with Sr^{2+} and tetravalent doping with Ce^{4+} in $LaCoO_3$.

2.2.3.1 Divalent Doping

The most common divalent dopants are Ca or Sr which are substituted at the A site. Substitution of Sr^{2+} at the La^{3+} site can either be accompanied by generating oxygen vacancies or creating holes. The equations can be shown using the Kroger-Vink notation,

$$2MO + 2La_{La}^{x} + O_{O}^{x} \rightarrow 2M_{La}^{'} + V_{O}^{\bullet\bullet} + La_2O_3 \qquad (2.2)$$

$$2MO + 2La_{La}^{x} + 2Co_{Co}^{x} + \tfrac{1}{2}O_2 \rightarrow 2M_{La}^{'} + 2h_{Co}^{\bullet} + La_2O_3 \qquad (2.3)$$

where La_{La}^{x}, Co_{Co}^{x}, O_{O}^{x} are the unperturbed lattice ion sites,

MO is the dopant oxide

$M_{La}^{'}$ is the M^{2+} dopant at the La^{3+}site,

$V_{O}^{\bullet\bullet}$ is the O^{2-} lattice ion vacancy,

$h_{Co}^{\bullet}$ is the Co^{4+} hole

Using computational modelling, Islam *et al* revealed that doping $LaCoO_3$ with Sr at low levels under low partial pressures of oxygen leads to preferential creation of vacancies whereas at a high partial pressure of oxygen Co^{4+} becomes more favoured. At high Sr levels, $x \geq 0.4$ in $La_{1-x}Sr_x CoO_3$, Co^{4+} can also be formed. At low levels of Sr doping (<0.4) Islam *et al* have also considered the formation of O^- holes ($h_O^\bullet$) on Sr doping and have shown this to be less energetically favoured than either O vacancy or Co^{4+}formation. This process will also be oxygen partial pressure dependent[11].

$$2SrO + 2O_O^x + 2La_{La}^x + \tfrac{1}{2}O_2 \rightarrow 2Sr_{La}' + 2h_O^\bullet + La_2O_3 \qquad (2.4)$$

Modelling has also shown that as expected formation of B^{4+} depends on the identity of B, for example Mn favours formation of Mn^{4+}. The options for formation of compensating defects on doping with Ca or Sr are listed in **Table 2.1.**

2.2.3.2 Tetravalent Doping

The most commonly considered tetravalent dopant is Ce^{4+} at the A site. In principle M^{4+} doping at the A site can either generate electron traps (e.g. Co^{2+} in $LaCoO_3$) or A site vacancies i.e. $V_{La}^{\bullet\bullet\bullet}$. The equations for these processes are given by:

$$4MO_2 + 4La_{La}^x + 4Co_{Co}^x \rightarrow 4M_{La}^\bullet + 4e_{Co}' + 2La_2O_3 + O_2 \qquad (2.5)$$

$$3MO_2 + 4La_{La}^x \rightarrow 3M_{La}^\bullet + V_{La}''' + 2La_2O_3 \qquad (2.6)$$

where MO_2 is the dopant oxide,

La_{La}^x, Co_{Co}^x are the unperturbed lattice ion sites,

$M_{La}^\bullet$ is the M^{4+} dopant at the La^{3+} site ,

e_{Co}' is the Co^{2+} electron trap,

$V_{La}^{\bullet\bullet\bullet}$ is the La^{3+} lattice vacancy

As for divalent doping, the preferred defect compensation process will be oxygen partial pressure dependent. For low oxygen partial pressure Co^{2+} will be formed and for high partial pressure, La vacancy will be formed. The options for formation of compensating defects on doping with divalent or tetravalent at the A doping are

summarised in **Table 2.1**.

M^{2+} Dopant (eg Sr^{2+})	ABO_3	M^{4+} Dopant (eg Ce^{4+})
M^{2+} at the A site ($M_A^{'}$)		M^{4+} at the A site ($M_A^{\bullet}$)
	A^{3+}(A_B^x)	A^{3+} vacancy ($V_A^{'''}$)
B^{4+} hole ($h_B^{\bullet}$)	B^{3+}(B_B^x)	B^{2+}electron trap ($e_B^{'}$)
O^{2-} vacancy ($V_O^{\bullet\bullet}$)	O^{2-}(O_O^x)	

Table 2.1 *A site doping and defect structures for ABO_3*

Importantly, French *et al* have shown by atomistic computational modelling that the solubility of Ce in $LaCoO_3$ is not energetically favourable for either of the above processes[12]. This is attributed to the cation radius mismatch between Ce^{4+} (1.14Å) and La^{3+} (1.36Å). This is in accordance with a substantial body of experimental data, which shows free CeO_2 in Ce doped $LaCoO_3$ preparations. The calculations indicate that only 5% doping occurs accompanied by the filling of oxygen vacancies in $LaCoO_3$, which is normally slightly reductively non-stoichiometric which can be shown by the following equation[12]:

$$2La_{La}^x + 2CeO_2 + V_O^{\bullet\bullet} \rightarrow 2Ce_{La}^{\bullet} + O_O^x + La_2O_3 \qquad (2.7)$$

2.3 Catalysis

2.3.1 Introduction

Many heterogeneous catalytic processes involve oxide supported metals, for example, platinum metal particles on a silica or alumina support[13]. The platinum provides most of the catalytic activity and the silica is there to add mechanical strength to the catalyst and to allow dispersion of the platinum over a larger surface area to increase surface activity. However these catalysts are very expensive and perovskites can be used more cheaply as the active catalyst and simply as a support for a number of catalytic reactions. Perovskites are candidates for these heterogeneous catalytic reactions, in particular oxidation reactions such as methane or VOC combustion and ammonia oxidation, because of their high temperature stability, good catalytic activity

and the enhancement of properties by cation doping, particularly at the A site.

2.3.2 Mechanisms for Catalytic Oxidation

Voorhoeve *et al* proposed two different mechanisms by which catalytic oxidation can occur over perovskites, suprafacial and intrafacial mechanism[14]. At lower temperature, suprafacial mechanism the catalyst provides the atomic orbitals of the proper symmetry and energy to activate the reactant molecules. In this mechanism the reaction occurs between the adsorbed species on the surface. The suprafacial mechanism dominates at low temperatures (<500°C) when the mobility of lattice oxygen is low. The adsorption and desorption reactions, which occur in the suprafacial mechanism, are much faster than oxygen extraction from the lattice at these lower temperatures. Oxygen vacancies for example created by Sr doping, play a role and promote suprafacial activity through enhancement of oxygen adsorption as in **Figure 2.3a**[14].

In contrast, in the higher temperature intrafacial mechanism the catalyst participates in the reaction as a reagent being partially consumed and then regenerated in a continuous cycle. This cycle involves the removal of the oxygen from the lattice and the rate of oxidation is accelerated compared to the suprafacial catalytic reaction. The removal of the oxygen from the lattice is endothermic and therefore the intrafacial process only dominates at high temperatures, i.e. above 550°C when the mobility of lattice oxygen becomes significant[14]. The intrafacial process involving removal of the lattice oxygen is shown schematically in **Figure 2.3b**.

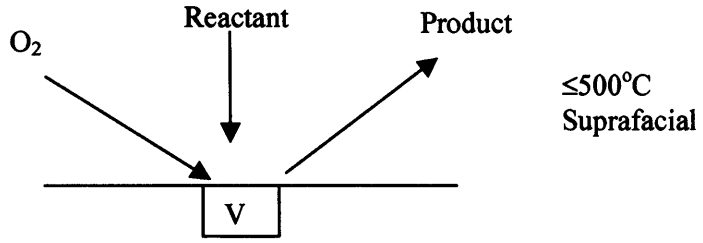

$$O_2(g) \Leftrightarrow O_2^-(chemisorbed)$$

Figure 2.3a *Schematic diagram for the suprafacial*[14]

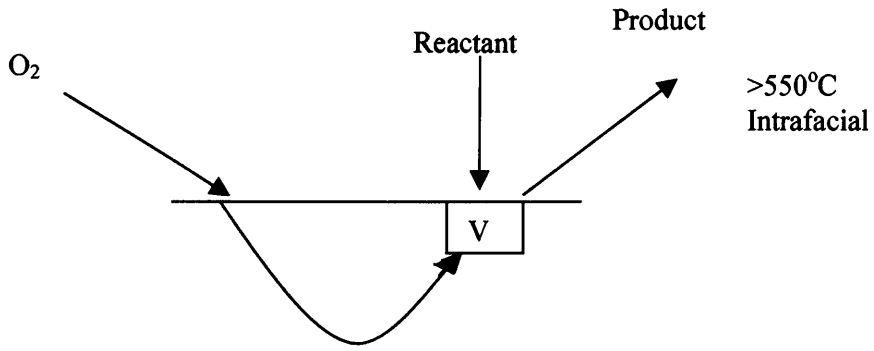

$$O^{2-}(bulk) \Leftrightarrow O^{2-}(nearsurface) \Leftrightarrow O^-(surface)$$

Figure 2.3 b *Schematic diagram for intrafacial mechanism*[14]

In the temperature range representing the transition from dominance by suprafacial catalysis to intrafacial, the mechanism can be envisaged as a process involving transport of oxygen across the surface as surface lattice oxygen becomes mobile[14].

2.3.3 Oxygen Adsorption and Surface Interaction

There are believed to be several different types of oxygen adsorbed species, including O_2 (adsorbed molecule), O (adsorbed neutral atom), O_2^- (superoxide) and O_2^{2-} (peroxide) which could be present on the catalyst surface. In their early work, Beilanski and Haber estimated energetics for different states in the gas, lattice and surface phases as shown in **Figure 2.4**[15]. The stabilities of these different oxygen ions have been estimated from the published values for dissociation energy of oxygen

and the electron affinity of the various oxygen ions in the gas phase combined with assumptions about the stabilization energies in the lattice and at the surface[15].

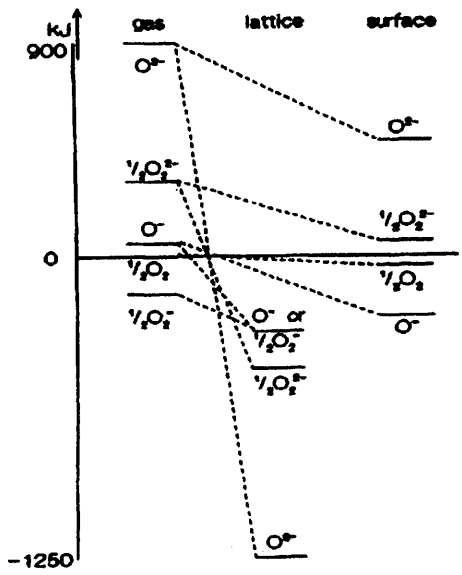

Figure 2.4 *Different oxygen species occurring in catalysis over oxides*[15].

In the gas phase, Beilanski and Haber have shown that the free superoxide ion (O_2^-) is the only ion, which is stable[15]. Thus it has been observed that at the surface it is the commonly adsorbed oxygen species. It only takes 10 kJ to create $2O^-$ ions from one molecule of O_2 (and two electrons) and O^- has indeed been observed as a surface species. The highest energy is required to form 2 oxide ions (O^{2-}), which is due to the high dissociation energy of the O_2 molecule and the strong electron affinity of the O^- ion. Thus O^{2-} is highly unstable in the gas phase[15].

The oxide ion O^{2-} becomes stabilized only in the crystal lattice by the electric field created by the neighbouring cations. Indeed, this stabilising Madelung energy is sufficient to make the oxide ion the most stable form of oxygen in the lattice[15].

Charged oxygen species at the surface also require stabilization energy. It is assumed that the stabilization energy at the surface relative to that in the lattice is roughly proportional to the number of cations coordinated to each oxide ion. Thus, in $LaCoO_3$ for example, the coordination number of oxide ions in the lattice is six and thus the stabilization energy of O^{2-} at the surface would be lower than the lattice. The adsorbate O^{2-} ion cannot appear at the surface. The different forms of ionic oxygen, which may be stable at the surface, are the superoxide ion O_2^- and the monoatomic O^- ion which have been postulated as the active species in suprafacial and intrafacial oxidation catalysis. More recently, the transformation of the oxygen species at the surface has been considered as a stepwise process;

$$O_{2(ads)} \rightarrow O_{2(ads)}^- \rightarrow O_{(ads)}^- \rightarrow O^{2-}{}_{(lattice)} , \qquad (2.8)$$

where the oxygen gradually becomes richer in electrons, which has also been presented schematically by Oldman[16]using ideas developed from the work of Wu *et al* as shown in **Figure 2.5**[17].

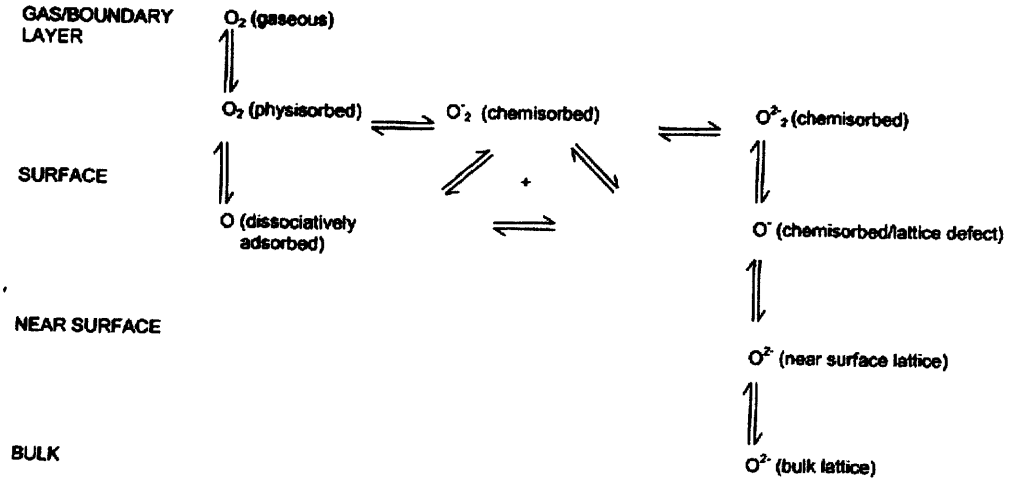

Figure 2.5 *Schematic diagram for the different oxygen states*[16].

The direct experimental evidence identifying different states of oxygen on the surface of $LaCoO_3$ is limited because of the difficultly in growing single crystals for the

application of surface science techniques such as Ultraviolet (UV), photoelectron spectroscopy (PES) and the problems encountered in electron paramagnetic resonance (EPR) spectroscopy due to the overlap of signals from the transition metals and oxygen species. However, some information has been obtained from techniques such as temperature programme desoprtion (TPD) and X-ray photoelectron spectroscopy.

TPD shows at least two kinds of oxygen with peaks at 300°C and 800°C for $LaCoO_3$ as shown in **Figure 2.6**. The peak at 250-300°C (designated as α_1) corresponds to surface adsorbed O_2, which is important at low temperatures in the suprafacial processes and may be associated with oxygen adsorbed at vacancies[18]. The peak at 800°C (designated by β), which corresponds to oxygen released from the lattice is accompanied by the reduction of the B atom e.g. Co^{3+} to Co^{2+}[18].

An additional peak has been detected at ~600°C in some work by Royer *et al* which has been designated as α_2 and is associated with the loss of O_2 adsorbed as O_2^- in oxygen vacancies as opposed to a proposed more loosely bound form possibly involving a triatomic state for the α_1 peak[19]. However, at this higher temperature, it could also be due to the loss of surface lattice oxygen as oxygen becomes mobile or subsurface adsorbed oxygen. Both α peaks are enhanced by creation of oxygen vacancies by Sr doping[20].

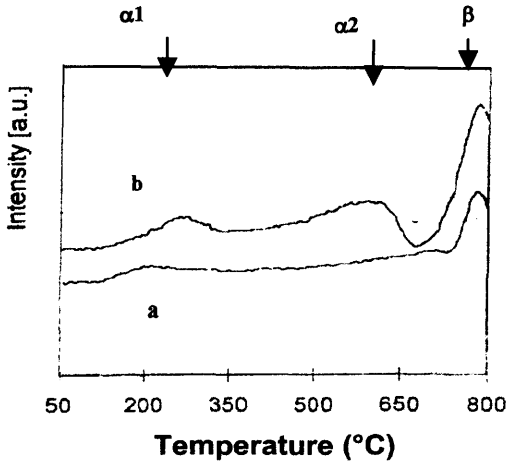

Figure 2.6 *TPD after treatment in $O_2 \geq 530°C$ (15min) and cooling to 50°C in O_2 for (a) $LaCoO_3$ and (b) $La_{0.8}Sr_{0.2}CoO_3$*[17,18,19].

TPD can reveal other processes, for example oxidative non-stoichiometry i.e. the removal of interstitially adsorbed oxygen at 300°C from the perovskite related material La_2NiO_4 and removal of the lattice oxygen at 750°C from $LaMnO_{3+\delta}$ which undergoes a phase transformation to stoichiometric $LaMnO_3$[21].

X-ray Photoelectron Spectroscopy (XPS) provides another technique to monitor different surface oxygen species experimentally[22]. XPS is highly surface specific due to the short range of photoelectrons that are excited from the solid. The electron binding energies (BE) of the peaks are characteristic of each element. The peak areas can give an indication of the quantitative composition of the surface material. XPS of $LaCoO_3$ shows two kinds of oxygen. The sharper, lower BE peak at 529eV is due to the lattice O^{2-} oxygen while the broader higher BE peak at 532eV corresponds to less electron rich adsorbed oxygen species such as O^-, O_2^-, or OH^-[22] as shown in **Figure 2.7.**

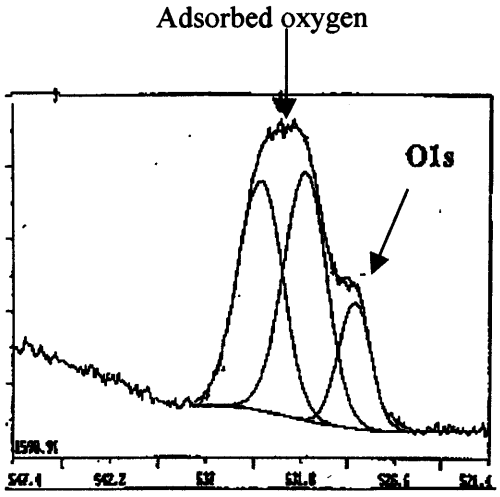

Figure 2.7 *XPS spectra for O 1s for $LaCoO_3$ to show the different surface oxygen states* [22].

XPS can reveal defects due to non-stoichiometry in perovskites[22]. For stoichiometric materials the intensity of the low BE lattice oxygen peak dominates. Reductive non-stoichiometric materials, which have a high fraction of oxygen lattice vacancies due to divalent cation doping, shows an increase in the intensity of high BE adsorbed oxygen.

Some clues as to the identity of adsorbed oxygen states on perovskites can be obtained from surface science studies of other materials; for example, from a combination of UV and X-ray PES and scanning tunnelling microscopy data for co-adsorption studies of ammonia oxidation, Carley *et al* proposed formation of a transient $O^{\delta-}$ state when oxygen adsorption is highly exothermic as is the case for Mg, Al, Ni, and Cu metals[23]. Formation of O^{2-} leads to inactivity and in the case of Mg, Mg^{2+}, formed by electron donation, is detected by XPS. In the case of weak oxygen adsorption, as for Ag and Zn, $O_2^{\delta-}$ has been identified[23]. **Figure 2.8** shows a cartoon model for the reaction dynamics of the dissociative chemisorption of oxygen at a Cu surface.

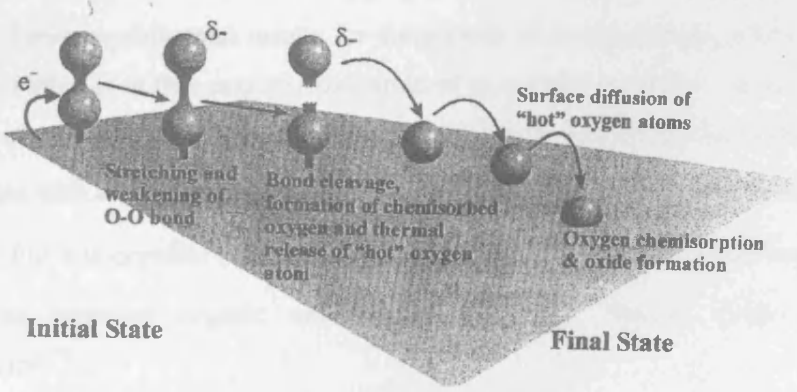

Figure 2.8 *Dissociative chemisorption of oxygen at a Cu (110) surface* [23]

A number of studies are reported where EPR has been applied to identify oxygen states on simple ionic oxides. For example, in an early review, Che *et al* have concluded that there is firm evidence for O^- and the superoxide ion O_2^- on several oxides and weak evidence for the peroxide ion O_2^{2-}. In addition Zhang *et al* [24] and Soria et al have detected O_2^- on CeO_2, Il'ichev *et al* detected O_2^- on ZrO_2[25] and Iwamoto *et al* have detected O^-, O_2^- and O_3^- on MgO and have proposed an order of activity $O^- > O_3^- > O_2^-$ [26]. Finally, in their recent review on oxidation reactions over

solid solution oxides, Stone *et al* discuss reaction mechanisms in terms of high and low coordinate O^{2-} ions[27].

Computational modelling has also been applied to simple oxides, for example Kantorovich *et al* using Density Functional Theory (DFT) slab configuration calculations which have predicted favourable formation of the peroxide ion O_2^{2-} by adsorption of atomic oxygen at a lattice oxygen site in MgO[28]. Molecular oxygen is only weakly adsorbed. Islam *et al* have carried out atomistic calculations to examine the formation of O^- and O_2^{2-} species on La_2O_3 and have considered the interaction of molecular oxygen with oxygen vacancies to form hole species ($2O^-$ or O_2^{2-})[29].

In the case of more covalent oxides, e.g. vanadium oxides, DFT cluster calculations have indicated that molecular oxygen is strongly adsorbed at oxygen vacancies[30]. The adsorbed molecule is then strongly polarised leading to activation and dissociation. From experimental results for these kinds of oxide systems, it has been postulated by Haber *et al* that catalytic oxidation of an organic molecule can proceed via either an electrophilic or nucleophilic mechanism[31]. For electrophilic oxidation, reaction occurs with activated oxygen, O_2, O_2^- or O^-, leading to total oxidation, i.e. combustion. For nucleophilic oxidation, lattice oxygen O^{2-} performs a nucleophilc attack on the activated organic molecule to give high chemo-, regio- and stereoselectivity[31].

Overall, experimental approaches to identifying oxygen states involved in catalysis over perovskites are difficult, particularly *in situ*, and conclusions remain ambiguous from other materials especially from techniques like EPR. Hence there is a developing strong interest in computational modelling for help to identify the stable species.

2.3.4 The Ion-Redox Mechanism

Oxidation reactions on an oxide catalyst can be described by a kinetic redox mechanism involving the reaction between the oxidizable reactant and the active

oxygen of the surface (surface reduction)[32]. The reduced site of the catalyst then becomes reoxidized by the gas phase oxygen (surface oxidation), which has been described mechanistically by Petrolekas *et al* according to the equations below:

Reaction between the oxidizable reactant (R) and active oxidised surface (OS) to give a product (RO) and a reduced surface site (S),

$$R(g) + OS \rightarrow RO(g) + S \tag{2.9}$$

Reoxidation of the catalyst site by gas phase oxidation,

$$\begin{aligned} O_2(g) + S &\rightarrow O_2S \\ O_2S + S &\rightarrow 2OS \end{aligned} \tag{2.10}$$

If the rate limiting step is the adsorption of oxygen, this process is equivalent to the Mars-van Krevelan model[32]. It represents a two step redox process at a single site separated in time as shown in **Figure 2.9a**. This process is formally identical to the suprafacial mechanism discussed in **Section 2.3.2** where the active oxygen species (O^*) could be adsorbed oxygen. However at high temperatures, when lattice oxygen ion mobility is increased, oxygen ions can be transported through the oxide lattice from the bulk to replenish the reduced surface. Oxygen in the bulk can be replenished by transport from another surface reoxidation site as shown in **Figure 2.9b**. Reduction and oxidation of the catalyst surface occur at different sites separated in space. Bulk lattice oxygen is the intermediate species and the rate limiting step is the diffusion of the lattice oxygen. It is formally identical to the intrafacial mechanism, discussed in **Section 2.3.2**, and has been referred to as the ion redox model. In the ion redox model, the overall catalytic redox cycle can be described by the following equation:

$$2B^{(n+1)+} + O_O^X \rightarrow 2B^{n+} + \tfrac{1}{2}O_2(g) + V_O^{\bullet\bullet} \tag{2.11}$$

The details of this mechanism generally depend on the identity of the transition metal B and the nature of the A site dopant

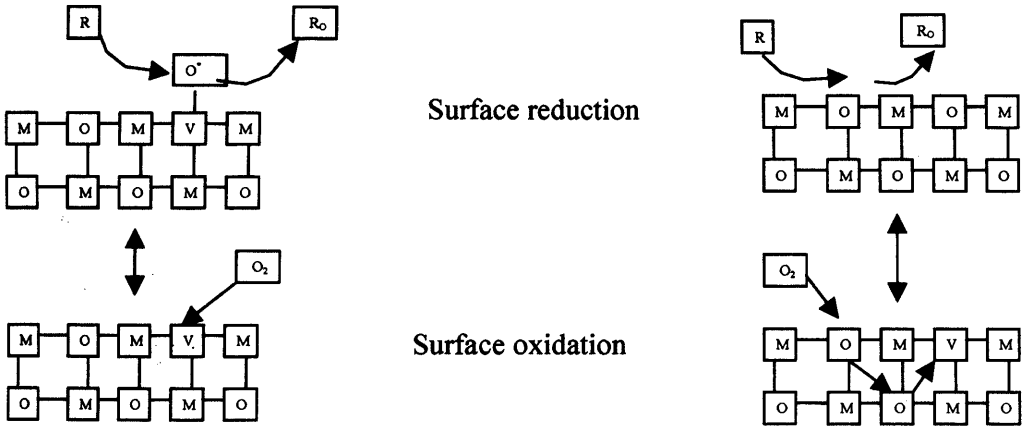

Figure 2.9 *Schematic Diagrams of (a) The Mars-Van Krevelan Model and (b) The Ion Redox Model* [32].

Of key importance in oxidation catalysis is the redox behaviour of the B site Co^{3+}/Co^{2+} in $LaCoO_3$, or Mn^{4+}/Mn^{3+} in the case of $LaMnO_3$, linked to the formation of oxygen vacancies[33]. In simple terms, during an oxidation process creation of vacancies at the surface can couple with reduction of the B site cation. It can be reversed by the adsorption of oxygen, which effectively reactivates the catalyst surface. For example, in $LaCoO_3$, the Co^{3+} is the active site in the oxidation process, in which Co^{3+} is reduced to Co^{2+} during the catalytic oxidation of the reactant, for example CH_4. The oxidation of methane occurs via removal of surface lattice oxygen, which is replenished by diffusion from the bulk. The catalyst is reduced and an oxygen ion lattice vacancy occurs. Subsequently, the bulk of the catalyst is replenished with oxygen from the gas phase and the catalyst is re-oxidized with Co^{2+} returning to Co^{3+}. The rate-determining step in this mechanism is the diffusion of oxygen in the bulk.

The schematic diagrams in **Figure 2.9a** and **b** represent an ideal surface view. In reality oxide catalysts are polycrystalline with a substantial amount of grain boundary contact as in **Figure 2.10**[19]. This model is idealised in **Figure 2.11** showing the different steps involved in oxygen adsorption, diffusion and exchange, i.e. surface adsorption and gas phase exchange (1), diffusion across the surface (2), diffusion

from the surface into the bulk (3) and grain boundaries (4) and diffusion between the grain boundaries and the bulk (3')[19].

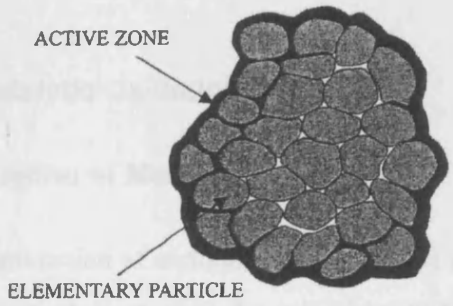

Figure 2.10 *A schematic view of the active zone for methane oxidation*[19]

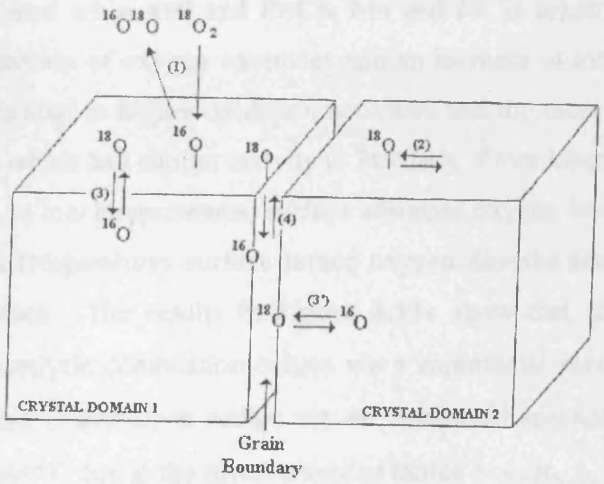

Figure 2.11 *Schematic diagram for the oxygen exchange mechanism in* $LaCoO_3$[19]

Oxygen isotopic exchange (OIE) has been shown to be an important experimental technique to study oxygen exchange at real oxide surfaces. For example, Nakamura *et al* have shown that Sr doped $LaCoO_3$ has enhanced OIE at 300°C compared to undoped $LaCoO_3$ due to creation of oxygen vacancies[20]. Kaliaguine *et al* have recently applied OIE at temperatures between 370 and 750°C to determine the relative importance of the oxygen transport steps depicted in **Figure 2.11** by comparing OIE

rates as a function of surface area, crystallite size and level of grain boundary contact for a series of $LaCoO_3$ materials[19,34]. The authors concluded that the amount of oxygen available for catalysis was restricted to a near surface active zone dominated by grain boundary effects as in **Figure 2.10.**

2.3.5 Some Catalytic Oxidation Applications

2.3.5.1 Combustion of Methane

The catalytic combustion of methane can occur over a number of different perovskite formulations. Arai *et al*, studied the catalytic combustion of methane over $LaMO_3$ (M= Cr, Mn, Fe, Co, Ni, Cu) and partially substituted $La_{(1-x)}A_xMO_3$ (M=Mn, Fe, Co; A= Sr,Ca,Ba,Ce; $0<x<0.4$) which were compared with Pt/Al_2O_3 catalysts[35]. Active catalysts are created when x=0 and B=Co, Mn and Fe Sr substitution at the A site leads to the formation of oxygen vacancies and an increase in ionic mobility. These compositions resulted in higher oxidation activities and the most active catalyst was $La_{0.6}Sr_{0.4}MnO_3$, which had similar activity to Pt/Al_2O_3. From kinetic measurements, it was shown that, at low temperatures, surface adsorbed oxygen was used for oxidation whereas at high temperatures surface lattice oxygen desorbs and oxygen vacancies occur in the lattice. The results in **Figure 2.12a** show that, at low temperatures (<500°C), the catalytic combustion occurs via a suprafacial mechanism whereas at high temperatures (>600°C) it occurs via an intrafacial mechanism. The rate of reaction above 600°C due to the involvement of lattice oxygen, r_l, is greatly enhanced compared to the rate below 500°C due to adsorbed oxygen, r_a[35].

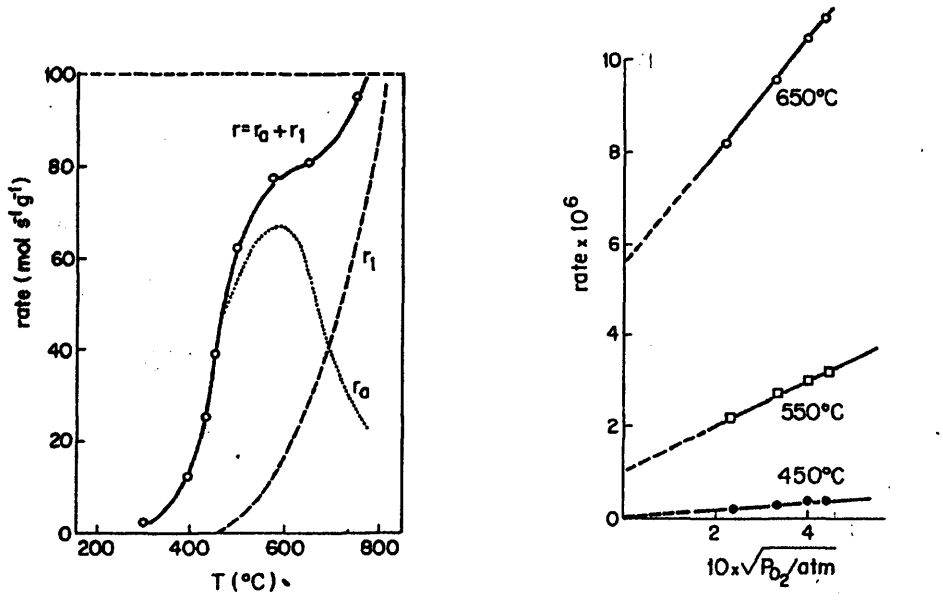

(a) (b)

Figure 2.12a *Rate of methane oxidation over $La_{0.6}Sr_{0.4}MnO_3$. Circles, experimental: dashed line, rate expected for oxidation by lattice oxygen:pointed line,rate expected for oxidation by adsorbed molecular oxygen* **b** *Rate for methane oxidation versus $P_{O_2}^{0.5}$:intercepts represent contributions of lattice oxygen*[34].

Arai *et al* also investigated the dependence on the partial pressure of methane and oxygen giving the following equation:

$$r = k.P_{CH_4}^{m}.P_{O_2}^{n} \quad , \qquad (2.12)$$

where r is the oxidation rate of methane and m and n are the reaction orders of methane and oxygen respectively for two substituted $La_{0.8}Sr_{0.2}MO_3$ materials(M= Co, Mn)[35]. The results show that the oxidation rate is first order with respect to CH_4, but n is fractional and decreases with increasing temperature, which indicates a variation in the oxygen species involved from the molecular adsorbed species to lattice oxygen as a function of temperature. The contributions of the adsorbed and lattice oxygen species can be shown in **Figure 2.12b** by plotting the experimental rate versus $P_{O_2}^{0.5}$. The intercepts of the straight lines show the contribution of the lattice oxygen, which is expected to increase as the temperature increases[35].

McCarty and Wise have also discussed a mechanism for the formation of oxygen vacancies by the reduction of the transition metal[36]. They suggested that anion vacancies are important in the combustion of hydrocarbons and also that the changes of the cation oxidation state in the perovskites are important in the adsorption of the hydrocarbons.

Kremenic *et al* investigated the catalytic combustion of propene and isobutene over $LaMO_3$ perovskites (M= Cr,Mn,Fe,Co, and Ni) at 300°C[37]. From **Figure 2.13** it can be seen that the catalytic activity is minimized for M= Cr,Fe,Ni and maximized for Mn and Co. The rate for isobutene was higher compared to propene. It is claimed that the catalytic activity could be influenced by the crystal field stabilization energies. The results can also be interpreted in terms of a more favourable redox behaviour of Co and Mn, particularly compared to Fe at 300°C, in relation to activation of O_2 as O_2^- on adsorption[37].

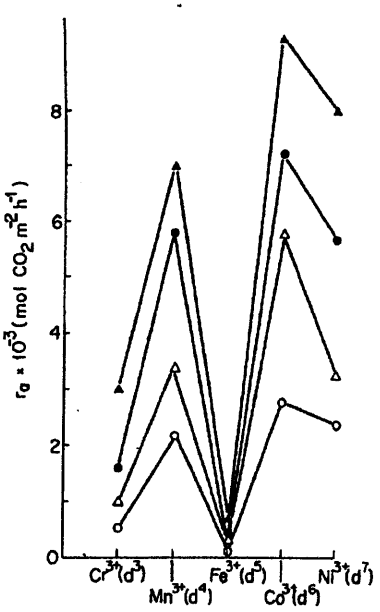

Figure 2.13 *Rates of propylene (open symbols) and isobutene (filled symbols) oxidations over $LaMO_3$ oxides at 300 °C. Molar ratio $HC:O_2$=25:1(circles) or 2:1(triangles)*[36].

While the effect of Sr^{2+} doping on catalytic methane combustion activity is relatively well understood experimentally and theoretically in terms of compensating oxygen

ion lattice vacancies[11], the interpretation of the effect of Ce^{4+} doping is complicated by the formation of mixed phase materials with segregation of CeO_2. Further complications arise when comparing results in the literature due to different preparation methods, different reaction temperature regimes and different ways of reporting catalytic activity, for example, measuring conversion levels at fixed temperatures or temperatures for specified levels of conversion (frequently 50%) from light off curves, without calculating *specific reaction rates.* For example, doping with low levels of Ce (x ~ 0.05 in $La_{1-x}Ce_xCoO_3$) appears to lead to a small drop in catalytic activity for CH_4 combustion under conditions of low conversion (<20%) in the low temperature regime (360°C) until at higher Ce levels (x~0.1-0.2), when CeO_2 is readily detected by XRD, the activity returns[38]. However, work at higher temperature (600°C) and higher levels of conversion (>50%) shows that, if reaction rates are calculated and normalised to surface area, the derived *specific catalytic activity* is significantly increased for Ce dopant levels of only 5% and there is no further increase for higher formulation levels of Ce[39]. Furthermore, this work has also shown that the phase segregated CeO_2 would have relatively low activity compared to $LaCoO_3$. Enhancement in activity at high temperature is therefore dominated by the Ce^{4+} dopant acting within the $LaCoO_3$ surface lattice.

2.3.5.2 CO Oxidation

Voorhoeve *et al* have suggested that CO oxidation occurs via a suprafacial mechanism at 300°C[14]. For $LnBO_3$ perovskites (Ln=lanthanides) it was shown that the Ln^{3+} ions are inactive and the M^{3+} transition metal is the active species in catalysis. For $LaBO_3$, where B is a transition metal from V to Ni, the work demonstrated that $LaCoO_3$ is the most active and $LaCrO_3$ is the least active.

From spectroscopic data, Tascon *et al* proposed a mechanism for the oxidation of CO on $LaCoO_3$ where initially oxygen is adsorbed as molecular (O_2^-) species on the cobalt ion which then dissociates giving atomic (O^-) oxygen adsorbed on the same site[40]. The CO adsorbs on the surface oxide ions, which then interacts with the adsorbed atomic oxygen producing a carbonate structure, which then decomposes to give CO_2 and O_2.

$$
\begin{aligned}
&O_{2(g)} \rightarrow O^-_{2(ads)} \rightarrow 2O^{2-}_{(ads)} \\
&CO_{(g)} \rightarrow CO_{(ads)} \\
&CO_{(ads)} + 2^-_{2(ads)} \rightarrow 2O^{2-}_{(ads)} \\
&CO_{3(ads)} \rightarrow CO_{2(ads)} + O^{2-}_{(ads)} \rightarrow CO_{2(g)} + O^{2-}_{(ads)}
\end{aligned}
\qquad (2.13)
$$

Rao and Chakrabarty investigated the effect on carbon monoxide oxidation of different perovskite cobaltites $Ln_{1-x}M_xCoO_3$ (Ln= La, Sm and M= Pb, Ba, Th)[41]. Experimentally it appeared that substitution of Ln both by divalent and tetravalent ions increases the catalytic activity and shows no correlation with the valency of cobalt. However, a modern interpretation of dopant solubility as a function of atom size would suggest that none of the dopants (M) would be highly soluble[41].

Voorhoeve *et al* investigated the catalytic activity of non-stoichiometric materials and showed that the substitution at the A site with Ce^{4+}, accompanied by the supposed reduction of Co^{3+} to Co^{2+}, enhances the catalytic oxidation of CO[42]. However the substitution of Sr^{2+} at the A site with the supposed oxidation of Co^{3+} to Co^{4+} shows a reduction in catalytic oxidation. This interpretation of defect structure as a function of divalent and tetravalent A site doping is not in accord with a more modern view from computational modelling discussed in **Section 2.1.3.2.** The CO is bonded to the transition metal as a carbonyl and the lone pair from the carbon atom goes into the empty d_z^2 orbital of the metal to form the σ bond. There is also the back donation of the t_{2g} electrons from the transition metal to the antibonding π-orbital of CO. This can be seen below in **Figure 2.14**[42].

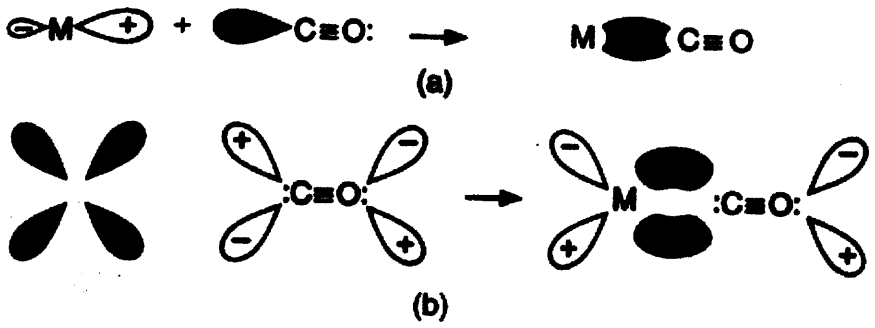

Figure 2.14 (a) the formation of the Metal← Carbon σ bond using unshared pair of the C atom. **(b)** The formation of the Metal → Carbon π bond. The outer orbitals on the CO are omitted for clarity [42].

More recently Petrolekas *et al* have studied CO oxidation over $La_{0.5}$ $Sr_{0.5}MnO_3$ using solid electrolyte potentiometry (SEP)[32]. They observed a sharp change in kinetic behaviour between 500°C and 550°C. This corresponds to a switch from a suprafacial process at low temperature to a high temperature intrafacial ion redox process when the lattice oxygen becomes mobile as discussed in **Section 2.3.4**. To interpret the results quantitatively the authors have employed the model in **Section 2.3.4**, distinguishing between a suprafacial Mars-van Krevelan type process, where adsorption of oxygen is the rate limiting step, from an intrafacial ion redox model, where diffusion of lattice oxygen is the rate limiting step.

It should be noted that oxidation of CO by NO in catalytic car exhaust depollution over perovksites, for example Sr doped $La_{1-x}Sr_xCoO_3$, is believed to proceed by removal of O^{2-} from the surface lattice followed by replenishment by NO adsorption and decomposition in oxygen vacancies.

2.3.5.3 Ammonia Oxidation

The use of transition metal oxide catalysts as replacements for precious metal (Pt/Rh) gauzes for high temperature ammonia oxidation to nitric oxide, a precursor for nitric acid manufacture, has been extensively reviewed by Sadykov *et al*[43].

Perovskites have been shown to be particularly important in terms of selectivity to nitric oxide (NO) formation and high temperatures (800-900°C) stability in resisting long term transition metal cation reduction due to the stability of the BO_6 octahedra. The selectivity to NO formation, as opposed to N_2 or N_2O, is particularly important. It has been proposed that this selectivity results from dilution of active sites at the surface by La^{3+} and the ability to oxidise through to NO faster than dimerisation of N containing intermediates, i.e. high oxygen surface coverage and activity is required.

A series of perovksites ($LaMO_3$) where (M = Ni, Co, Fe and Mn) have all been shown to be active for NH_3 oxidation at 800-900°C[17,44]. The selectivity to NO formation is significantly higher for $LaNiO_3$ and $LaCoO_3$ compared to $LaMnO_3$ and $LaFeO_3$. It has been shown that doping at the La site with a divalent ion such as Sr^{2+} enhances the activity of $LaMnO_3$ and $LaFeO_3$ somewhat while degrading the performance of $LaNiO_3$ and $LaCoO_3$ after an initial small enhancement at low Sr levels. Alternatively, when doping with tetravalent cations at the La site, it was revealed that Ce^{4+} shows a small enhancement to almost 100% NO selectivity for $LaCoO_3$. A similar enhancement was observed for Th^{4+} doping in $LaNiO_3$ at low dopant levels followed by degradation in performance.

It has been proposed that ammonia oxidation occurs via an intrafacial mechanism whereby lattice oxygen is extracted at high temperature by the following mechanism:

$$O_O^x + Co^{3+} \rightarrow O^- + Co^{2+} \qquad (2.14)$$

The O^- is considered to be the active species for NH_3 oxidation. The Co provides the adsorption site in $LaCoO_3$ for the activation of NH_3 for oxidation. The following equations show the stepwise mechanism occurring for NH_3 oxidation:

$$\begin{aligned} Co^{3+} + NH_3 + O^- &\rightarrow NH + Co^{2+} + H_2O \\ Co^{3+} + NH + O^- &\rightarrow NHO + Co^{2+} \\ Co^{3+} + 2NHO + O^- &\rightarrow 2NO + H_2O + Co^{2+} \end{aligned} \qquad (2.15)$$

The Co^{2+} is then reoxidised by transfer of oxygen from the lattice, which is then replenished from the gas phase as in the ion redox model shown in **Figure 2.9b**. Thus, a high activity oxygen surface is maintained.

When there is not enough oxygen available to form NO then it is possible for dimerization of the intermediates to occur forming N_2, which is given by the following

$$NHO + NH \rightarrow N_2 + H_2O \qquad (2.16)$$

The different behaviour of the various undoped and Sr doped perovskites has been discussed in terms of the redox behaviour of the transition metal B site and the different defect chemistries induced by Sr doping in relation to equation (2.11) for the ion redox model[17,44]. However the interpretation given by these authors predates a modern view of defect structure in La perovskites and the effects of dopants and is based on some uncertain EPR data detecting the presence of B^{4+} species.

The behaviour of Ce^{4+} in increasing selectivity to NO formation for $LaCoO_3$ has been attributed to enhanced redox behaviour of the material as shown in **Figure 2.15**[10]. However, the issue of low Ce solubility in $LaCoO_3$ and the appearance of a segregated CeO_2 phase as detected by XRD has not been discussed.

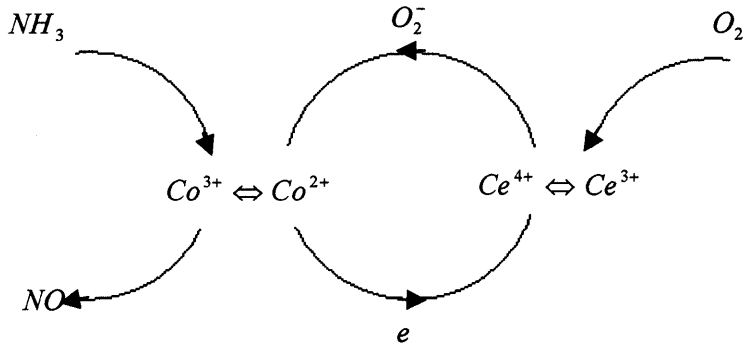

Figure 2.15 *Ammonia oxidation by $LaCoO_3$ involving Ce dopant*[10]

2.4 Challenges for Computational Modelling

In the preceding discussion $LaCoO_3$ perovskite has been identified as an important material in relation to a number of heterogeneous, catalytic oxidation processes. Also the presence of oxygen vacancies in $LaCoO_3$ has been shown experimentally to play a key role in oxygen adsorption and oxygen isotopic exchange and is believed to influence strongly catalytic oxidation performance as discussed in **Section 2.3.2** to **2.3.5.** It has been postulated that O_2^- and O^- active oxygen species are involved in these catalytic oxidation processes over $LaCoO_3$, involving suprafacial and intrafacial mechanisms respectively as a function of temperature. What has not been demonstrated experimentally is the precise nature of the active oxygen species and how the presence of oxygen vacancies modifies the perovskite surface behaviour in terms of oxygen adsorption and activation. Resolution of these issues represents a major challenge for computational modelling.

The role of divalent dopants such as Sr^{2+}in modifying defect structure in $LaCoO_3$ is fairly well understood experimentally and theoretically in terms of creating oxygen vacancies as discussed in **Section 2.2.3.1**. However, previous computational modelling work has largely focussed on the bulk material. In addition, there has been no computational study of the surface of undoped, reductively non-stoichiometric $LaCoO_3$ as normally prepared, which also contains oxygen vacancies as discussed in **Section 2.2.2**. A second challenge for computational work is therefore to model the surface structures of undoped, reductively non-stoichiometric and Sr^{2+} doped $LaCoO_3$ in terms of the disposition of oxygen vacancies, segregation of dopants and surface morphology.

It has also been shown experimentally that doping $LaCoO_3$ with tetravalent Ce^{4+} gives a measurable enhancement in catalytic oxidation performance for both methane combustion and ammonia oxidation as discussed in **Section 2.3.5.** This effect is not understood experimentally since segregation of a separate CeO_2 phase as detected by XRD, indicates low solubility. Low solubility has been confirmed by computational modelling for bulk $LaCoO_3$ as discussed in **Section 2.2.3.2.** A third challenge for

computational work is to model the behaviour of Ce at the surface of $LaCoO_3$ in terms of solubility and the nature of the favoured compensating defect process.

The solubility and precise effect of cation dopants in perovskites has been successfully modelled for a number of systems by atomistic computational methods, which can predict the favoured defect compensation processes in the bulk. However, for catalysis it is the structure and chemistry of the surface, which is important, and for $LaCoO_3$ perovskite, our knowledge of the surface structure and the processes during oxidation catalysis is limited. Therefore the main aim in this thesis is to develop a more complete understanding of the surface structure of $LaCoO_3$, and in particular the effect of doping Sr^{2+} and Ce^{4+} cations, in terms of enhancing catalytic performance through creation of oxygen vacancies or modifying cation redox behaviour. In addition quantum mechanical calculations have been carried out as a starting point for identifying the nature of the active oxygen species

REFERENCES

(1) J.L.G.Fierro; M.A.Pena. *Chem. Rev.* **2001**, *2001*, 1981.
(2) http://www.chemistry.ohio-state.edu, P. s. f.
(3) V.M.Goldschmidt; Skr.Nor.Videnk-Akad. *K1.I:Mat.-Naturvidensk.K.I* **1926**, *8*.
(4) H.Iwahara. *Solid State Ionics* **1995**, *77*, 289.
(5) C.H.Perry; D.J.McCarthy. *Physical Review* **1965**, *138*, A1537.
(6) H.J.M.Bouwmeester; P.J.Gellings. *Catalysis Today* **1992**, *12*, 1.
(7) G.V.Lewis; C.R.A.Catlow. *Radiation Effects* **1983**, *73*, 307.
(8) B.C.Tofield; W.R.Scott. *J Solid State Chemistry* **1974**, *10*, 183.
(9) K Kamata; T.Hayashi; T.Nakamura. *Mater.Res.Bul.* **1978**, *13*, 49.
(10) S.Fan; Q.Wang; B.Dou; Z.Yu. *Cuihua Xuebao* **1991**, *12*, 199.
(11) M.S.D.Read; M.Saiful; G.Watson; F.King; F.E.Hancock. *J. Mater. Chem.* **2000**, *10*, 2298.
(12) S.A.French; C.R.A.Catlow; R.J.Oldman; S.C.Rogers; S.A.Axon. *Chem.Commun,* **2002**, 2706.
(13) R.I.Masel *"Chemical Kinetics and Catalysis"*; Wiley-Interscience: New York, 2001.
(14) R.J.H.Voorhoeve; J.P.Remieka; L.G.Trimble. *N. Y. Ann, Acad.Sci.,* **1976**, *272*, 3.
(15) A.Beilanski; J.Haber. *Catal Reviews-Science and Engineering* **1979**, *19(1)*, 1.
(16) R.J.Oldman. *Synetix Report No 10* **2002**.
(17) Y.Wu; B.Dou; C.Wang; X.Xie; Z.Yu; S.Fa; Z.Fan; L.Wang. *J.Catal* **1989**, *88*, 120.
(18) Tascon, J. M. D.; J.L.G.Fierro; L.G.Tejuca *"Properties and Applications of Perovskite Oxides", Chapter 8, Infrared Spectroscopy and Temperature Programme Desorption*; Marcel Dekker, 1992.
(19) S.Royer; D.Duprez; S.Kaliaguine. *Journal of Catalysis* **2005**, *234*, 364.
(20) T.Nakamura; M.Misono; Y.Yoneda. *Bull. Chem.Soc.Jpn.* **1982**, *55*, 394.
(21) I.Rossetti; L.Forni. *Appl Catal B:Environ* **2001**, *33*, 345.
(22) M.O'Connel; A.K.Norman; C.F.Hutterman; M.A.Morris. *Catal.Today* **1999**, *47*, 123.
(23) A.F.Carley; P.R.Davies; M.W.Roberts. *Catal. Lett.* **2002**, *8(1-2)*, 25.
(24) X.Zhang; K.J.Klabunde. *Inorg.Chem.* **1992**, *31*, 1706.
(25) A.N.Il'ichev; M.D.Shibonova; V.N.Korchak. *Kinetic and Catalysis* **2004**, *45(1)*, 114.
(26) M.Iwamoto; J.H.Lunsford. *J.Phys.Chem.* **1980**, *84*, 3079.
(27) F.S.Stone; A.Cimino. *Advances in Catalysis* **2002**, *47*, 141.
(28) L.N.Kantorovich; M.J.Gillan. *Surface Science* **1997**, *374(1-3)*, 373.
(29) M.S.Islam; D.J.Ilett; S.C.Parker. *J.Phys.Chem.* **1994**, *98*, 9637.
(30) I.Czekaj; K.Hermann; M.Witko. *Surface Science* **2003**, *545(1-2)*, 85.
(31) J.Haber; M.Witko. *Catal. Lett.* **1991**, *9(3-4)*, 297.
(32) P.D.Petrolekas; I.S.Metcalfe. *Journal of Catalysis* **1995**, *152*, 147.
(33) N.N.Kovaleva; I.L.Gavartin; A.L.Shluger; A.V.Boris; A.M.Stoneham. *Physica.B* **2002**, *313*, 734.
(34) S.Royer; D.Duprez; S.Kaliaguine. *Catal.Today* **2006**, *112(1-4)*, 99.

(35) H.Aria; T.Yamada; K.Guahi; T.Seiyama. *Appl Catal.* **1986**, *26*, 265.
(36) J.G.McCarty; H.Wise. *Catalysis today* **1990**, *89*, 231.
(37) G.Kremenic; J.M.L.Nieto; J.M.D.Tascon; L.G.Tejuce. *J.Chem Soc, Faraday trans 1* **1985**, *81*, 939.
(38) C.Oliva; L.Forni; A.D.Ambrosio; F.Novarrini; A.D.Stepanov; Z.D.Kagramanov; A.I.Mikhailichenko. *Appl.Catal A:Gen.* **2001**, *201*, 245.
(39) J.Kirchinerova; M.Alifanto; B.Delmon. *Appl. Cat A: Gen.* **2002**, *231*, 65.
(40) J.M.D.Tascon; J.L.GFierro; L.G.Tejuca. *ZPhys.Chem.(Wiesbaden)* **1981**, *124*, 249.
(41) D.Y.Rao; D.K.Chakrabarty. *Ind.J.Chem.* **1984**, *23A*, 375.
(42) R.J.H.Voorhoeve *"Advanced Materials in Catalysis"*; Academic press: New York, 1977.
(43) V.A.Sadykov; L.A.Isupova; I.A.Zolotarskii; L.N.Bobrova; A.S.Noskov; V.N.Parmon; E.A.Brushtein; T.V.Telyatnikova; V.I.Chernyshev; V.V.Lunin. *Appl Catal A:General,* **2000**, *204*, 59.
(44) Z.Yu; L.Gao; S.Yuoh; Y.Wu. *J.Chem Soc, Faraday Trans. 1* **1992**, *88*, 3245.

CHAPTER 3

3. COMPUTATIONAL METHODOLOGY

Computational modelling techniques are being used extensively to develop molecular models and to determine structures, energetics and dynamics of complex materials. These techniques can be combined with results from experiments in constructing models and solving structural and other chemical problems.

There are many different methods used in computational chemistry, including atomistic methods (i.e. methods based on interatomic potentials), quantum mechanics (QM) and increasing methods that attempt to model at larger lengths and time scales[1]. In this thesis, we use a range of atomistic methods and quantum mechanical techniques both of which rest ultimately on the Born Oppenheimer approximation. Both methods involve the evaluation of an expression for the energy for a given geometry. An equilibrium structure is then obtained by varying the atomic positions to minimize the energy expression.

In this chapter, we concentrate on the atomistic approach but then consider the main concepts for quantum mechanical methods. Atomistic methods have been used for all the initial bulk defect and surface calculations. But, to determine a more accurate representation for the electronic structure of $LaCoO_3$ quantum mechanical methods have also been employed for the bulk and defect simulations.

3.1 Atomistic Methods

We define atomistic methods as those based on the use of interatomic potentials to describe the forces between atoms in a system. These methods allow calculations to be done on structures containing thousands of atoms to identify the ground state structure and determine the thermodynamic and kinetic properties. The great computational speed of atomistic methods allows for their use in procedures such as

molecular dynamics (MD), Monte-Carlo Simulations (MC) conformational energy searching, and docking, which require large numbers of energy evaluations[1].

Atomistic methods model each atom (or sometimes group of atoms) as a single particle. These atom-like particles are usually spherical and have a net charge. The interactions which occur between these particles are described by numerical or more common analytical functions which are discussed below[1]. The classical potentials which have been considered in this thesis are those which can be used for ionic solids such as the perovskite material $LaCoO_3$. The predominant interaction which occurs in such solids is the Coulombic interaction, which will be discussed in more detail below. For covalent materials, specific short-range, bonding terms (e.g. bond-harmonic or Morse potentials) must be included[2]. The simpler bonding, characteristic of ionic solids, allows them to be modelled by potentials which compute Coulomb interactions and non-bonded short range terms.

3.1.1 Potentials for Ionic System

As noted above interactions in these solids have two components: the dominant long range electrostatic Coulombic interaction and the short range term including overlap repulsion and the weaker van der Waals attraction[3].

The electrostatic contribution (E_{el}) in the non-bonded energy is modelled using a Coulombic potential. This electrostatic energy is a function of the charges on the non-bonded atoms and their interatomic distance, and is written as:

$$E_{el}(R^{AB}) = \frac{Q^A Q^B}{R^{AB}} \quad , \tag{3.1}$$

where R is the separation between the atoms A and B, Q^A and Q^B are the charges on the corresponding atoms. If part of the system, e.g. the solvent, is not modelled by an explicit atomistic approach, a dielectric constant ε may then be included in the denominator. Such methods are not used in this thesis.

The non-bonded term comprises both an attractive and a repulsive term. The van der Waals attraction can be described as the mutual attraction between two atoms due to

an induced-dipole induced-dipole interaction[3]. The induced dipole can be created as followed: an uncharged isolated atom will not have a dipole on average but, because the electrons are moving around the nucleus, it is possible to realise a spontaneous dipole, which will then induce a dipole in the nearby atom and will cause an attraction. It is also called the "London force" or dispersive interaction[3]. The van der Waals repulsive term arises at close interatomic separations where there is repulsion arising from "Pauli" or overlap repulsion.

The non-bonded energy is very positive (repulsive) at short distances, has a minimum which is negative at a distance corresponding to the two atoms which are at interatomic distance and goes towards zero as the distance increases which is shown in **Figure 3.1**. A general functional form for the non-bonded interaction is given by:

$$E_{NB}(R^{AB}) = E_{repulsive}(R^{AB}) - \frac{C^{AB}}{(R^{AB})^6} \quad , \tag{3.2}$$

where C is a constant for a specific material and R is the distance between the atoms A and B.

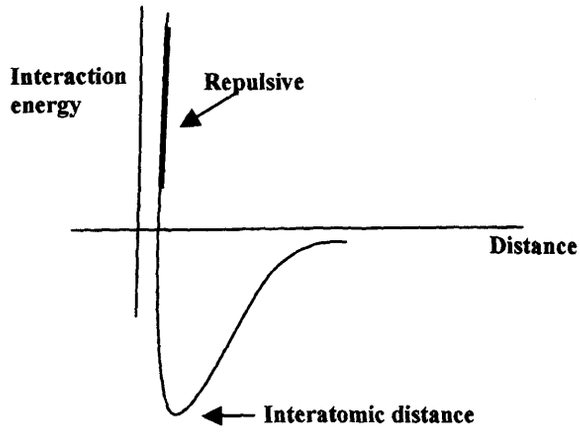

Figure 3.1 *The repulsive energy for the Van der Waals interaction.*

There is no precise analytical expression for the repulsive energy. A common form is the Lennard- Jones potential (E_{LJ})[4], where the repulsive part is dependent on R^{-12}:

$$R_{LJ}(R) = \frac{C_1}{R^{12}} - \frac{C_2}{R^6} \quad , \tag{3.3}$$

and C_1 and C_2 are constants. These parameters control the depth and position (interatomic distance) of the potential energy well for a given pair of non-bonded interacting atoms. In simple terms, C_2 determines the degree of "stickiness" of the van der Waals attraction and C_1 determines the degree of "hardness" of the atoms. There is some evidence that other repulsive exponents can be used instead of R^{-12}, for example R^{-9} or R^{-10}, which can give better results in some systems[4].

An alternative is the Buckingham potential (E_{Buck}) which models repulsive effects of the overlap of the electron wavefunctions assuming the electron density falls exponentionally with distance from the nucleus[5]. It can be written as:

$$E_{Buck}(R) = Ae^{-R/\rho} - \frac{C}{R^6} \qquad (3.4)$$

where A, ρ and C are constants and R is the interatomic distance. This is most common in ionic systems[5]. The first term in the equation is the hard core repulsion while the second term describes the short range attraction. This latter potential gives rise to a problem at short interatomic distances where it 'turns over' i.e. that as R goes toward zero, the exponential becomes a constant (A) while the R^{-6} term goes towards minus infinity. In practice this feature is rarely a problem as this unphysical region only occurs at much shorter interaction distance than are accessed in a real system[5].

The attractive parts of both potentials are the same with the main difference between the Lennard Jones and Buckingham functions being the repulsive part at short distances where the Lennard Jones potential sometimes tends to overestimate the repulsion. The Buckingham potential is also more flexible as it has three parameters (A, ρ and R) whereas the Lennard Jones potential has only two. It has therefore been much more widely used in an ionic system and is employed in all the parameterizations used in this thesis[4,5].

Calculating the non-bonded energy can be very time consuming due to the considerable range of the interactions. Significant time can be saved if the van der Waals potential is truncated at some distance, which is called the cut-off radius: at distances larger than the cut-off radius the contribution is set to zero. Since the van der Waals interaction potential is relatively short range and dies out as $1/R^6$, beyond 8-10Å the energy and forces can be safely set to zero. Thus using a cut-off at about

10Å is usually a reasonable approximation. However the Coulombic interactions die off as $1/R$ so even at considerable distances the energy of interaction is not negligible and it is never safe to time the Coulombic summation which must be summed to infinity[6]. The most widely used procedure to handle this term is the Ewald summation which can sum the Coulombic interactions to infinity in a periodic system. This approach transforms the Coulombic summation into two convergent sums, one of which can be carried out in reciprocal space while the other can be carried out in real space[6]. This is employed in all simulation program used in this thesis.

3.1.2 Polarisablity

Polarisability relates to the tendency of the electron cloud of an atom to be distorted from its normal shape by the presence of an ion, dipole or electric field. There are two methods of modelling polarisability: the first is to use a point ion, dipolar polarisability, (α), so that in the presence of an electric field (E) the dipole moment (μ) is given by [7]:

$$\mu = \alpha E \tag{3.5}$$

This model has been used for both molecular and ionic materials. However this model includes no coupling between polarisation and the surrounding environment, which can lead to excess polarisation.

The second method of modelling ionic polarisability is the shell model of Dick and Overhauser[8], which treats each ion as a core and shell, where the core represents the nucleus and the core electrons, and the shell models the valence electrons and is coupled to the core with a harmonic spring with a spring constant k as illustrated in **Figure 3.2**. The ion charge is divided between the core and shell such that the sum of the charges is the total ion charge. The free ion polarisability (α) is related to the shell charge (Y) and the spring constant (k)[8].

$$\alpha = \frac{Y^2}{k} \tag{3.6}$$

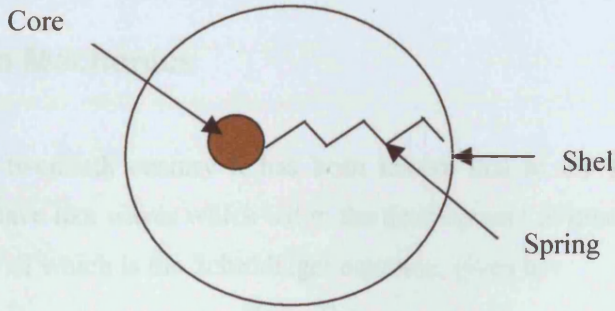

Figure 3.2 *Model of a polarisable ion showing the core connecting to the shell by a spring. (Note that in the implentation of the model both core and shell are point entities.)*[8]

The shell model allows polarisation to be coupled to be environment and is the preferred way of describing polarisation in systems such as materials modelled in this thesis, which contain strong fields. Shell model potentials are used throughout this thesis.

3.1.3 Parameterisation of Potentials

When employing the atomistic method it is necessary to determine the parameters for the potentials, which calculate the energy and the properties of the system. There are generally two methods by which we can parameterize the potentials. One method is to obtain the potential parameters by fitting to experimental data[9,10]. This method requires knowledge of the various observable quantities e.g. crystal structure, elastic, dielectric properties, vibrational spectra, calorimetric data which is then fitted using the least square procedure. The second method is to calculate the potential energy surface using a theoretical method. The theoretical method can be either be done by the electron gas or ab initio method. The electron gas method describes an atom by an electron gas, which is then used to calculate the interaction energies between the atoms. The ab initio method is more expensive computationally but offers greater accuracy. Detailed discussions are given in references[11-14].

The potential parameters used in this thesis have been taken from previous literature and are discussed in **Section 3.6** and tabulated in **Table 3.1**[9].

3.2 Quantum Mechanics

Since the early twentieth century it has been known that at the sub atomic level particles can behave like waves which led to the development of quantum mechanics, a basic postulate of which is the Schrödinger equation, given by:

$$H\psi = E\psi \ , \qquad (3.7)$$

where H is the Hamiltonian operator for the system, ψ is the wavefunction and E is the energy of the system. The wavefunction itself is not an observable property but $\psi\psi^*$ gives the corresponding particle density.

The Hamiltonian operator in the Schrödinger equation contains the kinetic and potential energy of the system. Therefore substituting the kinetic and potential energy into the Hamiltonian operator gives the Schrödinger equation for one electron atom

$$[1/2\nabla^2 - Z/r]\psi = E\psi \qquad (3.8)$$

where the electron kinetic energy is represented by $1/2\,\nabla^2$ (where ∇^2 is the shorthand for $d^2/dx^2+d^2/dy^2+d^2/dz^2$) and the potential energy (Z/r) is the attraction between the electron and neutron. This equation can be solved exactly for the one electron system. The Schrödinger equation cannot be solved exactly for the many electron system. Therefore approximations need to be made for the many electron system to determine the real solution of the Schrödinger equation, which are discussed in the following sections.

3.2.1 Hartree Fock Theory

The Hartree Fock theory includes electron-electron repulsion by a meanfield approximation. Electrons will move in a potential like independent electrons but they would feel an average repulsion between them. This potential contains electrostatic repulsion arising from r_{12}^{-1} operator[15].

When considering the electronic wavefunction for a molecule with many electrons, two additional features need to be considered for each electron. The first is that each electron has its own spin, which has to be included into the wavefunction. The individual spins can be referred to as up and down, or α and β. Electrons are also indistinguishable, and when electrons interchange, their wavefunction must change sign i.e. they show exchange symmetry, which is the basis of the Pauli Exclusion Principle. Therefore when considering many electrons the product of the wave function is replaced by an antisymmetrized determinantal wave function, which is called a Slater determinant. The consequence of the exchange symmetry can be expressed by the antisymmetrized wavefunction and it includes a second electron-electron term namely the exchange energy (K)[15].

Substituting all the energy terms described above in the Hamiltonian of the Schrödinger equation gives the Hartee Fock equation for each electron. The quality of this wavefunction created in equation (3.9) can be tested by using the variational principle which states that the better the wavefunction the lower will be the energy of the system.

$$\left[H^N + \sum_i J - \sum_i K\right]\phi_i = E\phi_i \qquad (3.9)$$

where the summations are over all the occupied orbitals[15].

From the Hamiltonian the various eigenfunctions, ϕ_i the eigenvalue E_i are generated[16]. The molecular orbitals functions ϕ_i can be calculated by the linear combination of the one electron atomic orbitals (LCAO). Therefore the molecular orbital can be expanded in terms of atomic basis functions, representing the atomic orbitals, according to the equation:

$$\phi_i = \sum_k c_{ik}\theta_k \quad , \qquad (3.10)$$

where ϕ_i is the molecular orbital, θ_k is the atomic basis function and c_{ik} is a coefficient which needs to be calculated to get the optimized molecular orbital. The coefficient denotes the contribution of the one electron wavefunction θ_k to the molecular orbital ϕ_i. The process is repeated until the coefficients are similar to the previous cycle. The results are then said to be self-consistent, and have the name self-

consistent field (SCF) theory. The types of basis function, which can be used, will be discussed in detail in **Section 3.2.3**.

3.2.2 Density Functional Theory (DFT)

The Hartree Fock theory is based on a many electron wavefunction, which needs to be calculated. Density Functional Theory (DFT) has been applied to replace the many body electronic wavefunction with the electron density as the basic quantity. While the many electron wavefunction depends on 3N variables for closed systems (three spatial variables for each of the N electrons), the density functional theory depends only on density as the function, which is easier to calculate.

There have been many variations of the density functional theory. The basis was the demonstration by Hohenberg and Kohn that all the ground properties are functionals of the charge density *(ρ)*[17]. Thus there is a one to one correspondence between the electron density and the energy. The total electronic energy of the interacting system is given below:

$$E[\rho] = E_{ke}[\rho] + E_{ne}[\rho] + E_{ee}[\rho] \ , \qquad (3.11)$$

where E_{ke} is the kinetic energy of the interacting system with electron density ρ, E_{ne} is the potential energy due to the Coulombic interactions and E_{ee} is the electron repulsion. This theory does not give any information about the energy (functionals) of the system.

Using the above theory, the kinetic energy (E_{ke}) is not represented well for a real system with interacting electrons[17]. Therefore a different model has been considered which replaces the interacting kinetic energy with that of a non-interacting electron system. The density and the energy of this system must be equal to the real system. In order to make this system have the same energy and density, the electrons are made to move in a modified external potential to that of the real system. Therefore the electrons are considered to be non-interacting and moving in an effective potential[17].

The E_{ee} term is separated into two energies, one of which is the classical Coloumb interaction (J) of the electrons and the other is the exchange correlation term E_{xc}. Therefore the total energy of the non-interacting system as a function of ρ can be given as:

$$E[\rho] = E_{non-ke}[\rho] + E_{ne}[\rho] + \{J[\rho] + E_{xc}[\rho]\} \qquad (3.12)$$

The E_{xc} term is the sum of the error in the kinetic energy when using the non interacting system and the error of treating the electron-electron interaction classically[17]. It is given by:

$$E_{xc}[\rho] = E_{ke}[\rho] - E_{non-ke}[\rho] + J[\rho] - E_{ee}[\rho] \qquad (3.13)$$

where E_{ke} is the kinetic energy and E_{ee} is the electron–electron interaction in the real system.

Similar to the Hartree Fock method, Kohn and Sham showed that the non-interacting electron wavefunction maybe written in terms of molecular orbitals[17]. These orbitals are called the Kohn Sham orbitals (φ_i) and the electron density for each Kohn Sham orbital would be:

$$\rho(r) = \sum [\phi_i(r)]^2 \qquad (3.14)$$

where the sum is over all the occupied Kohn Sham orbitals.

As for the Hartree Fock method, the Schrödinger equation can be solved by putting the energy contributions into the Hamiltonian operator[17]. The Hartee Fock theory does not consider the correlation between the electrons and all electrons are known to be moving in a static potential (repulsive). However, the improved density functional theory considers the correlations between the electrons[17]. Therefore the Kohn Sham atomic orbital (θ) at given point (r) gives the following Schrödinger equation for each electron:

$$[-1/2\nabla^2 - V_{eff}(r)]\phi(r) = E\phi(r) \qquad (3.15)$$

The effective potential is due to the non-interacting electrons represented in the density functional theory and is given below:

$$V_{eff}(r) = V(r) + \int \frac{\rho(r)}{|r - r'|} dr + V_{XC}(r) \tag{3.16}$$

where the first term is the electron and nucleus potential, the second is the electron-electron Coloumb potential and the final term is the exchange correlation potential which is given by :

$$V_{XC}(r) = \frac{\partial E_{XC}[\rho(r)]}{\partial \rho(r)} \tag{3.17}$$

The above equations from (3.14) and (3.16) are called the Kohn Shan equations, and they can be solved by an iterative process, which can be done by assuming an initial density from equation (3.14). From this initial density, the effective potential V_{eff} can be calculated and equation (3.15) can be solved obtaining a new electron density. Furthermore, from this new electron density an updated effective potential is calculated and the process is repeated until the new electron density is equal to the previous one. Therefore once the exchange correlation functional is known the energy of the system can then be calculated.

To calculate the exchange-correlation energy, approximations are necessary. The simplest is the local density approximation (LDA)[18]. The LDA is based on the known exchange-correlation energy for a uniform gas with interacting electrons, known as jellium. This approximation assumes that the charge density varies slowly on the atomic scale and it is therefore seen as a uniform gas. The LDA is a good approximation for condensed matter systems. However, when the density varies rapidly the LDA does not give a good approximation. This can be improved by taking the gradient of the local density approximation. This is referred to as the generalised gradient approximation (GGA)[19,20].

There are many different approximations for the functionals outlined above which will be discussed in more detail in **Section 3.7.2.**

3.2.3 Basis Sets

In setting up a molecular wavefunction we normally combine the one electron molecular orbitals ϕ_i. Furthermore, each molecular orbital can be calculated by the

combination of the atomic functions θ_k of each electron, i.e. the linear combination of atomic orbital (LCAO) approximation (equation 3.10)

The atomic wavefunctions θ_k can be described in many ways. The simplest way is to describe an atomic wavefunction is to use the Slater type orbital (STO), which is defined by fitting analytical exponentials to numerical wavefunctions[21]. These have the general form:

$$\theta_k = Ce^{-\zeta r} Y_{lm} \tag{3.18}$$

where C is a normalizing constant, Y_{lm} is the spherical harmonic and l and m are quantum numbers and ζ is the radius of the orbital, zeta. This type of orbital is good for atomic or diatomic systems where high accuracy is required[21].

The main alternative atomic orbital form is called the Guassian type orbital (GTO), which can be given below as:

$$\theta_k = Ne^{-\zeta r^2} Y_{Lm} \tag{3.19}$$

where N is normalizing constant.

The GTO has a zero slope at the nucleus whereas the STO has a cusp, i.e. the behaviour around the nucleus for the GTO is not correct. Another factor relating to the GTO is that its value rapidly falls as we move away from the nucleus and therefore the behaviour away from the nucleus is not well represented. When applying the basis set three times more GTO are required for the accuracy of one STO. The advantage of using GTO is the ease of calculating the integrals, meaning greater computational efficiency[22].

After deciding which atomic function (STO/GTO) is going to be used, the number of atomic functions in each atom needs to be considered. The simplest one is the "minimal" basis set, which uses one wavefunction for each atomic orbital, which is filled. The minimal basis set gives the basic description of the atomic orbital. To improve the basis set the number of wavefunctions can be doubled or tripled and then

it becomes a "double numerical" (DN) or "triple numerical" (TN) basis set respectively. For the basis set, which includes the polarising function, it is called "double numerical polarising" (DNP) basis function. This basis function has been considered in this thesis. For heavier elements when only the valence electrons are considered as discussed below in **Section 3.2.4**, the basis set can be called "double zeta valence" (DZV) or "triple zeta valence" (TZV)[22].

3.2.4 Pseudopotentials

Heavy elements contain many core electrons and therefore they require a large number of basis sets [23]. To overcome this problem the core electrons are represented as a pseudopotential, and only the valence electrons are treated explicitly. This pseudopotential replaces the potential of the nucleus and core electrons by an effective potential, which only acts on the valence electrons. The pseudopotentials are derived from the all electron atomic calculations. The valence electron pseudopotential is required to reproduce the behaviour and properties of the valence electrons in the full calculation. This has the effect of reducing the number of basis functions needed in the calculation without substantial loss of any accuracy in treating the valence shell electrons [23].

3.3 Minimization Methods

After obtaining the force fields either from already published parameters, derived from the force field equations as mentioned in **Section 3.1.3**, or quantum mechanical methods, the structure obtained can then be optimised by applying minimization techniques.

The simplest approach to minimize a structure is to consider an initial conformation and adjust it to get a lower total energy, which can then be further reduced to a minimum value by an iteration method[24]. The number of iterations depends on the nature of the minimization algorithm, the form of the energy function, the curvature of potential energy surface and the number of atoms. One iterative way to minimize the structure is to make a crude search i.e. to make small changes in the geometry of

the structure and check if the energy decreases. But this method is very time consuming and not very efficient. There are many other algorithms, as discussed below, which are more efficient in minimising the total energy of the structure.

3.3.1 Line Search

A line search is the lowest level of sophistication in optimization procedures. The line search changes the coordinates of the structure to a new lower energy structure[24]. The simplest method for a line search is to consider points in a line from the initial coordinates. The line search determines all the energies along one direction before moving to the next one. The minimum is determined along the line of the tangent point to the energy contour as shown in **Figure 3.3**. Therefore each line is orthogonal to the previous one. The actual minimum can be determined by successive iterations. However, these line searches are inefficient[24].

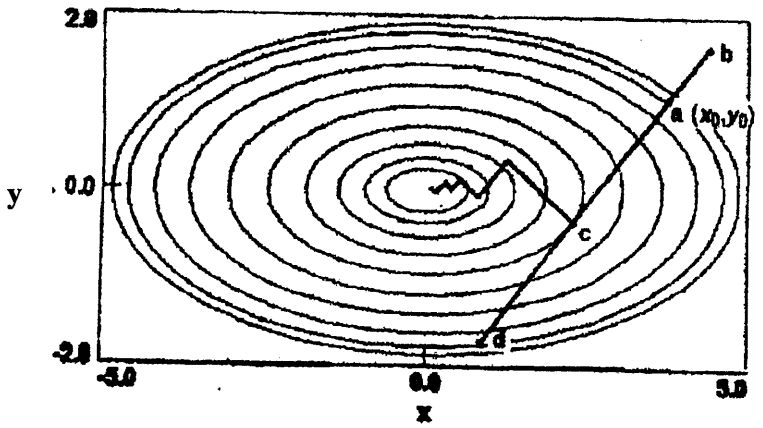

Figure 3.3 The *derivative vector from the initial point $a(x_0y_0)$ defines the line search direction. Note that the derivative vector does not point directly towards the minimum and that the minimum (point c) occurs at the point where the derivative vector is a tangent to the energy contours*[24]

3.3.2 Steepest Descent

The steepest descent method is the simplest derivative method employed to calculate the minimum energy[24]. This approach uses the derivative information to go downhill in the direction of the steepest slope. Once the steepest slope has been chosen, minimization can be done along that direction. This method also employs the line search method (given above) to determine how far it needs to go to establish the minimum. Convergence is slow when it is close to the minimum. However this method is good for minimizing systems which are far away from the minimum.

3.3.3 Conjugate Gradient

The conjugate gradient method is a minimizing technique for finding the nearest local minimum of a function, which presupposes that the gradient of the function can be computed[24]. The method uses conjugate gradients instead of the local gradient for going down hill. If the potential energy surface has a long, narrow shaped valley the minimum is reached in fewer steps than using the steepest descent method. It also applies line searches to get to the minimum, but information from successive searches is not thrown away as it is for the steepest descent minimization. The data are stored and used to shape the rest of the minimization. This algorithm requires more time but it is more efficient.

3.3.4 Newton Raphson

The Newton Raphson method uses both the gradient and the curvature (i.e. second derivative) of the potential energy surface[24]. It uses the gradient method to identify the direction of the search, and then the curvature of the function (second derivative) can be used to determine where the function passes through a minimum along that direction. It is very effective for minimizing energies. However, calculating the curvature of the potential energy surface is rather time consuming so approximations can be applied to speed up the process. One approximation is called the Quasi-Newton-Raphson method, which uses the conjugate gradient method and utilizes previous iterations to direct the minimization along a more efficient pathway. This

method works well on larger systems. The Broyden, Fletcher, Golfarb and Shannon (BFGS) algorithm is one example of the Quasi-Newton-Raphson method and has been applied for all the surface simulations discussed in **Chapter 5**. The algorithm spends a lot of time on each step but it makes the right step[25].

If the molecular energy surface was harmonic then the minimization could occur in one step but generally energy surfaces are not harmonic so the algorithm must be applied iteratively. The iterative Newton Raphson method can be unstable if the conformation is far away from the local minimum such that the potential energy surface is not quadratic. Therefore this is only the most efficient method to determine the minimum when the structure is close to the minimum compared to the conjugate gradient method, which can be applied when the structure is far away from the minimum.

3.4 Bulk Defect Structure Atomistic Calculations

In this thesis, the potential models described above in **Section 3.1.1** have been used to calculate the defect formation energies in $LaCoO_3$. Two kinds of approach have been used to calculate the bulk defect energies, periodic (Supercell method) and aperiodic (Mott Littleton method) which are discussed below.

3.4.1 Supercell Method

In the supercell method a larger unit cell containing the defect is used. The size of the supercell can be increased to 2x2x2 or larger, reducing the defect interactions until a converged energy is obtained. An example of a 2x2x2 supercell for $LaCoO_3$ is given in **Figure 3.4**. The increase in cell size uses more computer resources.

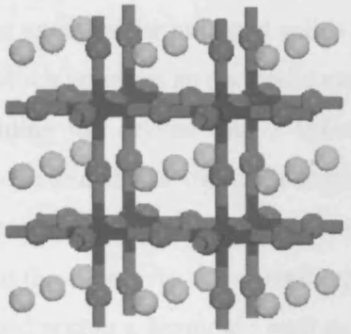

Figure 3.4 *A 2x2x2 supercell for $LaCoO_3$*

The supercell method applies three dimensional Periodic Boundary Conditions (PBC). PBC refers to simulations in a periodic lattice of identical sub units. In the PBC simulation the simulation box is repeated to form an infinite lattice. There are no walls to the central box and therefore the system has no surface effects. Coulombic interactions can be evaluated using the Ewald summation[6].

There are difficulties when charged defects are present and the cell is charged, since the Coulombic summation can then diverge. To overcome this, a uniform background of charge density is needed to compensate for the net charge of the cell. A further difficulty is that periodicity on the defect population is due to the periodic boundary conditions. Moreover, if the supercell contains a pair of charged defects the situation is more difficult as there will be a dipole moment within the unit cell. The interaction between the defects can give a significant contribution but this can be reduced by increasing the size of the supercell.

The supercell method has the advantage that the calculations can be carried out at a higher concentration of defects than is possible in the aperiodic case and the concentration of defects can be varied by varying the supercell size.

3.4.2 Mott Littleton Method

The calculation of defect energies for bulk and solids can also be performed using the Mott Littleton method which involves an aperiodic model[26]. The modelling of defect structures involves dividing the crystal into 3 spherical regions around the defect designated as regions I, IIa and IIb as shown in **Figure 3.5**. In the inner region I all the interactions are treated explicitly at the atomistic level and the ions are allowed to relax fully in response to the defect. In the second region (IIa) the individual ions are assumed to be constrained within a harmonic well as they respond to the force of the defect. In the outer region (IIb) the polarisation of the sub-lattice is considered via a quasi continuum approximation[26].

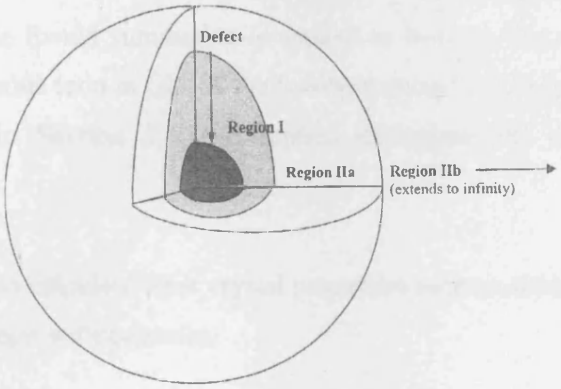

Figure 3.5 *Schematic diagram of the Mott Littleton method dividing the crystal into three regions*[26]

If the vector x represents the displacement of the ions in region I, while ς represents the displacements of the ions in regions II_a and II_b, then the total energy can be given by:

$$E = E_1(x) + E_{12}(x,\varsigma) + E_2(\varsigma) \tag{3.20}$$

where E_1 and E_2 are energies of region I and II_a and II_b together respectively and E_{12} is the interaction of between them. If the inner region is large enough then the outer region consists of a perfect crystal with harmonic displacements[26]. The

minimization of the energy for the defect structure by relaxing the ion positions can be carried out by one of the techniques in **Section 3.3.**

The Mott Littleton method gives the energies of isolated defects as defect clusters.

3.4.3 Methodology for Bulk Defect Structure Calculations

In this thesis the General Utility Lattice Program (GULP) was used to perform simulations on three dimensional ionic solids containing defects in $LaCoO_3$ as discussed in **Section 2.2.3**[27]. GULP is an atomistic code used for the calculations of both periodic lattices, (supercells) and aperiodic (Mott Littleton approach). For the former, symmetry is applied to reduce computational time and, to reduce the error in the Coulombic terms, the Ewald summation is applied to increase the convergence. In addition to the Coulombic term in GULP, the two-body term Buckingham potential function as discussed in **Section 3.1.1** is applied throughout for the atomistic calculations.

GULP can also be used to calculate other crystal properties such as elastic constants, dielectric constant and phonon frequencies.

3.5 Surface Defect Structure Atomistic Calculations

The stability of the surface structure is determined by the surface energy. The surface energy (γ_i) can be calculated from the difference between the energy of the surface block (E_{surf}) and the energy for the same number of bulk ions (E_{bulk}) per unit area:

$$\gamma_i = \left(\frac{E_{surf} - E_{bulk}}{area}\right). \qquad (3.21)$$

The surface energy is therefore the excess energy associated with the surface and needs to be minimized to get the most stable surface. The stability of the surface can be maximized in either of the following ways:

(i) By reducing the amount of surface area exposed.

(ii) By predominately exposing surface planes which have a low surface free energy.

(iii) By altering the local surface atomic geometry in a way, which reduces the surface free energy.

3.5.1 Slab Model

Atomistic calculations for the surface of an ionic solid can be carried out using the slab model. The slab model consists of a 2D slab employing periodic boundary conditions[28]. The cell consists of one or more blocks, which are split into two regions (I and II) as in **Figure 3.6**. Each region consists of structural units, which may be ions or molecules consisting of one or more atoms[28].

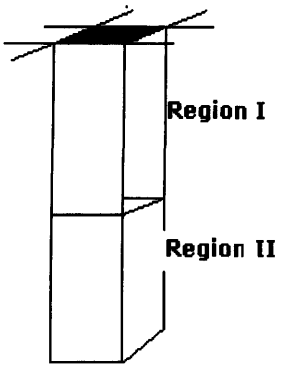

Figure 3.6 *Schematic diagram of the Slab model*[28]

The structure and surface energy of the surface can be obtained by relaxing the ions to their mechanical equilibrium positions, using this two-region approach[28]. The atoms of region I in the surface region are relaxed explicitly so that the resultant structure experiences only small net force whilst those atoms of region II, which are at a set distance from the surface, are kept fixed at their bulk equilibrium positions. The sizes of the regions I and II are chosen such that the surface energy converges[28].

3.5.2 Surface Reconstruction

In order to create a surface for computation there is a need to slice through the bulk structure as in **Figure 3.7**, which shows two possible terminations for the (100) surface of $LaCoO_3$.

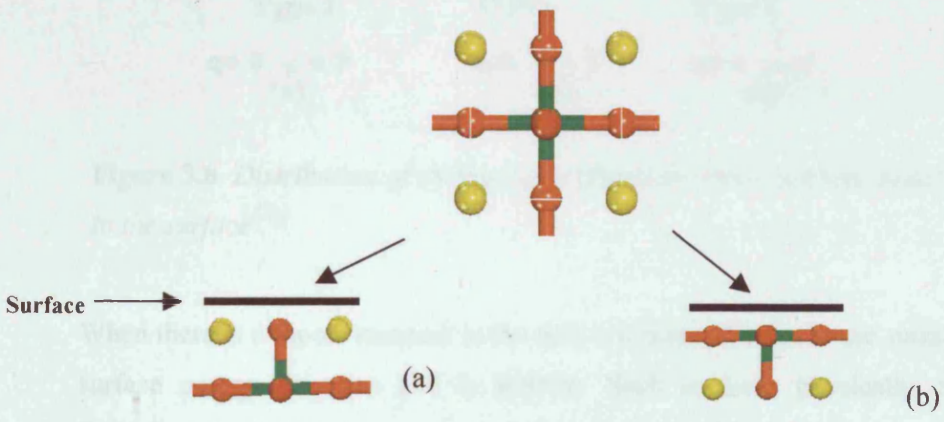

Figure 3.7 *Two terminations for the (100) $LaCoO_3$ surface structure (a) OLa and (b)OCoO termination La^{3+} ion Co^{3+} ion O^{2-} ion*

Tasker identified 3 different possible stacking sequences (**Figure 3.8**) for the exposed surface produced by slicing through the bulk structure [29]. For **Type 1** the surface cell consists of single planes containing anions and cations in a stoichiometric ratio (**Figure 3.8a**). The overall charge is zero. The potential in each plane cancels as the contributions of the sublattices are equal and opposite and there is no dipole moment present. **Type 2** shows a stacking of charged planes. The repeat unit consists of three planes in a symmetrical configuration and hence there is no dipole moment perpendicular to the surface (**Figure 3.8b**). Each plane contributes a term to the potential but the sum over the 3-plane unit cancels the potential to zero and no dipole moment is present. **Type 3** shows a stacking of the sequence of alternating charged planes producing a dipole perpendicular to the surface (**Figure 3.8c**).

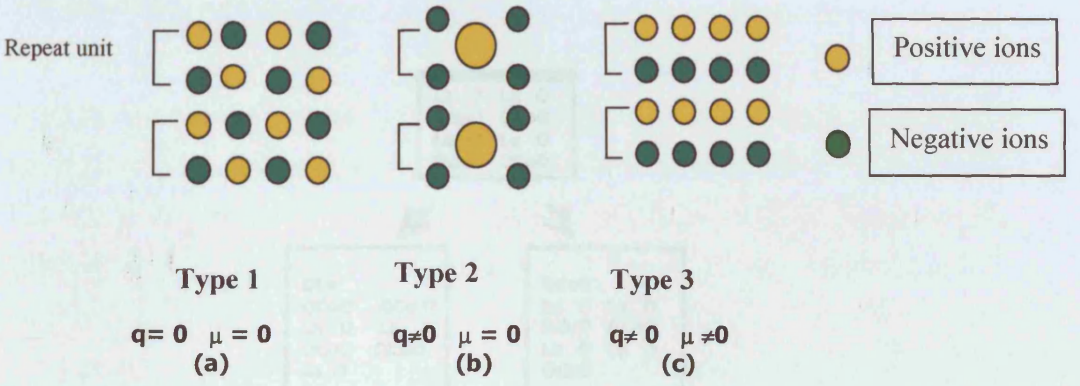

Figure 3.8 *Distribution of charges q on planes for three stacking sequences parallel to the surface*[29].

When there is a dipole moment in the unit cell perpendicular to the surface plane, the surface energy diverges and is infinite. Such surfaces physically cannot exist. Therefore the dipole must be quenched in the z direction. Four mechanisms are possible:

(i) Charge-transfer layer
(ii) Surface reconstruction as discussed below
(iii) Adsorption of foreign atoms
(iv) Electron redistribution

In semiconducting materials, the surface dipole can be quenched by charge transfer in the surface layers. Electron distribution occurs when the material is a semi-conductor and the electrons redistribute in the band gap, so that the dipole is quenched. Such models are not considered in the thesis.

Of the four quenching methods the most realistic approach to quench the dipole for wide band gap materials is to carry out a reconstruction by removing half the ions to an infinite distance below the surface as shown in **Figure 3.9** for the (100) surface of $LaCoO_3$ which gives the two possible surface terminations, OLa and OCoO. The reconstruction process will be discussed in more detail in **Chapter 5**.

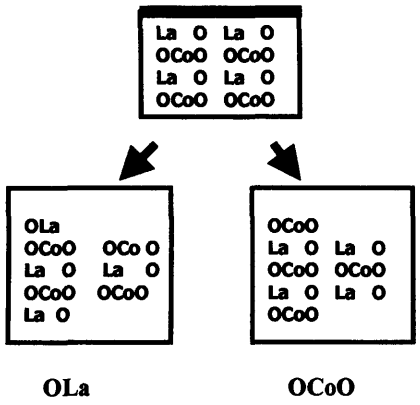

Figure 3.9 *Schematic representation of the stacking sequence for the (100) $LaCoO_3$ surfaces where the surface plane is uppermost.*

3.5.3 Methodology for Surface Defect Structure Calculations

In this work, the computer program MARVIN has been used for the simulations of the surfaces of $LaCoO_3$. The model used in MARVIN is the Slab model which has been discussed in **Section 3.5.1**[28]. The surface simulations are based on the Born model of ionic solids in which the long range Coulombic terms are evaluated for the surface simulations by a plane-by-plane summation procedure due to Parry and the Ewald procedure. Short range interactions are treated exactly the same way and with the same parameters as in the Bulk calculations.

The interatomic potentials used in the surface simulations were directly transferred from GULP calculations as in **Table 3.1** to MARVIN, as it was assumed that the charge and polarisation of the surface ions are similar to the bulk ions. All the structures were relaxed using the Broyden-Fletcher-Goldfarb-Shannon algorithm (BFGS) as discussed in **Section 3.3.4**. Region sizes I and II in the slab model were determined as discussed in **Chapter 5**.

3.6 Potentials Used for the Bulk and Surface Structure

In all the simulations used in this thesis, the cut-off used for the van der Waals term was 12Å. The interatomic potentials were employed from previous simulations of $LaCoO_3$ by Cherry *et al*[30] (**Table 3.1**), which reproduce the observed perovskite structure to within 1% of the lattice parameters. Data for the dopants Sr^{2+} and Ce^{4+} are from Catlow *et al*[9]. The constants *A*, ρ and *C* are defined in **Section 3.1.1** and *Y* and *k* have been discussed above in section **Section 3.1.2.**

Interaction	Short-range parameters			Shell Model	
	A/eV	ρ/Å	C/eVÅ^{-6}	Y(|e|)	k/ eVÅ^{-2}
La^{3+}.... O^{2-}	1545.21	0.3590	0.0	-0.25	145.0
Co^{3+}.... O^{2-}	1329.82	0.3087	0.0	2.04	196.3
O^{2-}.... O^{2-}	22764.30	0.1490	43.0	-2.38	42.0
Sr^{2+}...O^{2-}	959.1	0.3721	0.0	3.251	71..7
Co^{2+}...O^{2-}	3799.3	0.24273	0.0	3.503	110.5
Ce^{4+}...O^{2-}	1986.83	0.3511	20.40	7.7	291.75

Table 3.1 *Interatomic potentials for $LaCoO_3$ perovskites(cut-off)*

A supercell size of 2x2x2 was employed as discussed in **Chapter 4**. For the aperiodic Mott Littleton calculations the sizes of Region I and II were determined as discussed in **Chapter 4.** The energy minimization in GULP was performed using the Newton Raphson method.

3.7 Quantum Mechanical Calculation of the Bulk Defect Structure

Following on from the atomistic defect bulk and surface simulations discussed in **Section 3.4, 3.5** and **3.6** quantum mechanical methods have been employed to investigate the electronic behaviour in the $LaCoO_3$ system. The underlying concepts involved in quantum mechanical calculations have been discussed in detail in **Section 3.2.** In this thesis, the computer program $DMol^3$ has been used for the quantum mechanical simulations of the $LaCoO_3$ structure[31]. $DMol^3$ calculates variational

self-consistent solutions to the density functional theory (DFT) equations, expressed in a numerical atomic orbital basis, which has been discussed in detail in **Section 3.2.3**. The solutions to these equations provide the molecular wavefunctions and electron densities, which can be used to evaluate the energetics and the electronic and magnetic properties of the system. In addition, evaluation of the energy gradients provides a convenient method for determining the equilibrium geometry of the system. In the following different types of calculations, have been carried out, and the options for the choice of exchange correlation function and the structural model and parameters employed in DMol^3.

3.7.1 Spin Restricted and Unrestricted calculations

The molecular wavefunction is the combination of the one electron molecular orbitals which are anitisymmetrized Slater orbitals. The charge density is the sum of the one electron orbitals and is given below:

$$\rho(r) = \sum_i |\phi_i(r)|^2 \qquad (3.22)$$

where the sum is over all the occupied molecular orbitals. The molecular orbitals may be occupied by either a spin up α or a spin down β electron as discussed in **Section 3.2.1**. When the molecular orbitals used for the α electrons and β electrons are the same then the calculation is referred to as a "spin restricted" calculation. However, when different molecular orbitals have been used for the α and β electrons then the calculation is said to be "unrestricted". This will give two charge densities one for α and one for β. In this thesis both types of calculations have been carried out and these will be discussed in detail in **Chapter 7**.

3.7.2 Exchange Correlation Functional

In order to carry out DFT calculations the exchange correlation functional term needs to be approximated has been discussed in **Section 3.2.2**. A number of options for the exchange correlation functional exist. For example, a simple approximation was made by Hedin and Lundvist, which is based on the known exchange correlation

energy of a known uniform electron gas[17]. This is called the local density approximation, which is referred to as LDA. However, LDA underestimates the exchange energy by 10% so giving errors for the correlation energy and therefore the results are not accurate. Becke used a correction term to the local density approximation for the exchange energy, which gives asymptotic behaviour for the energy density[20]. The approximation derived by Vosko et al is the most popular local spin density correlation potential for an electron gas as it can be used for high electron density and it is denoted by VWN[32]. This is used as the default in DMol^3.

To consider the inhomogenity occuring in the molecular system the gradient of the local spin density is chosen which is denoted the non-local density approximation, NLSD. The default used in DMol is due to Perdew and Wang [33] for the correlation functional and one by Becke for the corrected exchange functional, known as the BP functional. Another gradient corrected functional is from Lee, Yang and Parr which is denoted by LYP[34], but this functional cannot predict any parallel spin correlation. In this thesis, initially the default PW91 functional was applied but this was not adequate for the $LaCoO_3$ structure. Therefore, the exchange correlation functional by Perdew, Burke and Ernzerh (PBE) was then applied which gave a more accurate description of the uniform electron gas[35].

3.7.3 DMol^3 calculations

In summary, spin restricted and spin unrestricted calculations have been carried out in DMol^3 on bulk $LaCoO_3$ using the PBE exchange functional. A supercell model depicted in **Figure 3.3** was employed and will be discussed further in **Chapter 7**. The basis sets, which have been employed, are numerical basis sets and have been discussed in **Section 3.2.3**. The basis set employed for $LaCoO_3$ was the double numerical basis set with polarizing functions (DNP) and a real space cut off of 5.5Å. As the La atom is a heavy element and it has many electrons, it is difficult to determine the electron behaviour of all the electrons. Therefore, for the La atoms the outer electrons are treated as the valence electrons and the inner electrons are treated as the core. A semi core local pseudopotential known as density functional semi core pseudo potential (dspp) has been used[36].

REFERENCES

(1) C.R.A.Catlow; E.Kotomin *"Computational Materials Science"*; IOS Press, 2001.
(2) P.M.Morse. *Phys.Rev.* **1929**, *34*, 57.
(3) F.London. *Z.Physik.* **1930**, *63*, 245.
(4) J.E.Lennard-Jones. *Proc.R.Soc.* **1924**, *106*, 463.
(5) T.L.Hill. *J.Chem.Phys.* **1948**, *16*, 399.
(6) P.P.Ewald. *Ann.Phys.* **1921**, *64*, 253.
(7) C.R.A.Catlow *"Computer Modelling of Solids", In : C.R.A.Catlow and W.C.Mackrodt, Lecture notes,* Berlin, 1982; Vol. 166.
(8) B.G.Dick; A.W.Overhauser. *Phys.Rev.* **1958**, *112*, 90.
(9) G.V.Lewis; C.R.A.Catlow. *J. Phys.C:Solid state Phys.* **1985**, *18*, 1149.
(10) C.R.A.Catlow; C.M.Freeman; M.S.Islam; R.A.Jackson; M.Leslie; S.M.Tomlinson. *Phil.Mag.A* **1988**, *58*, 123.
(11) W.C.Mackrodt; R.F.Stewart. *J.Phys.C.Condensed Matter* **1979**, *12*, 431.
(12) W.C.Mackrodt; R.F.Stewart. *J.Phys.C.Condensed Matter* **1979**, *12*, 5015.
(13) R.E.Cohen; L.L.Boyer; M.J.Mehl. *Phys.Rev.B* **1987**, *35*, 5749.
(14) C.R.A.Catlow; In:A.K.Cheetham; P.Day *"Solid State Chemistry:Techniques"*; Oxford University Press, 1986.
(15) D.R.Hartree. *Proc. Cambr. Phil. Soc.* **1928**, *24*, 89.
(16) D.R.Hartree *"The calculation of atomic structures"*; John Wiley & Sons: New York 1957.
(17) W.Kohn; L.J.Sham. *Phys. Rev.* **1965**, *A1133*, 140.
(18) J.P.Perdew; A.Zunger. *Phys.Rev.B.* **1981**, *23*, 5048.
(19) D.C.Langreth; M.J.Mehl. *Phys.Rev.B* **1983**, *28*, 1809.
(20) A.D.Becke. *Phys.Rev.A* **1988**, *38*, 3098.
(21) J.C.Slater; J.W.Connolly. *International Journal of Quantum Chemistry* **1976**, 141.
(22) J.Andzelm; E.Wimmer. *The Journal of Chemical Physics*, *96*, 1280.
(23) D.Vanderbilt. *Phys.Rev.B* **1990**, *41*, 7892.
(24) Cerius[2]"Forcefield-BasedSimulations". *Molecular Simualtion Inc.* **April 2000.**
(25) R.Fletcher *"Practical Methods of Optimisation"*; Wiley: New York, 1980.
(26) N.Mott; M.Littleton. *Trans. Faraday Soc.* **1938**, *34*, 485.
(27) J.D.Gale. *J.Chem.Soc. Faraday Trans.* **1997**, 629.
(28) D.H.Gay; A.L.Rohl. *J.Chem.Soc,Fraday Trans.* **1995**, *91(5)*, 925.
(29) P.W.Tasker. *J.Phys C: Solid State Phys.* **1979**, *12*, 4977.
(30) M.Cherry; M.S.Islam; C.R.A.Catlow. *J. Solid State Chem* **1995**, *118*, 125.
(31) Accelrys.Inc. DMol[3] program, 1996.
(32) S.J.Vosko; L.Wilk; M.Nusair. *Can. J. Phys.* **1980**, *58*, 1200.
(33) J.P.Perdew; Y.Wang. *Phys. Rev B* **1986**, *33*, 8822.
(34) C.T.Y.W.Lee; R.G.Parr. *Phys. Rev B.* **1988**, *45*, 13244.
(35) J.P.Perdew; K.Burke; M.Ernzerhof. *M. Phys. Review Lett.* **1996**, *77*, 3865.
(36) B.Delley. *Phys. Rev B.* **2002**, *66(15)*.

CHAPTER 4

4. ATOMISTIC COMPUTATIONAL STUDIES OF BULK $LaCoO_3$

Mixed metal oxides with the perovskite structure are flexible systems as their properties may be adjusted or enhanced for specific applications by chemical doping at the A or B cation sites as discussed in **Chapter 2**. For example, Sr^{2+} doping at the La site in $LaCoO_3$ is used to enhance its ionic conductivity and catalytic performance by the creation of oxygen vacancies, which influence oxygen adsorption and anion mobility[1]. Alternatively, these oxides can also contain defects in the form of electron holes or traps depending on the identity of the B site cation and the nature of the dopant.

In this chapter, atomistic simulation techniques have been used to investigate bulk defect structure of $LaCoO_3$ whose study is the main theme of the thesis. The GULP code was employed for the treatment of the bulk structure as discussed in **Section 3.4.3**[2]. This approach involves the use of shell model potentials, which have been described in detail in **Sections 3.1.1** and **3.1.2**.

Our initial aim is to carry out simulations of the unit cell of $LaCoO_3$ to validate the interatomic potentials for the simulations by comparison with previous computational data and to develop a methodology for the research. Following this, two kinds of approach have been used to calculate the bulk defect energies as discussed in **Section 3.4**: the periodic supercell method and the aperiodic Mott Littleton method. The research discussed will involve firstly a study of the creation of oxygen vacancies and secondly the effect of cerium doping.

4.1 Validation of the Interatomic Potentials

In order to verify the interatomic potentials static lattice simulations employed in GULP code were applied to the unit cell of $LaCoO_3$. In these calculations the results for the unit cell of $LaCoO_3$ perovskite showed negative frequencies, which are due to the atoms being constrained at the lattice sites in the unit cell. To overcome this

problem the structure was increased to a 2x2x2 supercell and the results obtained from these structures showed positive frequencies thus confirming a true minimum had been attained. **Figure 4.1** shows the comparison between the unrelaxed and relaxed minimized 2x2x2 unit cell structure. This shows distortion of the CoO_6 octahedra as in the real structure, which has a slight rhombohedral distortion and space group $\bar{R}3c$. Using the given potentials, the unit cell parameters for $LaCoO_3$ can be reproduced to within 1% of the experimental data in **Table 4.1**[3]. Therefore it seemed reasonable as a first approach to assume the 2x2x2 structure for all the following periodic simulations.

	Observed (Å)	Calculated (Å)
Lattice constant	3.820	3.822
La-O	2.701	2.703
Co-O	1.910	1.911
O-O	2.701	2.703

Table 4.1 *Calculated and experimental structural parameters for the $LaCoO_3$ structure.*

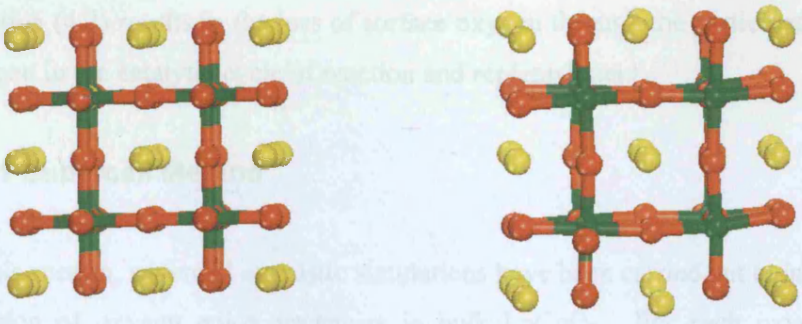

(a) Unrelaxed structure *(b) Relaxed structure*

Figure 4.1 Relaxation *of the 2x2x2 supercell $LaCoO_3$ (Lattice sites are colour coded as La^{3+} O^{2-} Co^{3+})*

4.2. Creation of Oxygen Vacancies in Bulk $LaCoO_3$

Defects such as oxygen vacancies are known to play a fundamental role in adsorption, catalysis and surface morphology as discussed in **Chapter 2**. Therefore, in this thesis atomistic simulation techniques have been employed to investigate the bulk structure of $LaCoO_3$ containing oxygen ion lattice vacancies. To achieve this, oxygen ion vacancies can be introduced according to the two reactions involving doping Sr^{2+} at the La^{3+} site (4.1) and reduction of Co^{3+} to Co^{2+}(4.2) which are shown below according to the Kroger-Vink notation:

Doping Sr^{2+} into the La^{3+} site,

$$2SrO + O_o^x + 2La_{La}^x \rightarrow 2Sr_{La}^{2+} + V_O^{\bullet\bullet} + La_2O_3 \qquad (4.1)$$

Reduction of Co^{3+} to Co^{2+},

$$2Co_{Co}^x + O_O^x \rightarrow 2Co_{Co}^{2+} + V_O^{\bullet\bullet} + 1/2\,O_2 \qquad (4.2)$$

These reactions represent the idealised processes, which are important for suprafacial (4.1) and intrafacial (4.2) oxidation catalysis, which have been discussed in **Section 2.3.2**. Reaction (4.1) generates oxygen vacancies via Sr doping, which is believed to enhance suprafacial catalysis by creation of favoured adsorption sites, whereas reaction (4.2) results in the loss of surface oxygen through the participation of lattice oxygen in the catalytic cycle of reaction and replenishment.

4.2.1 Supercell Method

In this section, supercell atomistic simulations have been carried out to investigate the creation of oxygen anion vacancies in bulk $LaCoO_3$. For each oxygen vacancy created via reaction (4.1), two La sites are substituted by Sr ions and for reaction (4.2) two cobalts ions are reduced to Co^{2+}. Different arrangements of the defects with respect to one another were considered by keeping the oxygen vacancy position fixed and changing the coordinates for the compensating defects. The 2x2x2 supercell was employed for all the simulations. The different structures corresponding to the various dispositions of cation defects with respect to the oxygen vacancy are shown in **Figure**

4.2 and **Figure 4.3**. The original La^{3+} ions in these figures have been omitted for clarity.

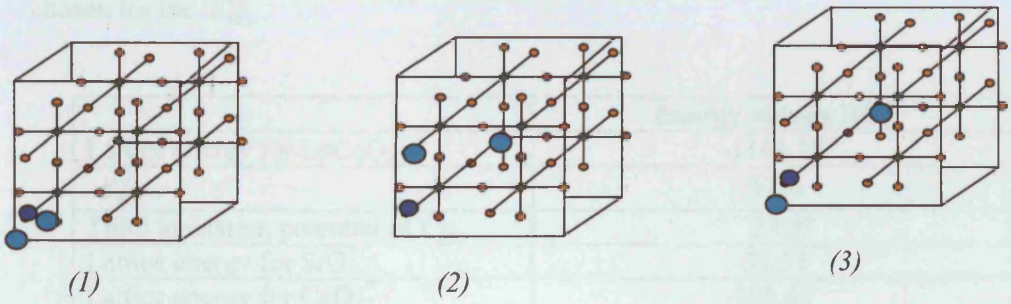

Figure 4.2 *Schematic diagrams for the different structures investigated for reaction (4.1) involving substitution by two Sr^{2+} (●) and creation of an O^{2-} vacancy (●)*

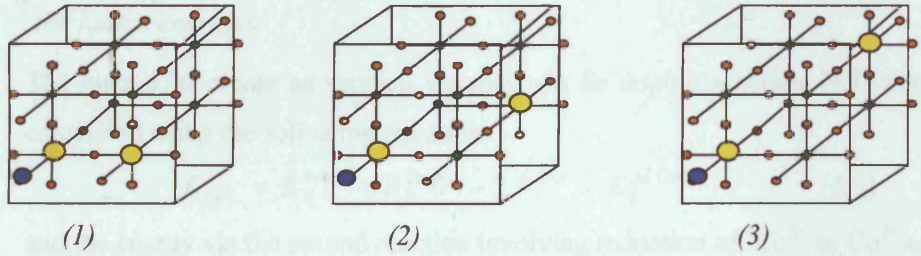

Figure 4.3 *Schematic diagrams for different structures investigated for reaction (4.2) involving reduction of two Co^{3+} to Co^{2+} (●) and creation of an O^{2-} vacancy (●)*

Energies of reactions for the oxygen vacancy creation reactions (4.1) and (4.2) were derived employing the Born Haber cycles from the calculated energies in GULP for each of the energy minimized structures in **Figure 4.2** and **Figure 4.3**. The different energies required to calculate the oxygen vacancy defect energies (E_{VAC}) are the energy of the defect containing $LaCoO_3$ structure (E_L^{DEF}) from the GULP calculations and the lattice energies of $LaCoO_3$, SrO, La_2O_3 and CeO_2 as discussed later, the third ionisation potential of Co (E_{IP}) and the energy to convert doubly charged gaseous oxygen ions to molecular oxygen ($E_{RM}^{O_2}$), i.e. the first and second electron affinities of atomic oxygen and the dissociation energy of molecular oxygen[4]. The above parameters are listed in **Table 4.2**. We should note that while there are limits to the precision for the value of $E_{RM}^{O_2}$, which depends on the environment of the oxide ion, it

has been successfully used in many calculations. In this thesis, comparisons between defect energies are restricted to the series of calculations relative to particular reactions defined by equation (4.1) and (4.2), which are not affected by the value chosen for the $E_{RM}^{O_2}$.

	Energy values (eV)
Lattice energy for $LaCoO_3$	-1144.58
$E_{RM}^{O_2}$	-9.36
Third ionisation potential of Co	33.57
Lattice energy for SrO*	-33.52*
Lattice energy for CeO_2*	-105.64*
Lattice energy for La_2O_3*	-127.34*

Table 4.2. *Energy values for the Born Haber cycle for reactions (4.1) and (4.2). *For the SrO, CeO_2 and La_2O_3 crystal structures the same potentials were used for the calculating the lattice energies.*

The energy to create an oxygen vacancy via Sr doping reaction (4.1) can then be calculated using the following equation:

$$E_{VAC} = E_L^{DEF} + E_L^{La_2O_3} - 2E_L^{SrO} - E_L^{LaCoO_3} \qquad (4.3)$$

and the energy via the second reaction involving reduction of Co^{3+} to Co^{2+}as in reaction (4.2) from the equation

$$E_{VAC} = E_L^{DEF} + E_{RM}^{O_2} - E_L^{LaCoO_3} + 2E_{IP} \qquad (4.4)$$

	Lattice defect energies (eV)
Structure 1	-1081.00
Structure 2	-1081.16
Structure 3	-1081.01

Table 4.3 *Lattice defect energies for creating oxygen vacancies via Sr doping*

	Lattice defect energies (eV)
Structure 1	-1064.29
Structure 2	-1064.83
Structure 3	-1064.16

Table 4.4 *Lattice defect energies for creating oxygen vacancies via reduction of Co^{3+} to Co^{2+}*

The lattice defect energies from the above **Tables 4.3** and **4.4** and equations (4.3) and (4.4) have been used to calculate the defect energies in **Tables 4.5** and **Table 4.6** respectively.

	Sr^{2+} - O Vacancy distances (Å)		Sr^{2+}-Sr^{2+} distances (Å)	Defect energy (eV)
Structure 1	2.73	2.73	3.71	3.21
Structure 2	5.50	4.98	3.83	3.05
Structure 3	2.58	4.82	6.64	3.19

Table 4.5 *Defect energies for creating oxygen vacancies via Sr doping*

	Co^{2+} - O Vacancy distances (Å)		Co^{2+}-Co^{2+} distances (Å)	Defect energy (eV)
Structure 1	5.63	4.36	3.91	3.93
Structure 2	4.78	7.75	5.46	3.38
Structure 3	5.50	4.32	6.62	4.05

Table 4.6 *Defect energies for creating oxygen vacancies via reduction of Co^{3+} to Co^{2+}*

The Sr^{2+}-O^{2-} vacancy separations and Sr^{2+} -Sr^{2+} dopant separations and the Co^{2+}-O^{2-} vacancy separations and Co^{2+}-Co^{2+} distances presented in **Tables 4.5** and **4.6** respectively, give an indication of the attractive distances and repulsive distances between the charged ions as discussed in **Section 4.2.3.** These distances give a representation of the closest attractive and repulsive interactions only.

In **Table 4.5** the separation distance between the Sr^{2+} dopants and O vacancy represents the attractive interaction due to the opposite charges on the defects whereas Sr^{2+}–Sr^{2+} dopant distances give an indication of the repulsive interaction between the Sr^{2+} ion dopants due to the same charges on both defects. The results reveal that the closest configuration (structure (1)) of the charged defects (Sr^{2+} dopants and O vacancy) has a higher energy required to create the vacancy than structure (2) where defects are more separated. Therefore structure (1) would represent a less favourable spatial arrangement of defects for the doping of Sr^{2+}.

Similarly, **Table 4.6** shows the distances between the reduced Co^{2+} ions and the oxygen vacancy, which correspond to the attractive interactions, whereas the distances between the Co^{2+} ions give the repulsive interactions. The results from **Table 4.6** also show that the closest configuration (structure (1)) of the charged defects (Co^{2+} ions and oxygen vacancy) has a higher defect energy than structure (2)

where the defects are separated and as a result structure (1) will be a less favourable structural arrangement for the reduction of Co^{3+} reaction. The defect energy dependence on the disposition of defects is discussed further in **Section 4.2.3.**

4.2.2 Mott Littleton Method

In this section the Mott Littleton method, which has been discussed in **Section 3.4.2,** has been employed to determine the defect energies for creation of oxygen vacancies in bulk $LaCoO_3$ according to reactions (4.1) and (4.2). For the Mott Littleton method the model is partitioned into two regions, I and II, the sizes of which need to be specified[5]. These sizes can be determined from the convergence of the calculated energy with respect to region size, which can be investigated by increasing one region size and keeping the other fixed and then determining the energy difference between each calculation. For example, the defects are put into a calculation with region I being 10Å and region II being 20Å. Then another calculation is done by keeping the defects at the same coordinates but increasing region I to 12Å and keeping region II at 20Å. This procedure is repeated until the difference between the energy in successive calculations is 1%. Similarly the convergence of region II can also be determined by changing the size of region II and keeping all the other coordinates fixed. The results for both reactions for creating oxygen vacancies are given below in **Table 4.7**:

	Calculated Energies					
	Region I Size (Å)			**Region II Size (Å)**		
	10	**12**	**14**	**20**	**22**	**24**
Sr^{2+} doping reaction	2.95	2.92	2.89	2.95	2.95	2.95
Co^{3+} reduction reaction	2.59	2.54	2.49	2.59	2.59	2.59

Table 4.7*Convergence of defect energies (eV) as a function of Mott Littleton region sizes*

The results in **Table 4.7** show that all the simulations for reaction (4.1) can be carried out by considering region I to be at 10Å and region II to be 20Å as there is negligible

difference in the results. Similarly for reaction (4.2) region I was determined to be 10Å and region II 20Å.

We should note that the Mott Littleton calculations in GULP yields a 'defect energy' *(E_{DEF})*, which is equivalent to the differences in lattice energies between defect containing $LaCoO_3$ (E_L^{DEF}) and defect free $LaCoO_3$ ($E_L^{LaCoO_3}$) in equation (4.3) and (4.4). The energy to create an oxygen vacancy *(E_{VAC})* is then derived from the data below in **Tables 4.8** and **4.9** and the two equations for the two reactions under consideration here according to the equations

For Sr^{2+} doping:

$$E_{VAC} = E_{DEF} + E_L^{La_2O_3} - 2E_L^{SrO} \qquad (4.5)$$

For Co^{3+} reduction

$$E_{VAC} = E_{DEF} + E_{RM}^{O_2} + 2E_{IP} \qquad (4.6)$$

This convention applies to all Mott Littleton calculation in this thesis.

	Lattice defect energies (eV) (E_{DEF})
Structure 1	63.32
Structure 2	63.63
Structure 3	64.04
Structure 4	64.46

Table 4.8 *Lattice defect energies for creating oxygen vacancies via Sr doping*

	Lattice defect energies (eV) (E_{DEF})
Structure 1	78.95
Structure 2	80.26
Structure 3	80.94
Structure 4	81.71

Table 4.9 *Lattice defect energies for creating oxygen vacancies via reduction of Co^{3+} to Co^{2+}*

Taking the specified region sizes for each reaction, different spatial disposition of the defects were considered. The oxygen vacancy was fixed at the centre of the defect cluster and the other compensating defects were positioned at different distances away from the centre as specified in **Tables 4.10** and **4.11** for the two reactions for creating oxygen vacancies. The calculated defect energies (for creating vacancies for both reactions, E_{VAC} in equations (4.3) and (4.4) are also given below in **Tables 4.10** and **4.11**.

	Sr^{2+} - O Vacancy distances (Å)		Sr^{2+}-Sr^{2+} distances (Å)	Defect energy (eV)
Structure 1	2.82	2.82	5.54	2.95
Structure 2	4.72	4.72	8.60	3.26
Structure 3	7.17	7.17	14.33	3.68
Structure 4	8.98	8.98	18.02	4.10

Table 4.10 *Defect energy for creation of oxygen vacancies via Sr doping reaction*

	Co^{2+} - O Vacancy distances (Å)		Co^{2+}-Co^{2+} distances (Å)	Defect energy (eV)
Structure 1	2.04	2.04	3.87	2.59
Structure 2	4.25	4.25	8.52	3.90
Structure 3	5.74	5.74	11.48	4.44
Structure 4	6.88	3.88	13.77	5.21

Table 4.11 *Defect energy for creation of oxygen vacancies via Co^{3+} to Co^{2+} reduction reaction*

For the Mott Littleton method, the Sr^{2+}-O vacancy separations and Sr^{2+}-Sr^{2+} dopant separations and the Co^{2+}-O vacancy separations and Co^{2+}- Co^{2+} distances presented in **Tables 4.10** and **4.11** respectively, give an indication of the defect interaction. Unlike the supercell calculation it would appear that the most stable structures results from situations where the compensating defects are closest together. This behaviour is discussed in **Section 4.2.3**.

The calculated results from the supercell (**Tables 4.5** and **4.6**) and Mott Littleton (**Tables 4.10** and **4.11**) methods for the energy required to create an oxygen vacancy via Sr^{2+} doping at the La^{3+} site or reduction of Co^{3+} are in approximate agreement with one another given the different nature of the two models. The Mott Littleton value of 2.95eV in **Table 4.10** for Sr^{2+} doping is also in reasonable agreement with the previous Mott Littleton calculations by Islam *et al* of 3.58eV[1]. The lower value calculated in this thesis is a result of the cluster defect model employed compared to calculations in the previously published work for non-interacting defects.

Comparing both reactions it is tempting to suggest that it is easier to create an oxygen vacancy by reduction of Co^{3+} to Co^{2+} than Sr^{2+} doping. However the accuracy of some of the parameters included in equations (4.3) and (4.4) for determining the defect energy to create an oxygen vacancy are probably not sufficient for this purpose.

4.2.3 Influence of the Interaction Between Defects on Stability

Arguments based simply on Coulombic interaction between the defects would lead us to expect that the closer the Sr^{2+} substituted cations or Co reduced cations are to the oxygen vacancy, the greater the stability of the structure. However, from **Table 4.5** for the supercell calculations it can be seen that the solubility of Sr is slightly more favoured for structure (2) where the compensating defects are more separated in a single unit cell compared to the other structures (1) and (3). Similarly for reaction (4.2) involving Co^{3+} reduction, for the supercell method **Table 4.6** indicates that structure (2) is more favoured compared to the other structures (1) and (3). These results show that the nature of defect interaction is more complex as has been found on many other systems. Therefore other methods of analysis need to be considered to determine which factors could influence the stability of the structure.

A helpful approach is to consider the sites where the charge has changed and an 'effective charge lattice' is created. In relation to the work under discussion here, the effective charge lattice model was created by increasing the size of the unit cell as shown below in **Figures 4.4** and **4.5** which allows us to look carefully at the lattice structure.

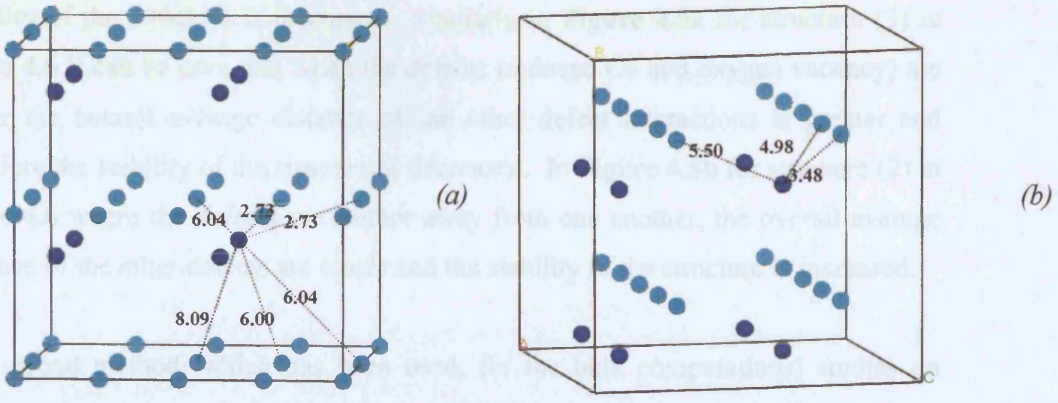

Figure 4.4 *Lattice structures for (a) the least and (b) the most stable arrangement in the "effective charge model". ( ) is the Sr dopant and ( ) is the oxygen vacancy*

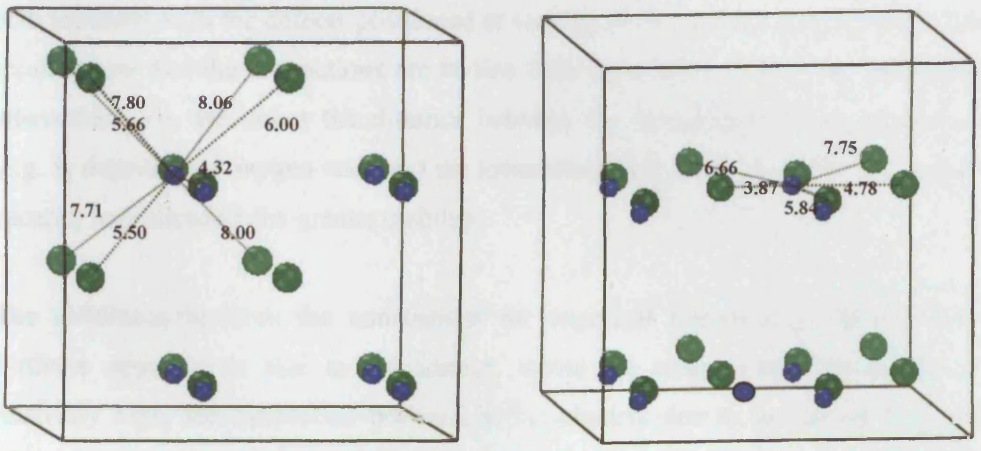

(a) *(b)*

Figure 4.5 *Lattice structures for (a) the least and (b) the most stable arrangement in the "effective charge model". ( ) is the reduced Co^{3+} and ( ) is the oxygen vacancy*

Figures 4.4 and **Figure 4.5** depict the most stable and least stable structures for reactions (4.1) and (4.2) respectively. These models show all the interactions between the effective charges and the distances between all the effective charges can then be measured. The models in **Figure 4.4** for structures (1) and (2) in **Table 4.5** reveal that the closer the substituting strontium and oxygen vacancy in a particular cluster are together, the further apart are the average distances between the other defects in the effective charge lattice and therefore the stability of the structure is decreased. These models also illustrate that as the defects are moved further apart as in **Figure 4.4b**, the average distances between many of the effective charges are reduced and the stability of the structure is increased. Similarly in **Figure 4.5a** for structure (3) in **Table 4.6** it can be seen that when the defects (reduced Co and oxygen vacancy) are closer the overall average distance of the other defect interactions is greater and therefore the stability of the structure is decreased. In **Figure 4.5b** for structure (2) in **Table 4.6** where the defects are further away from one another, the overall average distance of the other defects are closer and the stability of the structure is increased.

The second method, which has been used, for the bulk computational studies on creation of oxygen vacancies in $LaCoO_3$ is the Mott Littleton method. For reactions (4.1) involving Sr^{2+} doping and (4.2) involving Co^{3+} reduction the results have been

tabulated in **Tables 4.10** and **4.11** respectively. The calculations were carried out for both reactions with the defects positioned at varying distances from one another. The results show that the interactions are in line with expectations based on Coulombic interactions, i.e. the closer the distance between the defects with opposite charges (e.g. Sr dopants and oxygen vacancy) the lower the defect energy to create the oxygen vacancy and therefore the greater stability.

The difference between the conclusions for supercell calculations and the Mott Littleton approach is that in the former, where the concentration of defects is relatively high, the interaction between defect clusters due to periodicity must be taken into account, whereas in the latter the defect cluster can be considered as an isolated entity.

4.3 Cerium Doping in Bulk Stoichiometric $LaCoO_3$

Doping is important in modifying the catalytic behaviour of $LaCoO_3$, which has been discussed briefly in **Section 2.2.3**. Doping with enhanced catalytic effects can occur both by divalent ion (e.g. Sr^{2+}) substitution or tetravalent ion (Ce^{4+}) substitution at the La site. While the effect of Sr^{2+} is relatively well understood experimentally and theoretically in terms of compensating oxygen ion lattice vacancies, the interpretation of the effect of Ce^{4+} doping is complicated by formation of mixed phase materials with segregation of CeO_2[1]. Therefore the following section focuses on atomistic calculations for doping cerium in bulk $LaCoO_3$. Both the supercell and Mott Littleton methods have been applied using the computer program GULP and incorporating interatomic potentials derived from previous studies as discussed in **Section 3.1.1** and **3.1.2**. Two doping reactions have been considered, The first involves doping cerium at the La site, which is then compensated by creating lanthanum vacancies as shown according to the Kroger-Vink notation:

$$3CeO_2 + 4La_{La}^{x} \rightarrow 3Ce_{La}^{\bullet} + V_{La}^{'''} + 2La_2O_3, \qquad (4.8)$$

The second involves the substitution of Ce at the La site, which is compensated by the reduction of a Co^{3+} to Co^{2+} as shown according to the Kroger-Vink notation:

$$4CeO_2 + 4La_{La}^{x} + 4Co_{Co}^{x} \rightarrow 4Ce_{La}^{\bullet} + 4e' + 2La_2O_3 + O_2 \qquad (4.9)$$

4.3.1 Supercell Method

In this section, atomistic simulations have been carried out for reactions (4.8) and (4.9) describing dissolution of cerium in the $LaCoO_3$ lattice resulting in creation of lanthanum vacancies or reduction of Co^{3+} to Co^{2+} respectively. For reaction (4.8), three Ce ions are substituted at La sites which, are compensated by creation of a lanthanum vacancy and for reaction (4.9) one Ce ion is substituted at the La site while one cobalt is reduced. A 2x2x2 supercell was employed for all the simulations and different arrangements of the defects with respect to one another were considered. The different structures modelled are illustrated below in **Figures 4.6** and **4.7**. The original La^{3+}ions in the figures below have been omitted for clarity.

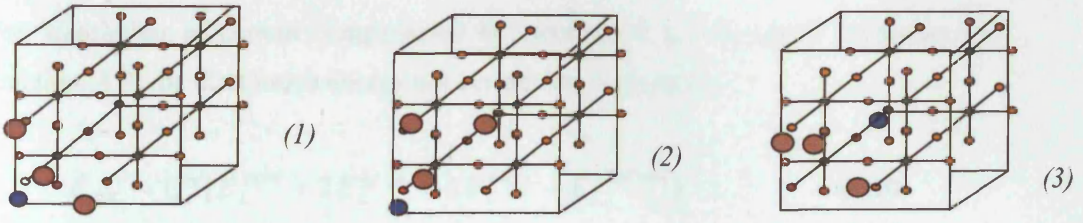

Figure 4.6 *Schematic diagrams for the different structures investigated for reaction (4.8) involving substitution of 3 Ce ( ) and creation of a La^{3+} vacancy ( ).*

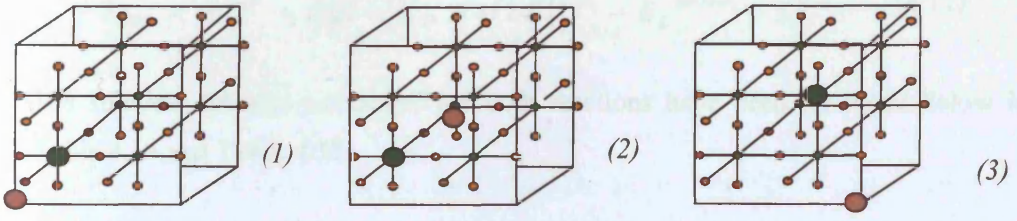

Figure 4.7 *Schematic diagrams for the different structures investigated for reaction (4.9) involving substitution of one Ce ion ( ) and reduction of a Co^{3+} to Co^{2+} ( )*

Solution energies were obtained for each of the energy minimized structures in **Figure 4.6** and **Figure 4.7**. These defect reactions are fully balanced equations, and therefore the Born Haber cycle can be applied to derive the solution energies. The different energies required to calculate the cerium solution energies (E_{SOL}) are the

defective lattice energy E_L^{DEF} of the doped $LaCoO_3$ structure derived from GULP calculations shown in **Tables 4.12** and **4.13**, the lattice energies (E_L) of $LaCoO_3$, CeO_2 and La_2O_3, the third ionisation potential of Co (E_{IP}) and the removal of lattice oxygen $E_{RM}^{O_2}$ (electron affinity of oxygen + dissociation of oxygen), which are given in **Table 4.2**.

	Lattice defect energies (eV)
Structure 1	-1196.78
Structure 2	-1200.00
Structure 3	-1199.89

Table 4.12 *Lattice defect energies for Ce doping accompanied by creation of La vacancies*

	Lattice defect energies (eV)
Structure 1	-1145.57
Structure 2	-1145.57
Structure 3	-1145.57

Table 4.13 *Lattice defect energies for cerium doping accompanied by reduction of Co^{3+} to Co^{2+}*

For dissolution of cerium compensated by creation of La vacancies according to reaction (4.8) the dissolution energy per cerium ion is given by:

$$E_{SOL} = 1/3[E_L^{DEF} + 2E_L^{La_2O_3} - 3E_L^{CeO_2} - E_L^{LaCoO_3}] \qquad (4.10)$$

Similarly, for reaction (4.9) where Ce^{4+} substitution is compensated by Co^{3+} reduction the dissolution energy per cerium ion is given by:

$$E_{SOL} = E_L^{DEF} + E_{RM}^{O_2} + E_{IP} + 1/2E_L^{La_2O_3} - E_L^{LaCoO_3} - E_L^{CeO_2} \qquad (4.11)$$

The solution energies calculated for both reactions have been tabulated below in **Table 4.14** and **Table 4.15**.

	Ce^{4+} - La Vacancy distances (Å)			Ce^{4+}-Ce^{4+} distances (Å)	Solution energy (eV)
Structure 1	3.82	3.82	3.82	5.33	3.34
Structure 2	5.36	5.36	6.59	3.80	2.27
Structure 3	3.81	5.34	3.79	6.55	2.30

Table 4.14 *Solution energies for Ce doping accompanied by creation of La vacancies*

	Ce^{4+} - Co^{2+} distances (Å)	Solution energy (eV)
Structure 1	3.34	2.79
Structure 2	3.23	2.79
Structure 3	3.37	2.79

Table 4.15 *Solubility for cerium doping accompanied by reduction of Co^{3+} to Co^{2+}*

For reaction (4.8) it can be seen from results in **Table 4.14** for doping Ce^{4+} and creating La vacancies that when the defects are closest to one another as in structure (1) the stability of the structure is decreased compared to structure (2) where the defects are further apart. This effect is similar to that observed for supercell calculations involving Sr^{2+} doping in **Section 4.2.1** and will be discussed further in **Section 4.3.3** in relation to the effective charge model.

For reaction (4.9) the results in **Table 4.15** for doping Ce^{4+} by reduction of Co^{3+} gives only one solution energy due to the periodicity within the structure which dictates that the distances between the optimised defects are approximately the same wherever the defects are positioned.

4.3.2 Mott Littleton Method

The Mott Littleton method has been employed to determine the solution energies for cerium in $LaCoO_3$ by the two processes which are given in reactions (4.8) and (4.9). For both reactions the sizes of the Mott Littleton regions need to be specified which can be done by checking the solution energy convergence for each reaction as discussed in **Section 4.2.2** while increasing the size of one region and keeping the other fixed. The results for both reactions (4.8) and (4.9) are given below in **Table 4.16**:

	Calculated Energies					
	Region I Size Å			Region II Size Å		
	10	12	14	20	22	24
Lanthanum vacancy reaction	2.70	2.67	2.64	2.70	2.70	2.70
Co^{3+} reduction reaction	2.64	2.63	2.62	2.64	2.64	2.64

Table 4.16 *Convergence data (eV) as a function of Mott Littleton region sizes*

The results in **Table 4.16** show that all the simulations for reaction (4.8) and (4.9) can be carried out by considering region I to be 10Å and region II to be 20Å since 1% difference in the calculated solution energies between the consecutive increases in region sizes is assumed to have negligible effect on the conclusions. The lattice defect energies needed to calculate the solution energies for reaction (4.8) and (4.9) are shown in **Tables 4.17** and **4.18**.

	Lattice defect energies (eV)
Structure 1	-54.14
Structure 2	-53.69
Structure 3	-52.49
Structure 4	-52.04

Table 4.17 *Lattice defect energies for doping Ce^{4+} compensated by the creation of lanthanum vacancies*

	Lattice defect energies (eV)
Structure 1	-1.14
Structure 2	-1.10
Structure 3	-1.05
Structure 4	-0.30

Table 4.18 *Lattice defect energy for Ce doping via Co^{3+} to Co^{2+} reduction reaction*

Taking the specified region sizes for each reaction, different arrangements of defects were considered. The lanthanum vacancy was fixed at the centre of the defect cluster and the other compensating cerium ions were positioned at different coordinates away from the centre as specified in **Tables 4.19** for reaction (4.8). For reaction (4.9) the cerium dopant was fixed at the centre and the reduced cobalt was positioned at different distances away from the centre as given in **Table 4.20**:

	Ce^{4+} - La Vacancy distances(Å)			Average Ce^{4+}-Ce^{4+} distances (Å)	Solution energy (eV)
Structure 1	3.68	3.68	3.68	5.44	2.70
Structure 2	5.35	5.35	6.55	9.30	2.85
Structure 3	5.35	8.52	8.52	7.64	3.25
Structure 4	9.33	9.33	9.33	10.05	3.40

Table 4.19 *Solution energies for doping Ce^{4+} compensated by the creation of lanthanum vacancies*

	Co^{2+} - Ce dopant distances(Å)	Solution energy (eV)
Structure 1	3.26	2.64
Structure 2	6.30	2.70
Structure 3	8.33	2.73
Structure 4	9.91	3.47

Table 4.20 *Solution energy for Ce doping via Co^{3+} to Co^{2+} reduction reaction*

For the Mott Littleton method the Ce^{4+}-La vacancy separations and Ce^{4+}-Ce^{4+} dopant separations and the Ce^{4+}-Co^{2+} separations presented in **Tables 4.19** and **4.20** respectively, give an indication of the attractive and repulsive distances between the charged ions as discussed in **Section 4.3.3.** From **Table 4.19** and **4.20** we see that when the compensating defects are closer together, the stability of the structures is greater compared to when the defects are moved further away. This effect will be discussed further in **Section 4.3.3.**

A comparison between the solution energy results from supercell and Mott Littleton calculations in **Tables 4.14** and **4.15** and **Tables 4.19** and **4.20** respectively for both reactions (4.12) and (4.13) involving La vacancy creation or reduction of $Co^{3+}$are in reasonable agreement. Overall the results confirm previous Mott Littleton computational data listed in **Table 4.21** and experimental observations that Ce is not very soluble in $LaCoO_3$ via either reaction as discussed in **Section 2.2.3.2** and is attributed to the cation radius mismatch between Ce^{4+}(1.14Å) and La^{3+} (1.36Å)[6].

	Ce^{4+} solution energies (eV)	
Reaction	**Isolated defects**	**Defect Clusters**
La vacancy creation reaction (4.8)	2.89*	2.70
Co reduction reaction (4.9)	2.69*	2.64

Table 4.21 *Comparison of the calculated Mott Littleton solution energies for solubility of Ce^{4+} in bulk $LaCoO_3$. *Results from French et al*[5]*

4.3.3 Effective Charge Model for the Interaction Between Defects

Once again we find that to understand the nature of the defect interaction we need to take into account periodicity from **Table 4.14**. For the supercell calculations it can be seen that solubility of Ce^{4+} is slightly more favoured for structure (2), although this structure shows a greater distance between the defects (Ce dopants and lanthanum vacancy) in a single unit cell compared to other structures. However the results in **Table 4.14** do not give a complete representation of all the interactions between the defects in a supercell calculation. Therefore the alternative method discussed in **Section 4.2.3** was considered to determine what factors affect the stability of the structure.

Only sites are considered where the charge has changed and an 'effective charge lattice' is created. For better visualisation of the interaction between the defects in the effective charge lattice model, the size of the unit cell was increased as shown below in **Figures 4.8** for structures (1) and (2) in **Table 4.14** so that all the distances between the defects could be measured within the lattice structure.

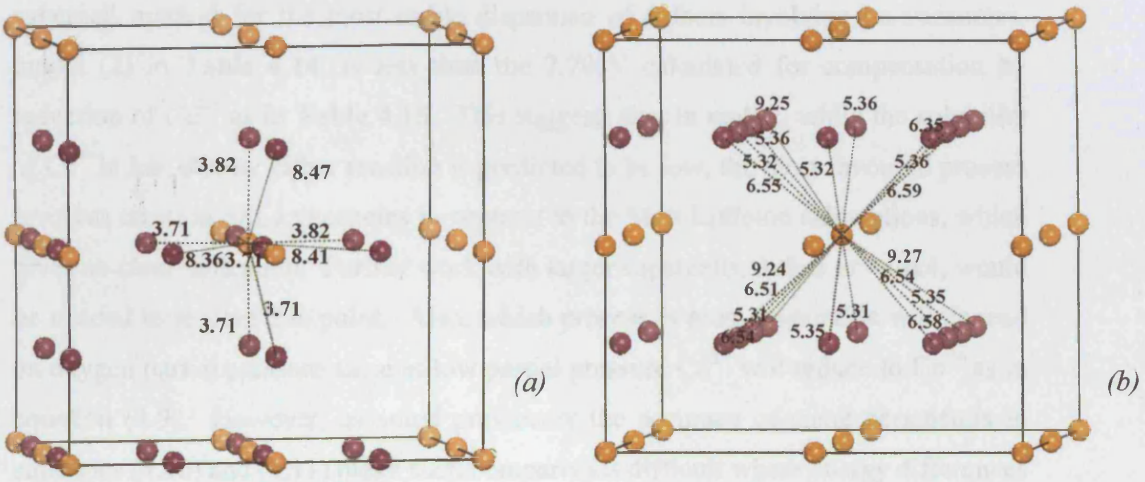

Figure 4.8 *Lattice structures for (a) the least and (b) the most stable arrangement in the "effective charge model". ( ) is the Ce dopant and ( ) is the lanthanum vacancy*

Figures 4.8 illustrates the least stable and most stable structures, (1) and (2) respectively in **Table 4.14**, for reaction (4.8). These models show all the interactions between the effective charges and the distances between all the effective charges. The models in **Figure 4.8a** reveals that although the substituted Ce^{4+} and lanthanum vacancy are closer together, there are fewer interactions between the effective charges and therefore the stability of the structure is decreased. **Figure 4.8b** shows that although the defects are further apart, there is a greater number of interactions between the defects which causes the stability of the structure to increase.

The second method, which, has been used, for the bulk studies on doping cerium in $LaCoO_3$ is the Mott Littleton method. The solution energy results for reactions (4.8) involving Ce^{4+} doping and creating a lanthanum vacancy and reaction (4.9) where Ce^{4+} doping is compensated by Co^{3+} reduction have been tabulated in **Tables 4.19** and **4.20** respectively as a function of the disposition of the defects with respect to one another. The results for both reactions show that the interactions follow Coulomb's law, i.e. the closer the distance between the defects with opposite charges (e.g. Ce dopant and lanthanum vacancy) the lower the solution energy to create the lanthanum vacancy.

Finally it would seem that the Ce^{4+}solution energy of 2.27eV calculated by the supercell method for the most stable dispersion of defects involving La vacancies, model (2) in **Table 4.14**, is less than the 2.79eV calculated for compensation by reduction of Co^{3+} as in **Table 4.15**. This suggests that in reality, while the solubility of Ce^{4+}in $LaCoO_3$ by either reaction is predicted to be low, the most favoured process involves creation of La vacancies in contrast to the Mott Littleton calculations, which gives no clear indication. Further work with larger supercells, 3x3x3 or 4x4x4, would be needed to resolve this point. Also, which process is most favourable will depend on oxygen partial pressure since at low partial pressure Co^{3+} will reduce to Co^{2+} as in equation (4.9). However, as noted previously the accuracy of some parameters in equations (4.10) and (4.11) make such comparisons difficult where energy differences are small.

4.4 Cerium Doping in Non-Stoichiometric $LaCoO_3$

As discussed in **Section 4.3**, Ce^{4+} has been doped into bulk stoichiometric $LaCoO_3$ creating lanthanum vacancies via reaction (4.8) or reduction of Co^{3+} to Co^{2+} via reaction (4.9). However, as prepared $LaCoO_3$ calcined at $\geq$ 900°C is typically slightly reductively non-stoichiometric. Therefore a third reaction has been considered where Ce^{4+} is doped into the $LaCoO_3$ lattice containing oxygen vacancies, resulting in filling of those vacancies according to equation (4.12):

$$2La_{La}^{x} + 2CeO_2 + V_O^{\bullet\bullet} \rightarrow 2Ce_{La}^{\bullet} + La_2O_3 + O_O^{x} \qquad (4.12)$$

Initially in **Section 4.2**, calculations were carried out on the creation of oxygen vacancies accompanied by the reduction of two Co^{3+} ions to Co^{2+} according to reaction (4.9). In this section oxygen will be inserted back into the structure, which will be compensated by two ceriums as shown by reaction (4.12). The solution energy (E_{SOL}) per ion for Ce doping into non-stoichiometric $LaCoO_3$ via reaction (4.12) is then given by:

$$E_{SOL} = 1/2[E_L^{DEF} + E_L^{La_2O_3} - 2E_L^{CeO_2} - E_L^{NS}] \qquad (4.13)$$

where E_L^{DEF} is the lattice energy of the Ce containing defect structure derived from GULP and the values are given in **Table 4.23**, E_L are the lattice energies of CeO_2 and La_2O_3 from **Table 4.2** and E_L^{NS} is the lattice energy of the oxygen vacancy defect $LaCoO_3$ structure derived from GULP as in **Section 4.2** are in **Table 4.22**.

	Non-stoichiometric lattice energies (eV)
Structure 1	82.13
Structure 2	80.18
Structure 3	80.03
Structure 4	79.25
Structure 5	78.35

Table 4.22 *Lattice defect energy for the non-stoichiometric structure*

	Lattice defect energies (eV)
Structure 1	0.10
Structure 2	-0.93
Structure 3	-0.21
Structure 4	-0.15
Structure 5	-0.61

Table 4.23 *Lattice defect energy for Ce doping and oxygen filling reaction*

Only Mott Littleton calculations have been carried out here, i.e. for the dilute dopant case. As in previous calculations in this chapter, solution energies were carried out as a function of disposition of the individual defects with respect to one another. The refilled oxygen vacancy was placed at the centre of the defect cluster and the dopant Ce^{4+}cations (designated Ce_1 and Ce_2) and compensating Co^{2+} cations (designated Co_1 and Co_2) at different distances from the centre as presented in **Table 4.24**. The region sizes for the Mott Littleton method were defined as 10Å for region I and 20Å for region II as in previous calculations.

The results for the non-stoichiometric calculations are tabulated in **Table 4.24**. The solution energy data indicate that the most favourable case, with energy of 0.95eV, is when Ce^{4+} cations are closest to the refilled vacancy site and the Co^{2+} ions are further away. An explanation here could be that the refilled oxygen site is more stabilised by the proximity of the two highly oxidized Ce^{4+} ions than by the Co^{2+} ions.

	Distances between defect cations and filled oxygen site (Å)				Solution energy (eV)
	Co_1	Co_2	Ce_1	Ce_2	
Structure 1	9.56	9.56	2.79	2.79	0.95
Structure 2	9.56	9.56	9.75	6.25	1.41
Structure 3	4.25	4.25	9.75	6.25	1.85
Structure 4	1.96	1.94	2.79	2.78	2.27
Structure 5	1.96	1.94	9.75	6.25	2.49

Table 4.24 *Solution energy for Ce doping and oxygen filling reaction*

This favourable solution energy is in agreement with previously reported simplified Mott Littleton calculations in **Table 4.25** showing greater solubility in the non-stoichiometric oxygen deficient $LaCoO_3$ than stoichiometric $LaCoO_3$. Therefore, the amount of Ce incorporation can be considered to be dependent on the level of reductive non-stoichiometry induced under conditions for a typical high temperature preparation. This has been estimated to be ~ 5% (x = 0.05).

It is important to remember that the above computational simulation represents the product of a one pot preparation involving air calcination at ≥900°C of precursor material; precipitated from solution. Also, the solution energies in **Table 4.24** are calculated relative to the fully relaxed non-stoichiometric $LaCoO_3$ as in equation (4.13)[6].

	Ce^{4+} solution energies (eV)	
Reaction	**Isolated defects**	**Defect Clusters**
La vacancy creation reaction (4.8)	2.89*	2.70
Co reduction reaction (4.9)	2.69*	2.64
Oxygen vacancy filling (4.12)	0.23*	0.95
Ce and Sr Co-doping reaction (4.14)	1.98	2.84

Table 4.25 *Comparison of the calculated Mott Littleton solution energies for solubility of Ce^{4+} in bulk $LaCoO_3$. *Results from French et al*[5]*

4.5 Cerium Co-doping with Sr in $LaCoO_3$

Finally, calculations have also been carried out on co-doping Sr^{2+} and Ce^{4+} at the La site in $LaCoO_3$, as shown in the following reaction:

$$CeO_2 + SrO + 2La_{La}^{x} \rightarrow Ce_{La}^{\bullet} + Sr_{La}^{'} + La_2O_3 \qquad (4.14)$$

since experimentally, in general terms, the method of doping pairs of cations to achieve a charge balance has been widely employed and computationally it has been confirmed that this approach can result in more favourable solution energies.

For dissolution of cerium compensated by doping of Sr^{2+} ions according to reaction (4.14) the dissolution energy per cerium ion is given by:

$$E_{SOL} = [E_L^{DEF} + E_L^{La_2O_3} - E_L^{CeO_2} - E_L^{SrO}] \qquad (4.15)$$

where E_L^{DEF} is the lattice energy of the Ce containing defect structure derived from GULP are shown in **Table 4.26**, and E_L are the lattice energies of CeO_2, SrO and La_2O_3 from **Table 4.2**. Only Mott Littleton calculations have been carried out here, and only the dilute case is considered in **Table 4.27**. The solution energies for co-doping Ce^{4+} and Sr^{2+} were calculated as a function of the disposition of the dopants with respect to one another. The Ce^{4+} was placed at the centre and Sr^{2+} was moved to different distances away from it as indicated in **Table 4.27**. The region sizes for the Mott Littleton method were defined as 10Å for region I and 20Å for region II as in previous calculations.

	Lattice defect energies (eV)
Structure 1	-8.93
Structure 2	-8.87
Structure 3	-8.69

Table 4.26 *Lattice defect energy for Ce co-doping with Sr^{2+} reaction*

The solution energy data in **Table 4.27** indicates the most favourable case for co-doping, with a value of 2.84eV per Ce ion dopant ion, is when the two dopants are closest together. In this situation the attraction between the effective charges at the two sites provides optimum stabilisation according to Coulomb's law.

	Sr^{2+} - Ce dopant distances (Å)	Solution energy (eV)
Structure 1	3.83	2.84
Structure 2	5.43	2.94
Structure 3	8.56	3.02

Table 4.27 *Solution energy for Ce co-doping with Sr^{2+} reaction*

However, the value of 2.84eV per Ce^{4+} ion calculated here indicates that Ce^{4+} co-doping with Sr^{2+} is not a particularly favourable process for incorporating Ce^{4+} itself. Presumly the ionic radius difference between Ce^{4+} (1.14Å) and La^{3+} (1.36Å) discussed in **Section 2.2.3.2** outweighs the advantage of balancing the charge with Sr^{2+}(1.44Å). Interestingly, the solution energy of 2.84eV is very similar to that calculated for reaction (4.9) (2.64eV) where Ce^{4+} is compensated by Co^{2+} formation. This may be fortuitous since the detailed geometry of the defect cluster will be different. The doped Sr^{2+} occupies a perovskite A-site while Co^{2+} occupies a B-site.

It is also worth noting that the value of 2.84eV is considerably higher than the 1.98eV calculated by the simplified Mott Littleton approach involving insertion of individual defects. This discrepancy arises because the simplified approach does not take into account the defect interactions, which are simulated in the defect cluster model employed elsewhere throughout this thesis.

4.6 Summary and Conclusions

Two different approaches have been used to calculate the defect energies in bulk $LaCoO_3$: The supercell method and the Mott Littleton method. Broadly the Mott Littleton calculations relates to dilute, isolated defect clusters and the supercell calculations are concerned more with concentrated dopant situations where defect interactions can be studied. The reason for these calculations was to determine the

factors, which could affect the ease of creation of oxygen vacancies or the solubility of cerium in $LaCoO_3$, two factors which are considered important in influencing catalytic behaviour.

The results for the supercell method for creating the oxygen vacancies and for Ce^{4+} doping in **Sections 4.2.1** and **4.3.1** respectively show that the stability of the structure may not only depend on the nearest neighbour Coulombic interactions but interactions between defect clusters. These interactions can be best visualised by creating an effective charge model for the given reactions showing all the interactions between the defects. However, the issue of whether the present analysis of results based on a (2x2x2) supercell are adequate needs to be resolved by further work with a (3x3x3) or (4x4x4) supercell.

In contrast, for the Mott Littleton method it has been shown in most cases that, for the various reactions for creating the oxygen vacancies and for Ce^{4+} doping studied in **Sections 4.2.2** and **4.3.2**, interactions between nearest neighbours in a defect cluster according to Coulomb's law determine stability, and therefore as the distances between individual defects in a cluster are increased the stability of the structure is decreased. This effect is due to the dilute defects clusters being isolated and therefore other interactions between defect clusters are not taken into account. An important exception to this simple view is the case of doping Ce^{4+} into non-stoichiometric $LaCoO_3$ resulting in filling of oxygen vacancies. The most favoured case is where the filled oxygen site is stabilised by the highly oxidised Ce^{4+} nearest neighbours while the reduced Co^{2+} cations are further away.

A comparison of calculations here for Ce doping with results in **Table 4.25** from simplified Mott Littleton calculations, where defects are modelled individually instead of as compensating defect clusters as in this thesis, shows good agreement but has indicated that interaction between defects in a cluster can be important in determining structural stability.

The data in **Table 4.24** confirm that the $Ce^{4+}$is not soluble in stoichiometric $LaCoO_3$ by either of the two processes involving creation of La vacancies or reduction of Co^{3+}. This has been attributed to the ionic radius mismatch for twelve-fold coordinated Ce^{4+}

(1.14Å) compared to La^{3+} (1.36Å). However, the markedly lower solution energy for a third reaction shows that, if Ce^{4+} is inserted into the reductively non-stoichiometric, oxygen deficient lattice of $LaCoO_3$, then there is much greater solubility. In this reaction, the insertion of Ce^{4+} is compensated by filling oxygen vacancies. Thus, the amount of Ce^{4+} incorporation can be considered to be dependent on the level of reductive non-stoichiometry induced under conditions for a typical high temperature preparation. Also, it has been shown that co-doping with Sr^{2+} is not a particularly favourable process.

However, the defect energies for creation of oxygen vacancies and the Ce^{4+} doping solution energies reported here relate to the bulk material, whereas catalysis is normally considered to be a largely surface process, although, in the case of perovskite oxides, sub-surface processes in relation to oxygen availability for intrafacial catalysis are also important. Therefore, in the following **Chapters 5** and **6** computational simulations have been carried out to investigate the creation of oxygen vacancies and the solubility of Ce^{4+} at the surface of $LaCoO_3$.

REFERENCES

(1) M.S.D.Read; M.S.Islam; G.Watson; F.King; F.E.Hancock. *J. Mater. Chem.* **2000**, *10*, 2298.

(2) Accelrys.Inc. DMol^3 program, 1996.

(3) M.Cherry; M.S.Islam; C.R.A.Catlow. *J. Solid State Chem* **1995**, *118*, 125.

(4) J.Shackelford; W.Alexander *"Materials Science and Engineering Handbook"*, 3rd ed.

(5) N.Mott; M.Littleton. *Trans. Faraday Soc.*, *34*, 485.

(6) S.A.French; C.R.A.Catlow; R.J.Oldman; S.C.Rogers; S.A.Axon. *Chem.Commun* **2002**, 2706.

CHAPTER 5

5. ATOMISTIC COMPUTATIONAL STUDIES OF OXYGEN VACANCY CREATION AT $LaCoO_3$ SURFACES

Defects such as oxygen vacancies play an important role in catalytic oxidation, as discussed in **Section 2.3** with the different reactions of catalytic oxidation being described in **Section 2.3.2**. Oxygen vacancies can be created by various processes, the two discussed in this thesis, are by Sr^{2+}doping at the La site in $LaCoO_3$, and by the reduction of Co^{3+} to Co^{2+}, as discussed in **Section 4.2**. The solubility and precise effect of cation dopants in perovskites has been successfully modelled for a number of systems by atomistic methods, which can predict the favoured defect compensation processes in the bulk[1,2] which has also been the main focus in this thesis. However, for catalysis it is the structure and chemistry of the surface, which are important. For perovskites, our knowledge of surface processes during catalytic oxidation processes is limited. Therefore the focus of this chapter is on catalytic oxidation where oxygen vacancies play an important part in the processes occurring at the surface.

Atomistic simulation techniques have been used here to investigate the defect surface structure for $LaCoO_3$ containing oxygen ion lattice vacancies. For these computer simulations the MARVIN code was employed for the treatment of the surface structure as discussed in **Section 3.5.3**[3], with the shell model potential described in **Sections 3.1.1** and **3.1.2**[4,5]. The interatomic potentials parameters used in the surface simulations were directly transferred from GULP calculations as in **Table 3.1** to MARVIN, as it was assumed that the charge and polarisation of the surface ions are the same as those of bulk ions. The sizes of regions I and II were chosen such that the surface energy changes by less than $0.01 J/m^2$ on expansion of either. All the structures were relaxed using the Broyden-Fletcher-Goldfarb-Shannon algorithm (BFGS) as discussed in **Section 3.3.4.**

As a first step the approach of Read *et al* was followed in reproducing the relaxed surface structures for stoichiometric $LaCoO_3$[1]. Oxygen vacancies were then introduced by the two reactions shown below:

doping Sr^{2+} into the La^{3+} site,

$$2SrO + 2La_{La}^{x} \rightarrow 2Sr_{La}^{2+} + V_{O}^{\bullet\bullet} + La_2O_3 \qquad (5.1)$$

reduction of Co^{3+} to Co^{2+},

$$2Co_{Co}^{x} + O_{O}^{x} \rightarrow 2Co_{Co}^{2+} + V_{O}^{\bullet\bullet} + 1/2\,O_2 \qquad (5.2)$$

These reactions represent the idealised processes, which might be envisaged as being of importance for suprafacial (5.1) and intrafacial (5.2) oxidation catalysis which have been discussed in detail in **Section 2.3.2**[6]. Reaction (5.1) generates oxygen vacancies by Sr doping, which is believed to enhance suprafacial catalysis by creation of favoured adsorption sites, whereas reaction (5.2) results in the loss of surface oxygen through the participation of lattice oxygen in the catalytic cycle of reaction and replenishment during intrafacial catalysis. It should be noted that reaction (5.2) is also equivalent to the spontaneous creation of oxygen vacancies in the course of a typical catalytic preparation of $LaCoO_3$ involving calcination at high temperature to produce a slightly reductively non-stoichiometric material. Such treatment may also influence the efficiency of suprafacial catalysis[7].

These simulations provide a basis for determining the energetically favoured surface structure, and therefore the crystal morphology, in the presence of oxygen ion vacancies, which will be discussed in **Section 5.3.3**.

5.1 Stoichiometric $LaCoO_3$ Surfaces

In this thesis the low index surfaces for cubic $LaCoO_3$ perovskite, which are the (100), (110) and (111) planes, have been investigated. These surfaces have dipole moments perpendicular to the surface repeat unit, which, as shown by Tasker, result in instability, which, can be removed by surface reconstruction[8]. In each case, in the process of reconstruction by removal of half the surface atoms to the bottom face of the model, it is possible to generate two possible surface terminations as discussed briefly in **Section 3.5.2**. For example, the dipole moment for the (100) plane can be removed by surface reconstruction creating OLa terminated and OCoO terminated

layers as shown in **Figure 5.1a**. Similar reconstructions were carried out for the (110) and (111) planes, which are shown in **Figure 5.1b** and **c** respectively.

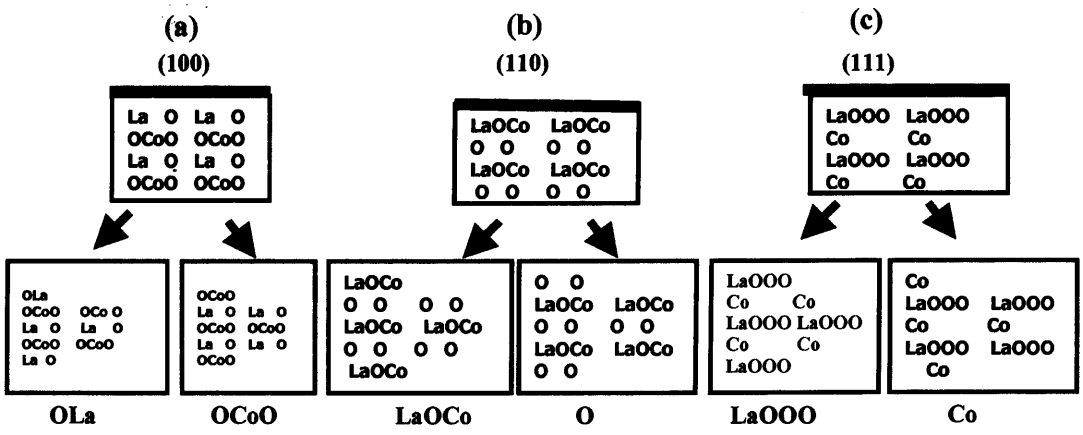

Figure 5.1 *Schematic representation of the stacking sequence for the (100), (110) and (111) $LaCoO_3$ surfaces where the surface plane is uppermost.*

Different surface unit cells were investigated to identify which would yield the most stable reconstructed surface. Detailed calculations were carried out for the (100) OLa terminated layer by comparing the (2x1), (4x1), (6x1), (8x1), (10x1) and ($\sqrt{2}$x$\sqrt{2}$) surface reconstructions where (2nx1) represents a reconstruction with n adjacent OLa units exposed at the surface followed by *n* adjacent cells in which the outermost OLa ions have been removed. The calculated surface energies in **Table 5.1** show that there is little variation in the surface energy from the 2x1 to 10x1 cells. The results also show that the model with a (2x1) cell generates a more stable structure compared to ($\sqrt{2}$x$\sqrt{2}$). These two structures are compared in **Figure 5.2** which reveals that for the (2x1) cell there is a much greater displacement possible for the oxygen in the Co-O layer directly under La than for the ($\sqrt{2}$x$\sqrt{2}$) vector. By contrast, the ($\sqrt{2}$x$\sqrt{2}$) surface cell has stable CoO_6 units and less relaxation can occur within the structure. Similar results for the convergence of surface energies were obtained for the reconstruction of the (110) and (111) surfaces. Therefore for all surface planes the (2x1) cell was employed. In order to achieve convergence with region size, the sizes I and II required

for the simulations for (100) and (110) were 6 and 12 unit cells and for the (111) plane 7 and 16 unit cells respectively.

Surface cell geometries	Surface energy (Jm^{-2})
2x1	2.16
4x1	2.33
6x1	2.50
8x1	2.51
10x1	2.54
$\sqrt{2}x\sqrt{2}$	5.84

Table 5.1. *The relaxed surface energies for the (100) OLa termination for different surface cells.*

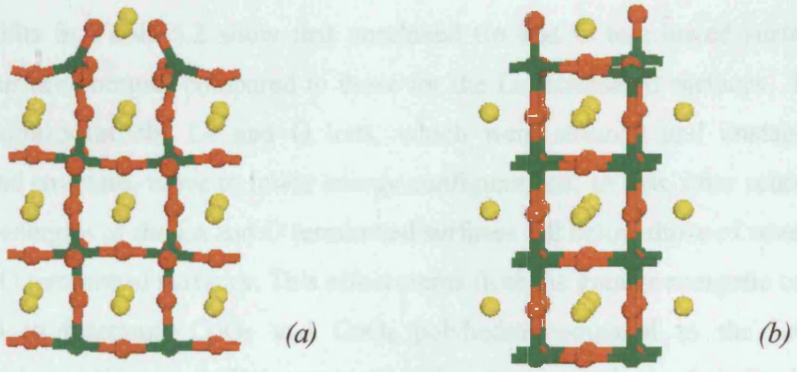

Figure 5.2. *Relaxed surface structures for (100) OLa (a) (2x1) and (b) ($\sqrt{2}x\sqrt{2}$). (Lattice sites are colour coded as La^{3+} O^{2-} Co^{3+}) where the surface plane is uppermost layer.*

Table 5.2 shows the surface energies calculated for $LaCoO_3$ from the MARVIN code as defined in equation (3.25) in **Section 3.5** for the (100), (110) and (111) planes for each of the terminations discussed by Read *et al* and illustrated in **Figure 5.3**[11]. The results obtained here reproduced this previous work.

	Unrelaxed surface energies (Jm^{-2})		Relaxed surface energies (Jm^{-2})	
Miller index	**Calculated surface energy**	**Surface energy from Read *et al*[1]**	**Calculated surface energy**	**Surface energy from Read *et al*[1]**
(100) OLa	9.01	9.04	2.16	2.18
(100) OCoO	6.59	6.62	2.69	2.68
(110) O	5.48	5.50	2.01	2.05
(110) LaOCo	10.28	10.30	3.84	3.87
(111) Co	8.25	8.27	3.69	3.72
(111) LaOOO	10.23	10.25	3.09	3.11

Table 5.2 *The surface energies calculated for $LaCoO_3$ for the planes (100), (110) and (111).*

The results in **Table 5.2** show that unrelaxed Co and O terminated surfaces have lower surface energies compared to those for the La terminated surfaces. However, during relaxation, the La and O ions, which were strained and unstable in the unrelaxed structure, move to lower energy configurations, so that, after relaxation the surface energies of the La and O terminated surfaces fall below those of several of the Co and O terminated surfaces. This effect stems from the greater energetic constraints required to rearrange CoO_5 and CoO_6 polyhedra compared to the La oxygen coordination environment. The most stable relaxed structure is the O(110) plane, with the order of stability being:

(110)-O ~ (100)-OLa>(100)-OCoO> (111)-LaOOO>(111)-Co~(110)-LaOCo,

in agreement with the work of Read *et al*[1]. The calculated structures of the most stable surface are shown in **Figure 5.3**.

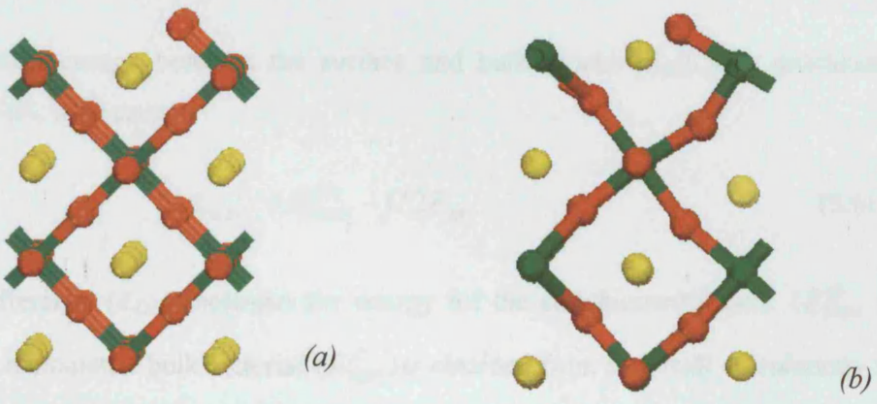

Figure 5.3. *The unrelaxed (a) and relaxed (b) structures for the stoichiometric (110)O terminated surface (Lattice sites are colour coded as* La^{3+} O^{2-} Co^{3+}*) where the surface plane is uppermost*

5.2 Calculating Surface Energies for $LaCoO_3$ Surface Structures

In **Section 5.1** surface energies have been calculated for stoichiometric $LaCoO_3$ in order to assess the relative stabilities of different surfaces and terminations. In the following section, surface energies will be calculated for non-stoichiometric, oxygen vacancy containing $LaCoO_3$. In both cases, the stability of the surface structure is determined by the surface energy. The surface energy (γ) can be calculated from the difference between the energy of the surface block (E_{SURF}) and the energy for the same number of bulk ions (E_{BULK}) per unit area as discussed in **Section 3.5** and shown in equation (5.3). However when calculating the surface energy for the non-stoichiometric surface a correction term is added from which the surface energy of the non-stoichiometric surface can be calculated.

Firstly, the bulk energy (E_{BULK}) for the stoichiometric material is calculated from the following equation:

$$\gamma = \frac{(E_{SURF} - E_{BULK})}{A} x16.02189 \qquad (5.3)$$

using the values for the surface energy(γ), the energy of the surface block (E_{SURF}) and the area (A) derived from MARVIN. The figure of 16.02189 is a conversion factor from eV to J/m^2. To derive the energy of the surface block it is necessary to correct the total surface block energy (E_{SURF}^{TOT}) from MARVIN for the boundary

interaction energy between the surface and bulk blocks (E_{BI}), also calculated by MARVIN, such that:

$$E_{SURF} = E_{SURF}^{TOT} - 1/2E_{BI} \tag{5.4}$$

The difference (E_{DEF}) between the energy for the stoichiometric bulk (E_{BULK}^{SS}) and non-stoichiometric bulk material (E_{DEF}^{SS}) is obtained from supercell calculations on the bulk system containing the same number of defect as to the surface block, in this case 2x2x2, in GULP such that:

$$E_{DEF} = E_{BULK}^{SS} - E_{DEF}^{SS} \tag{5.5}$$

Finally, the surface energy of the non-stoichiometric material is calculated from the equation:

$$\gamma = \frac{(E_{SURF}^{DEF} - (E_{BULK} + E_{DEF})}{A} x16.02189 \tag{5.6}$$

where the energy of the surface block for non-stoichiometric material (E_{SURF}^{DEF}) is derived from MARVIN after correcting for the boundary interaction as in equation (5.4) and (E_{BULK}) has been calculated previously from equations (5.3) for stoichiometric material.

The above procedure is used throughout this thesis to calculate surface energies for non-stoichiometric systems.

5.3 Non-stoichiometric $LaCoO_3$ Surface Structures

We investigate the effect of oxygen vacancies created in $LaCoO_3$ according to the two reactions involving doping Sr^{2+} at the La^{3+} site (5.1) and reduction of Co^{3+} to Co^{2+}(5.2). It should be noted that Coulombic interactions between defects with opposite effective charges are expected to stabilise defect clusters involving the Sr^{2+} dopants and oxygen vacancies in the case of reaction (5.1) and reduced Co^{2+} ions and

oxygen vacancies in the case of reaction (5.2). This assumption has been confirmed by the results shown in **Table 5.3** where, broadly, the most stable models are shown to be where the defects are closest within the compensating cluster. The detailed results are presented in the following sections.

5.3.1 Creation of Oxygen Vacancies via Sr^{2+} Doping

Figure 5.4 illustrates the layer structure of the surface region for the various surface planes and terminations studied in this thesis, where the notation is such that the depth co-ordinate, z = 1, in **Table 5.3** is the surface layer. The layer spacings for the (100), (110) and (111) surfaces are 1.91Å, 1.35Å and 1.11Å respectively. **Table 5.3** gives the configuration of the defects examined, defined in terms of the layer at which the dopant and vacancy are substituted, the distances between the defects (i.e. Sr^{2+} dopants and O^{2-} vacancies). Therefore calculations have been carried out by doping Sr^{2+} at the La^{3+} site in $LaCoO_3$, (i.e. reaction (5.1) above), for the (100), (110) and (111) surfaces. Electroneutrality requires two Sr^{2+} ions for each oxygen vacancy, which are labelled in **Table 5.3** as $Sr_1^{2+}$and Sr_2^{2+}. For reference, a schematic diagram illustrating the disposition of defects identified in **Table 5.3** for the (100) surface with OLa termination is shown in **Figure 5.5**.

Table 5.3 also shows the defect energies for creation of oxygen vacancies according to reaction (5.1) for different dispositions of compensating defects within the surface layers. These energies have been calculated exactly as for the bulk studies reported in **Section 4.2.1** in equation (4.3) but using the lattice energy calculated by MARVIN for the surface block containing the defects. The results for the different surfaces are as follows:

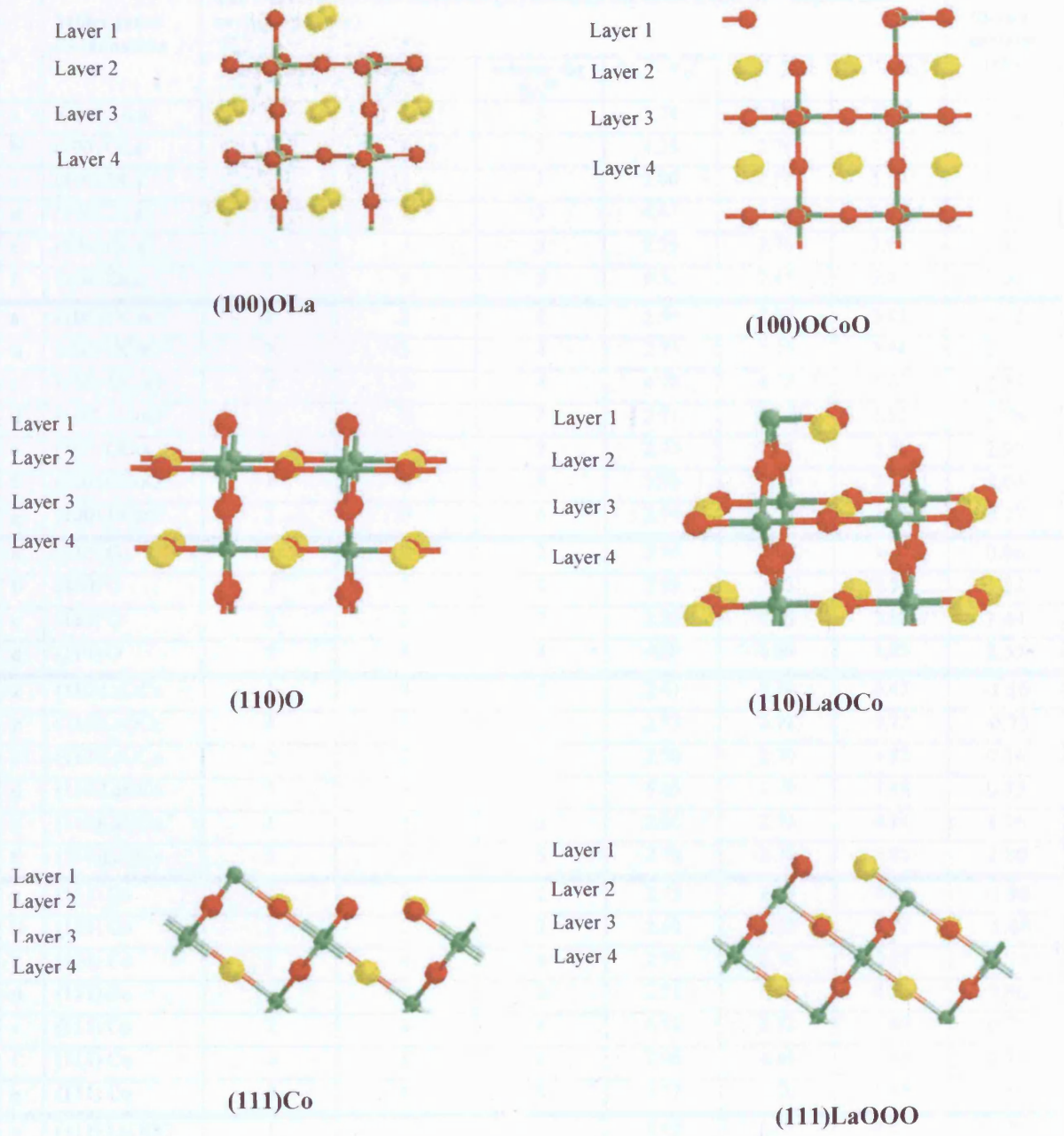

Figure 5. 4. *Different z-layers for the stoichiometric unrelaxed (100), (110) and (111) reconstructured surfaces (Lattice sites are colour coded as* La^{3+} O^{2-} Co^{3+}*)*

	Miller index /termination	The z-layers and the distances (Å) between the defects (i.e. Sr^{2+} dopant and oxygen vacancy)						Defect energies (eV)
		z-layer for V_O^{2-}	z-layer for Sr_1^{2+}	z-layer for Sr_2^{2+}	Sr_1^{2+}- V_O^{2-}	Sr_2^{2+}- V_O^{2-}	Sr_1^{2+}- Sr_2^{2+}	
a	(100) OLa	2	1	3	2.74	2.79	4.00	1.67
b	(100) OLa	1	1	3	4.33	2.70	3.76	1.90
c	(100) OLa	3	3	3	2.80	2.71	3.99	2.32
d	(100) OLa	3	1	3	4.67	2.70	3.79	2.52
e	(100) OLa	4	3	5	2.75	2.76	3.98	3.12
f	(100) OLa	1	5	5	9.32	7.45	3.82	7.00
a	(100) OCoO	2	2	2	2.59	2.82	3.83	1.72
b	(100) OCoO	3	2	4	2.73	2.75	3.94	2.24
c	(100) OCoO	2	4	4	4.78	4.78	3.82	2.57
d	(100) OCoO	1	2	2	2.71	4.74	3.95	2.98
e	(100) OCoO	2	2	2	2.75	2.75	3.95	2.98
f	(100) OCoO	4	4	4	5.93	2.72	3.67	3.04
g	(100) OCoO	5	4	6	2.74	2.77	3.99	3.27
a	(110) O	1	2	2	2.70	2.70	3.82	0.96
b	(110) O	3	2	2	2.93	2.93	3.51	1.23
c	(110) O	2	2	2	2.83	4.89	3.88	1.44
d	(110) O	3	4	4	4.69	4.69	3.85	2.55
a	(110)LaOCo	2	3	3	2.61	5.78	3.47	-1.16
b	(110)LaOCo	4	5	5	2.73	2.71	3.77	-0.73
c	(110)LaOCo	2	3	3	2.70	2.70	3.82	0.24
d	(110)LaOCo	3	3	3	4.45	2.70	3.48	0.75
e	(110)LaOCo	1	1	3	2.96	2.73	4.10	1.76
f	(110)LaOCo	5	5	5	2.70	2.79	5.40	2.80
a	(111) Co	2	2	2	2.75	4.45	4.64	-1.98
b	(111) Co	2	2	2	2.69	2.52	5.22	-1.48
c	(111) Co	4	4	4	2.79	2.76	5.55	-0.11
d	(111) Co	2	2	2	2.71	6.42	4.52	0.56
e	(111) Co	2	4	4	6.18	2.72	5.60	0.79
f	(111) Co	6	6	6	7.96	4.68	5.33	1.13
g	(111) Co	8	8	8	2.77	2.76	5.53	3.51
a	(111) LaOOO	1	1	3	4.42	2.63	4.05	-1.86
b	(111) LaOOO	1	1	3	4.45	7.15	4.40	-1.80
c	(111) LaOOO	1	3	3	2.73	6.11	5.49	-1.44
d	(111) LaOOO	3	3	3	4.82	9.65	5.25	1.37
e	(111) LaOOO	5	5	5	2.70	4.64	5.34	3.33

Table 5.3. *The z-layers, distances between the defects (Sr^{2+} dopant and O^{2-} vacancies and Sr_1^{2+} - Sr_2^{2+}) and calculated defect energies for $LaCoO_3$ (100), (110) and (111) planes for the Sr doping reaction (5.1). (Note: The z-layers for V_O^{2-}* and *Sr^{2+} are from the unrelaxed initial structures*)

(100) $LaCoO_3$ Surface

The results in **Table 5.3** show that for the Sr doped OLa terminated (100) surface, the defect energy of 1.67eV (configuration **(a)**) is only slightly lower than that of 1.72eV for the OCoO (configuration **(a)**) terminated surface. These values compare with 3.05eV and 2.95eV derived in this thesis from bulk supercell and Mott Littleton calculations as reported in **Tables 4.2** and **4.5** respectively. The results here for both terminations thus clearly show that it is energetically more favourable for defects to segregate to the surface as there is a general trend for the (100) surface that the deeper the defect complex, the higher the defect energy and the closer it approximates the bulk value. The more favourable substitution at the surface compared to the bulk by Sr^{2+} has also been observed in calculations by Read *et al*[1] although those calculations reported less detail than presented here since specific sites were not identified.

A schematic diagram illustrating the disposition of defects identified in **Table 5.3** for the (100) surface with OLa termination is shown in **Figure 5.5**. It is clear that for defect clusters closest to the surface, a number of detailed factors control which particular vacancy site is most favoured. For example, for the most stable model (**Figure 5.5a**, with a defect energy of 1.67eV) we see that the oxygen vacancy has the lowest energy when located between the doped Sr cations, where the defects are closest to each other, compared to the second most stable configuration (**Figure 5.5b**, with defect energy 1.90eV), where the vacancy has also migrated to the surface but the defect-defect separation is larger overall.

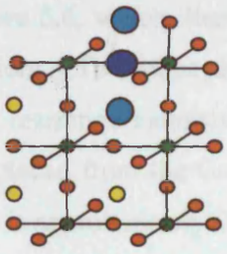

(a)

Energy =1.67eV

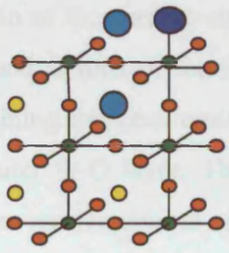

(b)

Energy =1.90eV

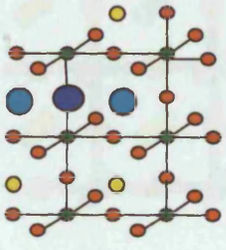

(c)

Energy =2.32eV

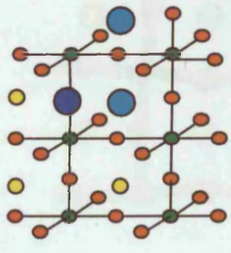

(d)

Energy =2.52eV

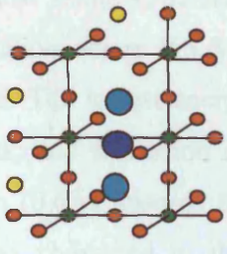

(e)

Energy = 3.12eV

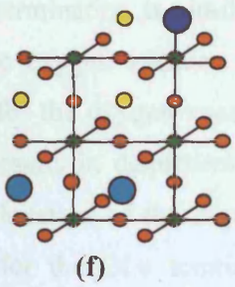

(f)

Energy =7.00eV

Figure 5.5. *Idealised structures for configuration listed in* ***Table 5.3****, for the non-stoichiometric (100)OLa terminated $LaCoO_3$ surface structures (a),(b),(c),(d),(e) and(f) containing O^{2-} vacancies and Sr^{2+} dopants. (Lattice sites are colour coded as La^{3+} O^{2-} Co^{3+} Sr^{2+} O^{2-} vacancy)*

The unrelaxed and relaxed structures for the most stable model, configuration **(a)** in **Table 5.3,** (defect energy of 1.67eV) for the (100)OLa terminated surface are shown in **Figure 5.6**, which illustrates the relaxation of the surface and the displacement of the Sr ions. To reduce the strain, the Co and O ions of the CoO_5 polyhedra at the surface rearrange extensively and the remaining oxygens underneath the surface Sr are displaced from the Co-O layer to the outer Sr-O layer. The displacement of the oxygen is approximately 0.50Å, which causes rearrangement of the ions to a depth of three layers down, as shown in **Figure 5.6**.

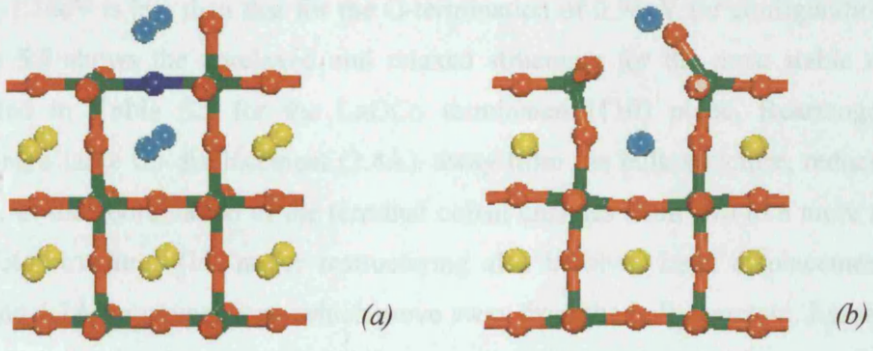

Figure 5.6. *The unrelaxed (a) and relaxed (b) structures for the OLa terminated layer for the non-stoichiometric (100) $LaCoO_3$ surface containing O^{2-} vacancies/ Sr^{2+} dopants. (Lattice sites are colour coded as La^{3+} O^{2-} Co^{3+} Sr^{2+} O^{2-} vacancy)*

The most stable structure for the OCoO termination is similar to that for the OLa termination where the Sr dopants and the oxygen vacancy segregate towards the surface. The lowest energy configuration for the oxygen vacancy is between the Sr dopants, and relaxation of the structure results in displacement of the sub-surface oxygen (0.6Å) towards the dopants. The location of the dopants in the subsurface layer as compared to the surface layer for the OLa terminated configuration is probably the cause of the slight increase in the defect energy.

Finally we should note that the result for configuration **(f)** in **Table 5.3** and **Figure 5.5**, where the defects are separated, shows a substantial increase in the defect energy for creating an oxygen vacancy (7.00eV) indicating that the defect complexes are indeed bound with the Coulomb term being a major component of the binding energy.

(110) $LaCoO_3$ Surface

A clear pattern emerged for the (100) surface as discussed above: the lowest energies result when the compensating defects, O^{2-} vacancies and Sr^{2+} cations, are located next to one another close to the exposed surface. However, the case of the (110) surface is different, as it is a more complex surface.

For the (110)LaOCo terminated surface, the energies for configuration **(a)** in **Table 5.3** of -1.16eV is less than that for the O-termination of 0.96eV for configuration **(a)**. **Figure 5.7** shows the unrelaxed and relaxed structures for the most stable model identified in **Table 5.3** for the LaOCo terminated (110) plane. Rearrangement involving a large Co displacement (2.4Å), away from the bulk structure, reduces the energy, as the coordination of the terminal cobalt changes from two to a more stable three-fold structure. This major restructuring also involves large displacements of 2.7Å and 4.7Å for oxygen ions, which move away from the bulk structure. Essentially the half termination for this surface is inconsistent with the coordination chemistry of cobalt, which drives the extensive reconstruction.

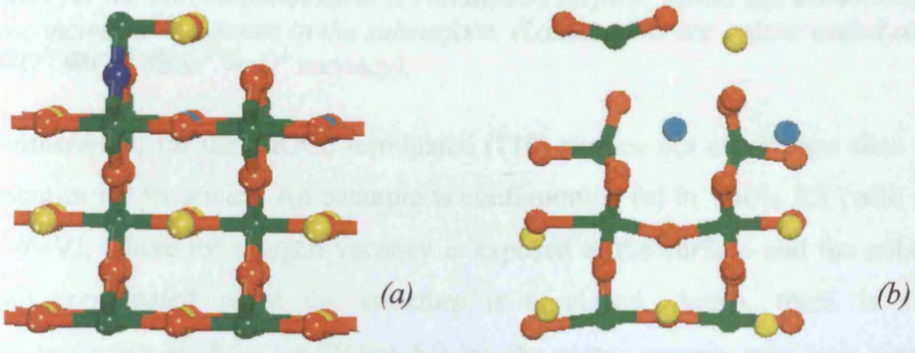

Figure 5.7. *The unrelaxed (a) and relaxed (b) structures for the LaOCo terminated layer for the non-stoichiometric (110)$LaCoO_3$ surface containing O^{2-} vacancies/ Sr^{2+} dopants (Lattice sites are colour coded as La^{3+} O^{2-} Co^{3+} Sr^{2} O^{2-}vacancy).*

For the LaOCo terminated (110) plane, our calculations show that vacancies created deeper within the subsurface structure can also have low energies, for example, at a depth of 4Å, the calculated energy is -0.73eV for configuration **(b)** in **Table 5.3**. Once again the low defect energy is due to the rearrangement of the surface cobalt, this time from three fold coordinated surface cobalt to the more favoured four fold coordinated cobalt. This rearrangement involves displacement of the exposed cobalt

by 2.7Å towards the bulk oxygens, which are bonded to the three coordinated subsurface cobalt (due to the oxygen vacancy). It is accompanied by large displacements of the outermost oxygens with La displaced away from the bulk. Overall this relaxation is best described as a concerted rearrangement of the ions. **Figure 5.8** illustrates the comparison between the unrelaxed and relaxed structures for this model. Overall, these large relaxation effects reflect the instability of the stoichiometric LaOCo terminated (110) surface in contrast to the stoichiometric (110)O terminated surface.

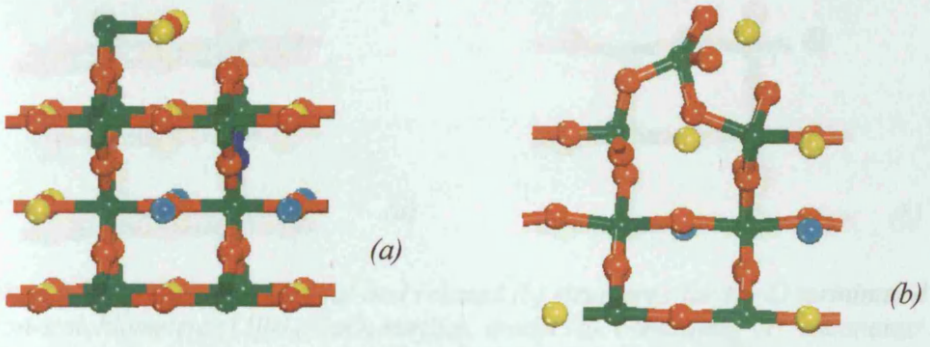

Figure 5.8. *The unrelaxed (a) and relaxed (b) structures for the LaOCo terminated layer for the non-stoichiometric (110)$LaCoO_3$ surface, model* ***(b)****, containing O^{2-} vacancies/ Sr^{2+} dopants in the subsurface. (Lattice sites are colour coded as La^{3+} O^{2-} Co^{3+} Sr^{2+} O^{2-} vacancy).*

Furthermore, for the LaOCo terminated (110) surface not all surface sites yield low energies for vacancies. An example is configuration **(e)** in **Table 5.3** (with energy of 1.76eV), where the oxygen vacancy is exposed at the surface and the cobalt is two fold coordinated when the structure is unrelaxed. Again, there is substantial reconstruction as shown in **Figure 5.9**, but the energy remains relatively high.

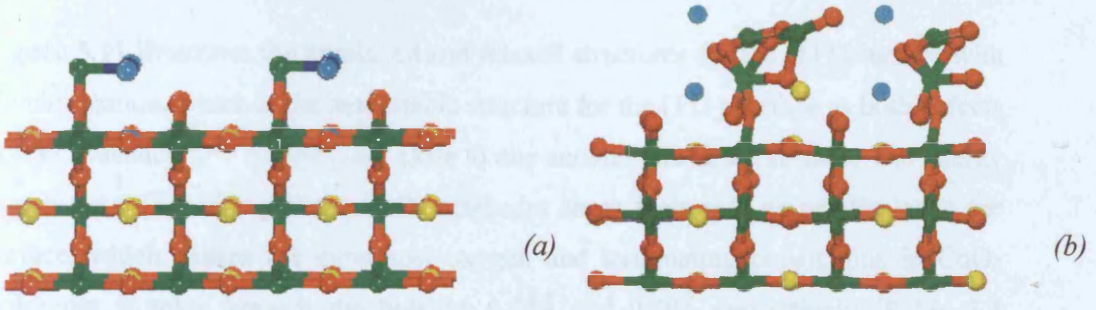

Figure 5.9. *The unrelaxed (a) and relaxed (b) structures for the LaOCo terminated layer for the non-stoichiometric (110)$LaCoO_3$ surface, model* ***(e)****, containing O^{2-} vacancies/ Sr^{2+} dopants. (N.B In order to visualise the relaxation better, the 4x1 unit structure has been shown. Lattice sites are colour coded as La^{3+} O^{2-} Co^{3+} Sr^{2+} O^{2-} vacancy).*

Turning to the O terminated (110) plane, the results in **Table 5.3** show that this surface behaves in a more straightforward manner than the LaOCo termination. In the most energetically favoured structure for the oxygen terminated surface for configuration **(a)**, the oxygen vacancy is segregated at the surface and the Sr dopants are in the adjacent sub-layer as illustrated in **Figure 5.10**. The relaxed structure in **Figure 5.10(b)** shows a slight movement of the Sr dopants (0.14Å). The presence of the oxygen vacancy at the surface causes displacements of the Co ions (0.24Å) and rearrangement of the oxygens in the sublayers (0.36Å and 0.23Å).

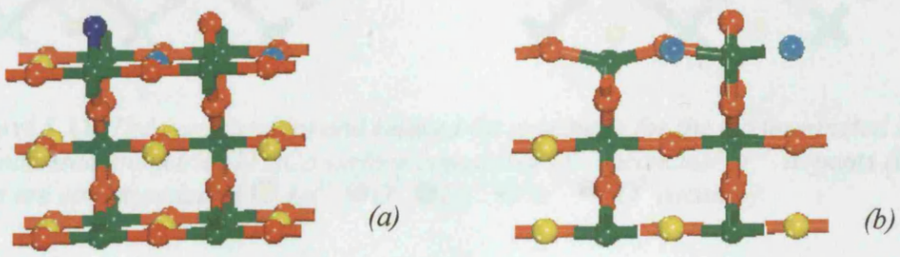

Figure 5.10. *The unrelaxed (a) and relaxed (b) structures for the O terminated layer for the non-stoichiometric (110)$LaCoO_3$ surface, model (a), containing O^{2-} vacancies/ Sr^{2+} dopants. (Lattice sites are colour coded as La^{3+} O^{2-} Co^{3+} Sr^{2+} O^{2-}vacancy).*

(111) $LaCoO_3$ Surface

As for the (100) surface, the results for the (111) surfaces in **Table 5.3** show stable defect clusters and that surface segregation is favourable. Comparison of the two terminations in **Table 5.3** reveals that the most stable vacancy/dopant configuration, **(a)**, for the Co terminated surface (-1.98eV) is only slightly more favourable than for the LaOOO termination configuration, **(a)** (-1.86eV), in the presence of Sr^{2+} dopants.

Figure 5.11 illustrates the unrelaxed and relaxed structures for the (111) surface with Co termination, which is the most stable structure for the (111) surface as both defects (i.e. O^{2-} vacancy/Sr^{2+} dopants) are close to one another and at the surface. The energy is reduced by the tilting of the CoO_6 octehedra about their axes perpendicular to the surface, which causes the outermost oxygen and terminating cobalt ions in CoO_5 polyhedra to relax towards the bulk by 0.24Å and 0.79Å respectively. **Table 5.3** shows that it is energetically more favoured to create oxygen vacancies via Sr^{2+} doping for the (111) surface, both Co and LaOOO terminated, compared to (100) and

(110). Indeed, the defect energies calculated reveal an unusually low defect energy for the (111) surface compared to the (110) and (100) surfaces: the introduction of dopants and vacancies allows the initially constrained and unstable structure to rearrange to form a more favoured conformation.

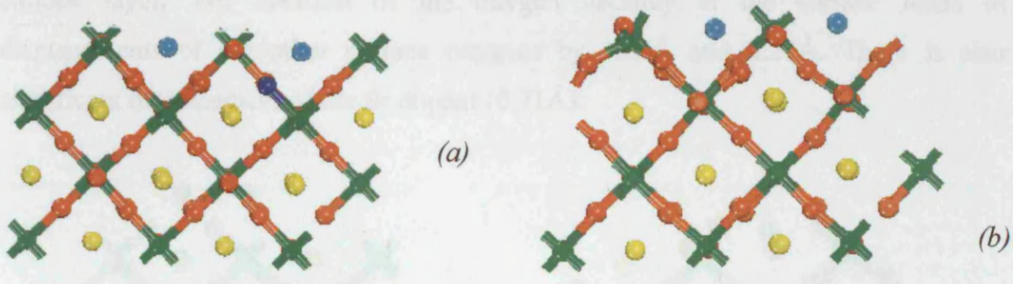

Figure 5.11. *The unrelaxed (a) and relaxed (b) structures for the Co terminated layer for the non-stoichiometric (111)Co surface containing O^{2-} vacancies/ Sr^{2+} dopants (Lattice sites are colour coded as La^{3+} O^{2-} Co^{3+} Sr^{2+} O^{2-} vacancy).*

As for the (110) surface, the results in **Table 5.3** reveal a marked anomaly for the Co terminated (111) surface. For example, one of the configurations with an oxygen vacancy created at the exposed surface has a relatively high energy of 0.56eV (configuration **(d)**) compared to the others. The unrelaxed structure has a two fold coordinated terminal cobalt, and in the relaxed structure there is a major reconstruction, as seen in **Figure 5.12,** involving large displacements of both Co and Sr to yield 4 fold coordinated cobalt; but the energy remains high. The asymmetric co-ordination of Co when it is terminating leads to the large defect energy and the energetic preference for the vacancy to be in the sub-surface layer.

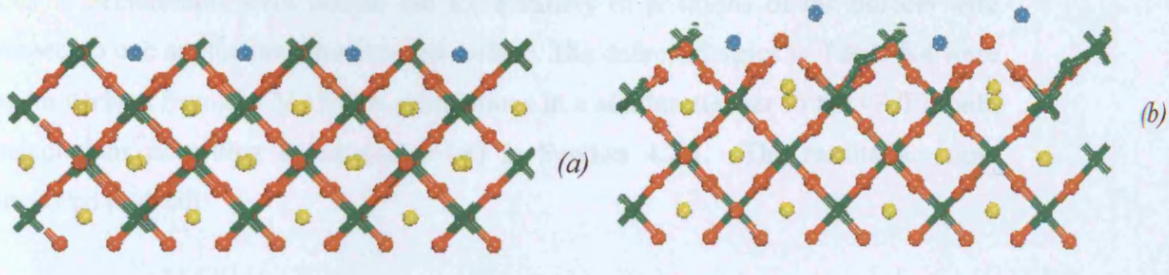

Figure 5.12. *The unrelaxed (a) and relaxed (b) structures for the Co terminated layer for the non-stoichiometric (111)$LaCoO_3$ surface containing O^{2-} vacancies/ Sr^{2+} dopants (N.B In order to visualise the relaxation better the 4x1 unit structure have been shown. Lattice sites are colour coded as La^{3+} O^{2-} Co^{3+} Sr^{2+} O^{2-} vacancy).*

The results in **Table 5.3** indicate straightforward behaviour on doping Sr^{2+} into the LaOOO terminated (111) surface (configuration **(a)**). **Figure 5.13** illustrates the most stable structure for the LaOOO termination, which shows one of the Sr dopants and the oxygen vacancy in the surface layer and the other Sr dopant in the adjacent sub surface layer. The creation of the oxygen vacancy at the surface leads to displacements of the other surface oxygens by 0.23Å and 0.28Å. There is also significant displacement of the Sr dopant (0.71Å).

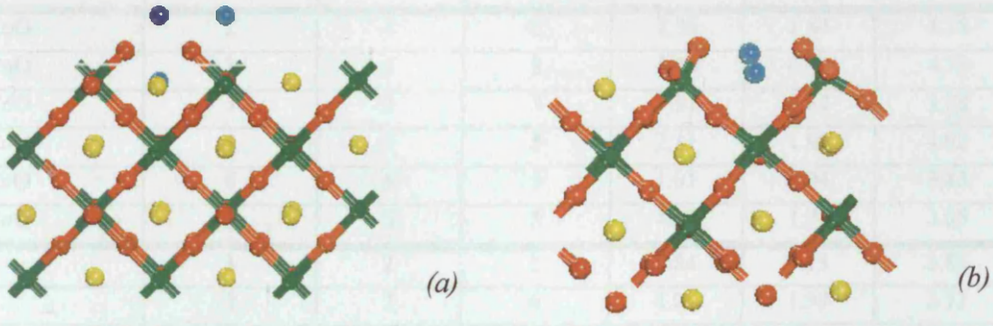

Figure 5.13. *The unrelaxed (a) and relaxed (b) structures for the LaOOO terminated layer for the non-stoichiometric (111) $LaCoO_3$ surface containing O^{2-} vacancies/ Sr^{2+} dopants(Lattice sites are colour coded as La^{3+} O^{2-} Co^{3+} Sr^{2+} O^{2-} vacancy).*

5.3.2 Creation of Oxygen Vacancies via Reduction of Co^{3+}

As in **Table 5.3**, **Table 5.4** reports the defect configurations (i.e. Co^{2+} and O^{2-} vacancies), and defect energies for creation of oxygen vacancies as a result of reducing the Co oxidation state from Co^{3+} to Co^{2+} as in reaction (5.2), in which two Co^{2+}compensate for one oxygen vacancy. The former are tabulated as Co_1^{2+} and Co_2^{2+}. Simulations were carried out for a variety of positions of the defects with respect to one another and the exposed surface. The defect energies in **Table 5.4** were again derived from the MARVIN calculations in a similar manner to the GULP bulk calculations according to equation (4.4) in **Section 4.2.1**. The results are now reviewed in detail:

	Miller index/ termination	The z-layers (Å) and distances between the defects (i.e. Co^{2+} dopant and oxygen vacancy)						Defect energies (eV)
		z-layer for V_O^{2-}	z-layer for Co_1^{2+}	z-layer for Co_2^{2+}	Co_1^{2+}- V_O^{2-}	Co_2^{2+}- V_O^{2-}	Co_1^{2+}-Co_2^{2+}	
a	(100) OLa	2	2	2	2.36	1.91	4.27	0.73
b	(100) OLa	1	2	2	1.82	4.33	4.02	0.86
c	(100) OLa	3	2	4	2.53	1.91	4.44	1.35
d	(100) OLa	1	2	4	1.13	5.66	4.56	1.80
e	(100) OLa	4	4	4	1.86	1.88	3.73	2.11
f	(100) OLa	2	4	4	4.25	4.17	3.89	4.20
a	(100) OCoO	2	1	3	2.36	1.84	4.18	-0.10
b	(100) OCoO	1	1	3	5.75	6.87	4.72	0.83
c	(100) OCoO	3	3	3	1.91	1.87	3.78	1.81
d	(100) OCoO	4	3	5	2.11	1.90	4.02	2.30
e	(100) OCoO	5	5	5	1.91	1.94	3.85	2.44
f	(100) OCoO	5	5	5	4.27	1.91	3.85	4.64
a	(110)O	1	2	2	1.84	4.13	3.83	0.37
b	(110)O	3	2	4	4.08	1.99	3.73	0.96
c	(110)O	2	2	2	1.97	5.67	3.69	1.71
d	(110)O	6	6	6	1.88	1.88	3.77	2.72
a	(110) LaOCo	2	3	3	4.28	3.99	6.63	-0.48
b	(110) LaOCo	2	1	3	1.94	1.92	3.77	-0.12
c	(110) LaOCo	1	1	3	2.45	4.18	3.73	1.00
d	(110) LaOCo	4	3	3	4.15	4.32	6.45	1.16
e	(110) LaOCo	3	3	3	2.03	1.88	3.90	1.73
f	(110) LaOCo	5	5	5	1.89	1.92	3.81	2.48
a	(111) Co	2	1	3	1.89	4.11	3.86	-3.51
b	(111) Co	2	1	3	4.30	7.17	3.99	-3.09
c	(111) Co	2	1	3	1.91	4.16	3.67	-2.98
d	(111) Co	4	3	3	4.37	1.95	5.59	-2.01
e	(111) Co	2	3	3	1.93	5.69	5.25	-1.23
f	(111) Co	6	5	5	4.29	4.32	5.28	-0.50
g	(111) Co	8	7	7	2.03	5.77	5.37	2.40
a	(111) LaOOO	1	2	2	4.35	4.24	5.53	-1.14
b	(111) LaOOO	3	2	4	1.79	5.86	6.77	-0.07
c	(111) LaOOO	1	2	2	2.02	4.35	5.60	1.45
d	(111) LaOOO	7	6	6	4.26	4.32	5.34	1.58
e	(111) LaOOO	9	8	8	1.93	5.73	5.42	3.22

Table 5.4 *The z-layers, distances between the defects (i.e. dopants Co_1^{2+}, Co_2^{2+} and O^{2-} vacancies), and defect energies calculated for $LaCoO_3$ for the planes (100), (110) and (111) for the cobalt reduction reaction (5.2). (N.B. The z-layers for V_O^{2-} and Co^{2+} are from the unrelaxed structures).*

(100) $LaCoO_3$ Surface

Figure 5.14 presents schematic diagrams for the different defect configurations reported in **Table 5.4** for the (100) surface with OCoO termination. For the (100) surface containing Co^{2+} and O^{2-} vacancies, the most favoured termination for the defect creation is the OCoO terminated surface in **Figure 5.14a**, which gives a defect energy of -0.10eV (configuration **(a)**), which is calculated to be lower than that for the OLa termination 0.73eV (configuration **(a)**). These values compare with those of 3.38eV and 2.59eV derived in this thesis from bulk supercell and Mott Littleton calculations as reported in **Tables 4.3** and **4.6** respectively. This comparison indicates that oxygen vacancies compensated by reduction of $Co^{3+}$are preferentially formed nearer to the surface compared to the bulk, which is supported by the overall trend in the results in **Table 5.4** as a function of defect disposition.

As with the Sr doping reaction, the oxygen vacancy has a lower energy when it is between the pair of Co^{2+}ions. For the most stable structure, the defects are closer together compared to the case where the oxygen vacancy is segregated to the surface in the next most stable model, configuration **(b)**.

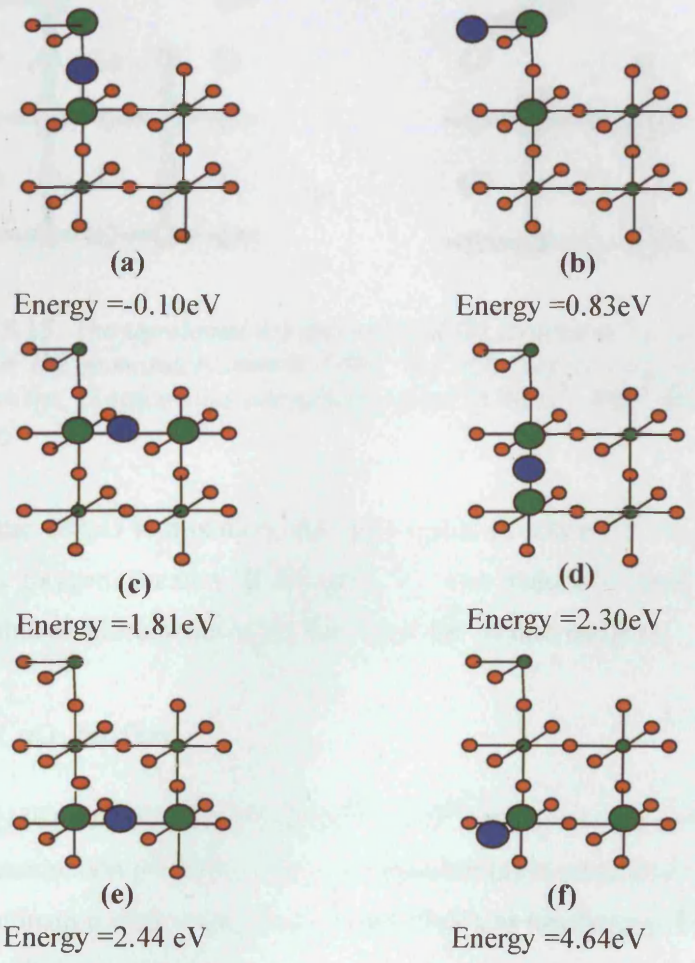

Figure 5.14. *Idealised structures listed in* ***Table 5.4*** *for (100) OCoO terminated $LaCoO_3$ surface structures (a),(b),(c),(d),(e) and (f) containing O^{2-} vacancies and Co^{2+} cations (N.B. For simplicity the La ions are not shown and lattice sites are colour coded as O^{2-} Co^{3+} Co^{2+} O^{2-}vacancy)*

The unrelaxed and relaxed structures for the most stable configuration **(a)** from **Table 5.4** (-0.10eV) are shown in **Figure 5.15**. The results show the displacement of the surface CoO_3 layer, which rearranges extensively.

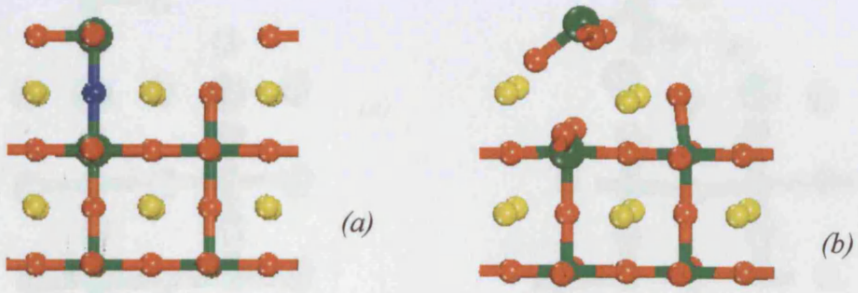

Figure 5.15. *The unrelaxed (a) and relaxed (b) structures for the OCoO terminated layer for the non-stoichiometric (100) $LaCoO_3$ surface containing O^{2-} vacancies/ Co^{2+} cations. (Lattice sites are colour coded as La^{3+} O^{2-} Co^{3+} Co^{2+} O^{2-} vacancy)*

As with the OCoO termination, the most stable structure for the OLa termination is when the oxygen vacancy is between the two reduced cobalt ions. This causes considerable displacements of the latter and the surface oxygens.

(110) $LaCoO_3$ Surface

For the (110) surface containing $Co^{2+}$and O^{2-} vacancies, the defect energy for the LaOCo termination (-0.48eV) with configuration **(a)** is calculated to be lower than for the O termination with configuration **(a)**(0.37eV), as tabulated in **Table 5.4**. However, as for the Sr doping reaction, there are some unusual results for the (110) LaOCo termination, which are discussed below.

Figure 5.16 illustrates the structure for the (110) surface with the LaOCo termination giving the lowest energy (-0.48eV), configuration **(a)** in **Table 5.4**. As found in previously discussed configurations, major reconstruction results in a change in the coordination of the cobalt from two to four.

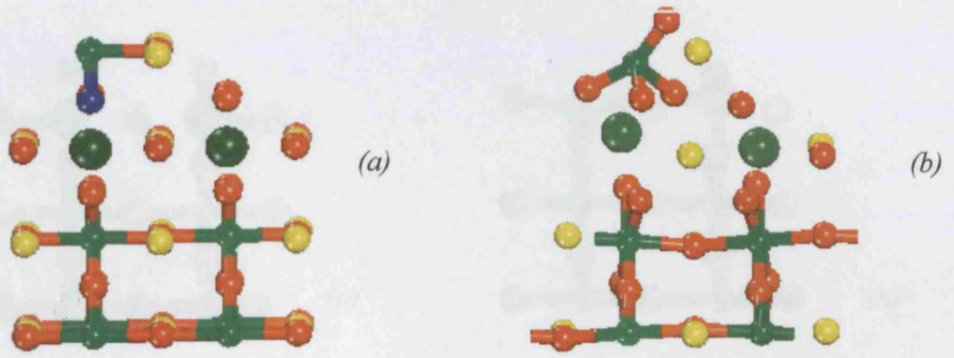

Figure 5.16 *The unrelaxed (a) and relaxed (b) structures for the LaOCo terminated layer for the non-stoichiometric (110)$LaCoO_3$ surface, model* ***(a)****, containing O^{2-} vacancies/ Co^{2+} cations. (Lattice sites are colour coded as La^{3+} O^{2-} Co^{3+} Co^{2+} O^{2-} vacancy)*

The results in **Table 5.4** for the (110)LaOCo termination also show that the oxygen vacancy has a lower defect energy when located between the two Co^{2+} ions as shown in the configuration **(b)** (defect energy of -0.12eV), compared to the configuration **(c)** (with defect energy of 1.00eV), where the oxygen vacancy is at the surface. The difference can be attributed to the greater flexibility of the former configuration, which allows greater relaxation.

Moreover, as the defects comprising $Co^{2+}$and O^{2-} vacancies are moved within the structure, it appears that, if the oxygen vacancy is located below the Co^{2+} defect pair, the structure is more favoured compared to when it is between the two Co^{2+}, which is attributable to the different modes of relaxation. When the oxygen vacancy is below Co^{2+}, two cobalt ions can share a bridging oxygen, while when oxygen vacancy is in the same layer one cobalt ion is left under-coordinated.

Figure 5.17 shows the most stable structure for the O terminated (110) surface where the oxygen vacancy is at the surface and the reduced cobalt ions are in the adjacent sub-layer, configuration **(a)** in **Table 5.4**. The relaxed structure in **Figure 5.17(b)** does not show much rearrangement as the oxygen vacancy is at the surface. The reduced cobalt ions are displaced by about 0.25Å and the oxygen ions at the surface are displaced by 0.36Å and 0.28Å. The higher defect energy for the O terminated surface compared to the LaOCo terminated surface is due to it being highly constrained and unable to relax to a lower energy structure.

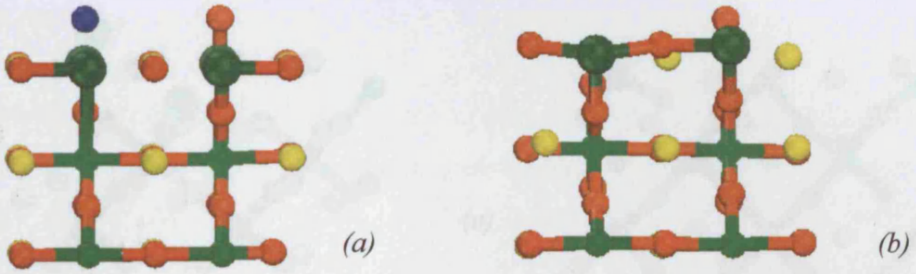

Figure 5.17 *The unrelaxed (a) and relaxed (b) structures for the O terminated layer for the non-stoichiometric (110)$LaCoO_3$ surface, model* ***(a)****, containing O^{2-} vacancies/ Co^{2+} cations. (Lattice sites are colour coded as La^{3+} O^{2-} Co^{3+} Co^{2+} O^{2-}vacancy)*

(111) $LaCoO_3$ Surface

The results in **Table 5.4** indicate that the defect energy for the Co terminated (111) surface of -3.51eV for configuration **(a)** is lower than for the LaOOO termination configuration **(a)**, (-1.14eV) in the presence of O^{2-} vacancies/Co^{2+} defects. The ease of oxygen vacancy formation for the (111) surface compared to (100) and (110) mirrors the results for oxygen vacancy creation via Sr^{2+} doping in **Table 5.3**. Comparison of both terminated surfaces in **Table 5.4** shows that oxygen vacancy formation is favoured in the Co terminated surface.

The most stable structure in **Table 5.4** for the (111) surface with Co termination (configuration **(a)**) is illustrated in **Figure 5.18**. The defect energy is reduced owing to the tilt of the CoO_6 octahedra about their axes perpendicular to the surface, which causes the terminating Co to relax towards the bulk (0.21Å), which in turn leads to the outermost La and O ions relaxing towards the bulk. The greatest displacement of oxygen is 0.30Å. Of particular interest is the prediction from **Table 5.4** that defects comprising oxygen vacancies and cobalt ions again have lower energies on the (111) surface compared with the (100) or (110) surfaces.

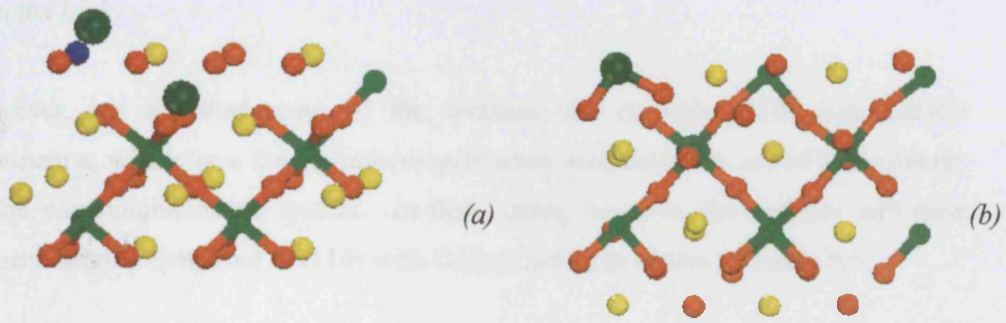

Figure 5.18. *The unrelaxed (a) and relaxed (b) structures for the Co terminated layer for the non-stoichiometric (111)$LaCoO_3$ surface containing O^{2-} vacancies/ Co^{2+} cations. (Lattice sites are colour coded as La^{3+} O^{2-} Co^{3} Co^{2+} O^{2-}vacancy)*

Figure 5.19 illustrates the most stable structure for the LaOOO terminated surface showing the oxygen vacancy at the surface and the reduced Co ions in the adjacent sub-layer in configuration **(a)** in **Table 5.4**. The surface oxygen ions move away from the bulk by about 0.31Å and 0.46Å; there is a slight displacement of the La ions (0.33Å).

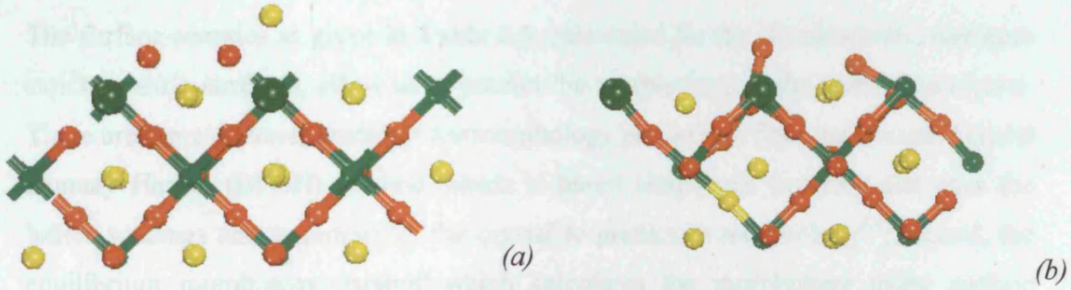

Figure 5.19. *The unrelaxed (a) and relaxed (b) structures for the LaOOO terminated layer for the non-stoichiometric (111)$LaCoO_3$ surface containing O^{2-} vacancies/ Co^{2+} cations (Lattice sites are colour coded as La^{3+} O^{2-} Co^{3+} Co^{2+} O^{2-}vacancy)*

5.4 Morphology of $LaCoO_3$

The calculated surface energies in **Table 5.5** for $LaCoO_3$ containing oxygen vacancies show that in all cases the surface energies are lower than those for the stoichiometric material in **Table 5.2**. The results are in line with the earlier findings discussed in

Section 5.3 that vacancies have lower formation energies at the surface compared with the bulk.

However, we see that some of the surfaces, for example (110) with LaOCo termination, which have the highest energies when stoichiometric, are of lower energy in the non-stoichiometric system. In these cases, however, the surfaces still have higher energies compared to (110) with O termination as shown in **Table 5.5.**

Miller index	Calculated stoichiometric surface energies (Jm^{-2})	Calculated surface energy for the Sr doped reaction (5.1) (Jm^{-2})	Calculated surface energy for the reduced Co reaction (5.2) (Jm^{-2})
(100) OLa	2.16	1.65	1.50
(100) OCoO	2.69	2.02	0.79
(110) O	2.01	1.16	0.88
(110) LaOCo	3.84	2.20	1.96
(111) Co	3.69	2.09	1.51
(111) LaOOO	3.11	1.53	1.65

Table 5.5. *Calculated surface energies for the stoichiometric, Sr doped reaction and the reduced Co reaction for the creation of O^{2-} vacancies.*

The surface energies as given in **Table 5.5**, calculated for the stoichiometric and non-stoichiometric surfaces, allow us to predict the morphology of the perovskite crystal. There are three different methods for morphology prediction: first, the Bravais Friedel Donnay Harker (BFDH) method which is based simply on structure and uses the lattice spacings and symmetry of the crystal to predict its morphology[9]; second, the equilibrium morphology method which calculates the morphology using surface energies[10]; and the third, the growth morphology method where the attachment energy is calculated, which is defined as the energy per molecule released when a new layer of ions is attached to the crystal face[3]. The greater the value for the attachment energy, the lower the contribution of that surface to the crystal morphology. In the present case the equilibrated morphology approach was found to reproduce the experimental results most closely for example, the scanning electron microscopy studies of the related polycrystalline material[11]. The resulting calculated morphology for stoichiometric $LaCoO_3$ is similar to the predictions of Read *et al*, with contributions from both the (110) and (100) surfaces, as discussed in **Section 5.1** and shown in **Figure 5.20.**

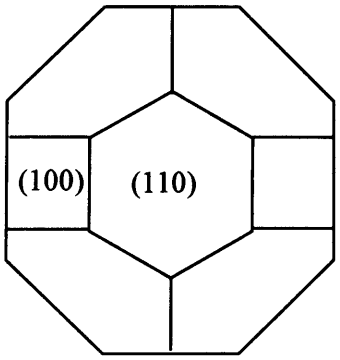

Figure 5. 20 *The predicted equilibrated crystal morphology for the stoichiometric $LaCoO_3$.*

In our calculated surface energies, we may predict the equilibrium morphology of the non-stoichiometric crystal bulk. The resulting simulations predict that, for Sr doped $LaCoO_3$, the crystal morphology is dominated by (110) faces as shown in **Figure 5.21a** unlike the stoichiometric material where both (110) and (100) faces are displayed. For materials containing oxygen vacancies compensated by reduction of Co^{3+} to Co^{2+}, (110) and (100) faces are equally prevalent as in **Figure 5.21b** but, unlike the stoichiometric material, the OCoO termination is favoured compared to OLa in the case of the (100) surface. It is interesting to note that despite the introduction of defects into the surfaces, the (110)O surface remains highly stable compared to the others and (110)LaOCo remains the least stable in all cases. In the case of Sr doping, the only surface which changes its stability in relation to the others in the undoped material is (111)LaOOO. In the case of the Co reduction reaction the behaviour is obviously more complex.

To understand the conceptual issues in reconciling the data concerning surface energy in **Table 5.2** and **5.5** and defect energies in **Table 5.3** and **5.4** it is important to differentiate clearly between surface and defect energy. The surface energy is the overall energy required to create a surface, whereas the defect energy is the energy required to create a defect in the original defect free surface. In this work, these defect energies are referenced to the relaxed stoichiometric surface. Thus the

morphologies in **Figure 5.21**, predicted for non-stoichiometric $LaCoO_3$ containing O^{2-} vacancies and derived from the surface energies in **Table 5.5**, relate to a material, which would be prepared by a single step process, for example a typical high temperature (>900°C) calcination. Even for formulations not containing Sr prepared by high temperature calcination, reductively non-stoichiometric $LaCoO_3$ is predicted to contain O^{2-} vacancies and Co^{2+}as discussed by French *et al*[12]. According to the results presented here, these vacancies would be segregated to the surface.

These predictions do not correspond to the measurements for specially prepared single crystals of undoped and Sr doped $LaCoO_3$, which indicate the dominance of the (111) surface[13]. The discrepancy is not likely to be due to the choice of modelling method since the potentials used predict the $LaCoO_3$ unit cell parameters to be within 1% of the experimental value. However, these single crystal materials prepared via a melt process are unlikely to be representative of polycrystalline materials prepared by solution phase precipitation routes and calcinations at more modest temperatures (900°C). The predictions are also not in agreement with experimental observations for a related material, undoped $SmCoO_3$, where Low Energy Ion Scattering (LEIS) has indicated surface enrichment of the A site Sm cation, i.e. a preference for (100)OSm and (111)SmOOO surface planes[14]. Here the author tentatively suggests the (100) surface on the basis of surface density but concede some discrepancy exists. However, the nature of the preparation should again be noted, in this case involving a dense, polycrystalline pellet which was sintered at 1250°C followed by grinding and diamond spray polishing. Substantial destruction of the surface crystal structure and surface segregation might be expected.

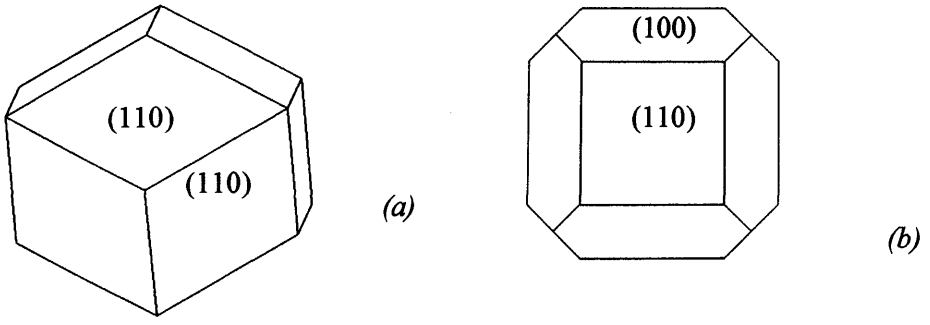

Figure 5.21. *The equilibrium crystal morphologies based on relaxed structures for non-stoichiometric $LaCoO_3$ (a) Sr^{2+} doping reaction (5.1), (b) Co^{3+} reduction reaction (5.2).*

5.5 Implications for Catalysis

Turning now to the catalytic properties of the different surfaces, we should consider firstly those faces which are likely to be present in the material as prepared and differentiate between these faces in terms of the defect energies for creating the catalytically important oxygen vacancies. The stoichiometric material is predicted to display (100)OLa terminated and (110)O terminated surfaces, both of which might be of importance for suprafacial activity. However, for intrafacial catalysis, where creation of oxygen vacancies and mobility of oxygen anions becomes important at higher temperature, the (110)O terminated surface is likely to be the most significant since the defect energy to create vacancies is lower **(Table 5.2)**, as illustrated in **Figure 5.22a**.

In the case of non-stoichiometric Sr doped materials, the situation is simplified since only the (110)O terminated surface is predicted as shown in **Figure 5.22b** and oxygen vacancies are relatively easily created in this surface **(Table 5.3)**. However the cycle of filling and recreation of vacancies is likely to involve cobalt redox behaviour although the initial vacancies created by Sr^{2+} doping are likely to dominate.

For undoped, reductively non-stoichiometric $LaCoO_3$ both (100)OCoO terminated and (110)O terminated faces are predicted to be present in as prepared material and both should be of importance for suprafacial processes. In the case of intrafacial activity, where the cycle of filling and recreation of oxygen vacancies becomes dominant, the (100)OCoO terminated surface is likely to be most significant as shown in **Figure 5.22c** since the defect energy for vacancy formation is lower **(Table 5.4)**. The appearance of the (100)OCoO terminated face in undoped, non-stoichiometric $LaCoO_3$ compared to the (100)OLa terminated in stoichiomtric material indicates potentially different surface chemistry behaviour in catalysis.

Considering all cases, stoichiometric and non-stoichiometric materials, suprafacial and intrafacial activity, two surfaces are predicted to play a key role: (110)O terminated and (100)OCoO terminated. In both these cases, the target O site for creation of oxygen vacancies is well exposed at the surface. The catalytic behaviour

will be influenced by the preparative methods used, for example calcination, which affects both the development of crystallinity and oxygen non-stoichiometry[15].

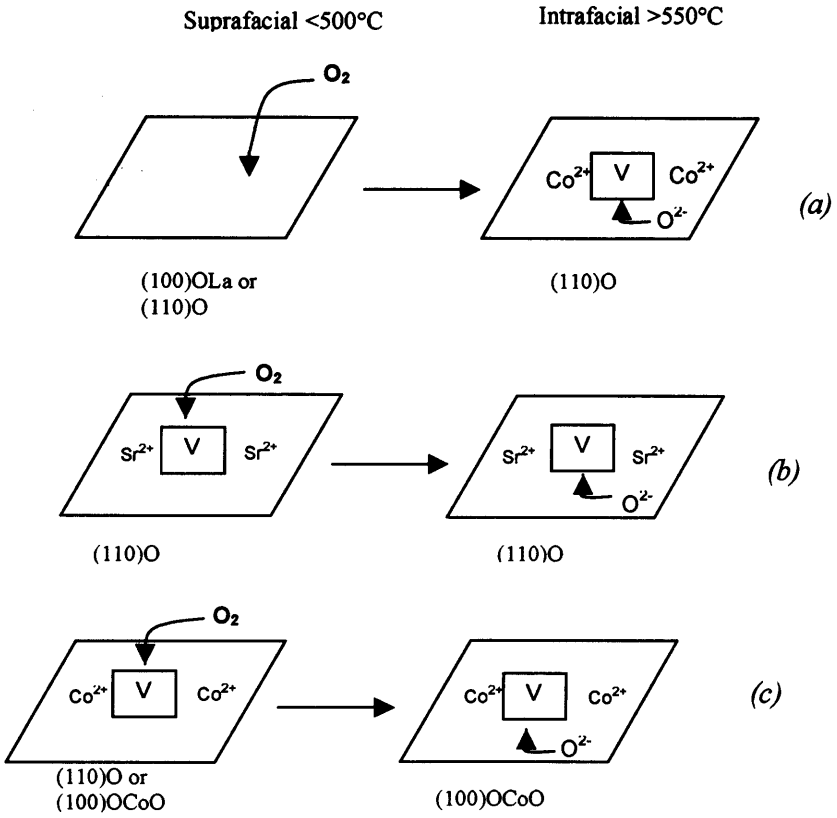

Figure 5.22 *Implications for catalysis on stoichiometric surfaces (a) non-stoichiometric surfaces (b)Sr^{2+} doped or (c)containing Co^{2+}*

5.6 Summary and Conclusions

The atomistic calculations of the surface structure of the catalytically active perovskite $LaCoO_3$ are aimed at underpinning the development of a better mechanistic description of the processes involved during catalytic oxidation and, in particular, the nature of the active oxygen states concerned with the hypothesised, suprafacial and intrafacial reactions. The calculations in this chapter have reproduced all the low index surface terminations investigated by Read *et al*, i.e. (100), (110) and (111), for stoichiometric $LaCoO_3$. Experimental evidence from electron microscopy suggests

that these low index faces do indeed dominate the crystal morphology of $LaCoO_3$, although higher index faces may be present under the high operating temperature of some catalyst processes and play an active role in catalysis[11].

Defects especially oxygen vacancies are known to play a fundamental role in surface morphology, adsorption and catalysis. The calculations on Sr doped and reduced cobalt materials find higher stability when there is a close separation between defects of opposite charge as would be expected on simple electrostatic grounds. Moreover, the results show that in many cases, there is a strong driving force for surface segregation of oxygen vacancies. However, the factors controlling surface stability are complex, as noted in many cases, e.g. the (110)LaOCo surface, where the coordination chemistry of cobalt drives extensive surface reconstruction.

For materials containing oxygen vacancies, the results clearly confirm that the presence of defects strongly influences crystal morphology and surface chemistry. For reaction (5.1) involving creation of oxygen vacancies coupled with Sr doping it appears that the relaxed (110)O terminated surface alone becomes energetically favoured compared to (100)OLa and (110)O as predicted for stoichiometric $LaCoO_3$. The order of stability from the surface energies for the different surfaces containing oxygen vacancies created by doping of Sr^{2+} at the La^{3+} site is given by:

(110)O>(111)LaOOO~(100)OLa>(100)OCoO ~(111)Co~(110)LaOCo.

For reaction (5.2), involving creation of oxygen vacancies by reduction of Co^{3+} to Co^{2+}, the calculations show that the (100)OCoO terminated and (110)O terminated planes have the lowest surface energies. In this case, the order of stability for all the low index faces is shown to be:

(100)OCoO~(110)O>(100)OLa~(111)Co~(111)LaOOO > (110)LaOCo.

These predictions of morphology do not correspond with measurements by X-ray scattering and LEIS. However, in both cases the materials for experimental examination were prepared under conditions where surface segregation or surface structure disruption might be expected.

The significance of the results for catalytic behaviour is evident when we consider which crystal faces are likely to occur in the as prepared material and the consequent implications for suprafacial activity. These crystal surfaces can then be distinguished regarding their intrafacial activity in terms of the ease of creating oxygen vacancies. For stoichiometric materials, where both (100)OLa terminated and (110)O terminated surfaces are predicted to be prevalent, under high temperature conditions, the latter is likely to dominate intrafacial catalysis as a result of the ease of creating vacancies **(Table 5.5)**. For non-stoichiometric, Sr^{2+} doped $LaCoO_3$ the situation is simpler since the (110)O terminated surface is predicted to dominate the crystal morphology and, as indicted above, the energy for creating oxygen vacancies is relatively low. For as prepared, undoped reductively non-stoichiometric $LaCoO_3$, which is predicted to display (110)O terminated and (100)OCoO terminated surfaces, the latter is most likely to dominate intrafacial activity since creation of vacancies is energetically highly favoured. We should note that catalytic behaviour is likely to depend on preparative conditions, which influence both crystallinity and oxygen non-stoichiometry. Furthermore, the results highlight the possibility of controlling morphology through selective creation of surface defects by doping.

For the two surfaces identified as being particularly important for catalysis as prepared materials containing oxygen vacancies generated via Sr^{2+} doping or reduction of $Co^{3+}$to $Co^{2+}$the target oxygen site is well exposed. This feature should be the subject of further work involving a more detailed quantum mechanical study to investigate the interaction of molecular oxygen with the stoichiometric and the oxygen vacancy containing non-stoichiometric surfaces.

REFERENCES

(1) M.S.D.Read; M.S.Islam; G.Watson; F.King; F.E.Hancock. *J. Mater. Chem* **2000**, *10*, 2298.

(2) Y.Wu; B.Dou; C.Wang; X.Xie; Z.Yu; S.Fa; Z.Fan; L.Wang. *J.Catal.* **1989**, *88*, 120.

(3) D.H.Gay; A.L.Rohl. *J. Chem. Soc, Faraday Trans.* **1995**, *91*, 925.

(4) T.L.Hill. *J.Chem.Phys.* **1948**, *16*, 399.

(5) B.G.Dick; A.W.Overhauser. *Phys.Rev.* **1958**, *112*, 90.

(6) R.J.H.Voorhoeve; J.P.Demeika; L.E.Triumble. *N.Y Ann, Acad.Sci.* **1976**, *272*, 3.

(7) H.Aria; T.Yamada; K.Guahi; T.Seiyama. *Appl Catal.* **1986**, *26*, 265.

(8) P.W.Tasker. *J. Phys C: Solid state Phys.* **1979**, *12*, 4977.

(9) J.D.H.Donnay; D.Harker. *Am Miner* **1937**, *22*, 446.

(10) W.C.Mackrodt; R.J.Davey; S.N.Black; R.Docherty. *J. Cryst. Growth* **1987**, *80*, 441.

(11) E.Traversa; P.Nunziante; M.Sakamoto; Y.Sadaoka; M.C.Carrotta; G.Martinelli. *J. Mater. Res.* **1998**, *13*, 1335.

(12) S.A.French; C.R.A.Catlow; R.J.Oldman; S.C.Rogers; S.A.Axon. *Chem.Commun.* **2002**, 2706.

(13) W.R.Flavell; A.G.Thomas; J.Hollingworth; S.Warren; S.C.Gna; P.M.Dunwoody; C.E.J.Mitchell; P.G.D.Marr; D.Techan; S.Downes; E.H.Seddon; V.R.Dhanak; K.Asai; K.Koboyashi; N.Yamada. *Faraday Disc,* **1999**, *114*, 407.

(14) I.C.Fullarton; J.P.Jacobs; H.E.vanBenthem; J.A.Kilner; H.H.Brongersma; P.J.Scanlon; B.C.H.Steele. *Ionics* **1995**, *1*, 51.

(15) L.Haung; M.Bassir; S.Kaliguine. *Mater. Chem. and Physics* **2007**, *101(2-3)*, 259.

CHAPTER 6

6. CERIUM SOLUBILITY IN $LaCoO_3$ SURFACES

In **Chapter 2** we highlighted the importance of cation doping in lanthanum based, first row transition metal perovskites in relation to enhancement of catalytic oxidation applications, in particular the use of $LaCoO_3$ for catalytic combustion of methane and oxidation of ammonia[1,2]. Both divalent cations (Sr^{2+}/Ca^{2+}) and tetravalent (Ce^{4+}) have been shown experimentally to be effective. The effect of Sr^{2+} doping at $LaCoO_3$ surfaces on the creation of oxygen vacancies and control of morphology has been discussed in **Chapter 5**. In **Chapter 4** computational modelling studies of Ce^{4+} doping into bulk $LaCoO_3$ were reported and have confirmed experimental results and earlier, Mott Littleton calculations, that Ce^{4+} is not soluble in stoichiometric material. In contrast, it has been shown that limited solubility, up to 5%, can be achieved in non-stoichiometric, oxygen vacancy containing $LaCoO_3$ resulting in filling of those oxygen vacancies, hence providing additional oxygen for suprafacial catalysis[3]. However, catalysis is a surface process and the fact that apparently low levels of Ce^{4+} with respect to the bulk can have a marked effect on catalysis indicates that Ce^{4+} could be segregated at the surface. Therefore, in this Chapter we present surface computational studies of Ce^{4+} doping of $LaCoO_3$.

As in **Section 4.3**, four reactions were considered for cerium doping at the surface, the first two of which initially assume a stoichiometric host $LaCoO_3$ lattice, where the substitution of Ce^{4+} for La^{3+} is compensated either by creation of La^{3+} vacancies (6.1) or reduction of Co^{3+} to Co^{2+} (6.2) as shown:

$$3CeO_2 + 4La_{La}^{x} \rightarrow 3Ce_{La}^{\bullet} + V_{La}^{'''} + 2La_2O_3 \qquad (6.1)$$

$$4CeO_2 + 4La_{La}^{x} + 4Co_{Co}^{x} \rightarrow 4Ce_{La}^{\bullet} + 4e_{Co}^{'} + 2La_2O_3 + O_2 \qquad (6.2)$$

A third case is also considered where cerium is doped into the $LaCoO_3$ lattice containing oxygen vacancies, resulting in filling of those vacancies according to the equation:

$$2La_{La}^{x} + 2CeO_2 + V_O^{\bullet\bullet} \rightarrow 2Ce_{La}^{\bullet} + La_2O_3 + O_O^{x} \quad (6.3)$$

Finally calculations were carried out on co-doping Sr^{2+} and Ce^{4+} at the La site in $LaCoO_3$, as shown by the following reaction:

$$CeO_2 + SrO + 2La_{La}^{x} \rightarrow Ce_{La}^{\bullet} + Sr_{La}^{'} + La_2O_3 \quad (6.4)$$

6.1 Surface Structure of $LaCoO_3$

In **Sections 5.1** and **5.3.2** the surface structures of stoichiometric $LaCoO_3$ and non-stoichiometric material, containing oxygen anion vacancies compensated by reduction of two Co^{3+} ions to Co^{2+}, have been modelled using the MARVIN code[4]. The surface energies for the three relaxed, low index faces, (100), (110) and (111), for both stoichiomteric and non-stoichiometric $LaCoO_3$ are reproduced in **Table 6.1**.

Miller index	Calculated relaxed surface energies (Jm^{-2})	
	Stoichiometric surface	Non-stoichiometric surface
(100) OLa	2.16	1.50
(100) OCoO	2.69	0.79
(110) O	2.01	0.88
(110) LaOCo	3.84	1.96
(111) Co	3.69	1.51
(111) LaOOO	3.09	1.65

Table 6.1 *The surface energies calculated for stoichiometric and non-stoichiometric $LaCoO_3$ (100), (110) and (111) planes, also shown in* **Table 5.5**.

These results show that, for the stoichiometric material, the most stable surfaces are the (110)O and the (100)OLa terminated surfaces. For the non-stoichiometric system, the (100)OCoO terminated and the (110)O terminated surfaces are the most stable. These three surfaces, (100)OLa, (100)OCoO and (110)O, have been selected here for further computational studies to calculate the surface solution energy of Ce substituted at the La site according to the four reactions (6.1) to (6.4) described above. For reference, the unrelaxed and relaxed structures for the three selected surfaces for

stoichiometric and non-stoichiomteric $LaCoO_3$ are shown in **Figures 6.1** and **6.2** respectively.

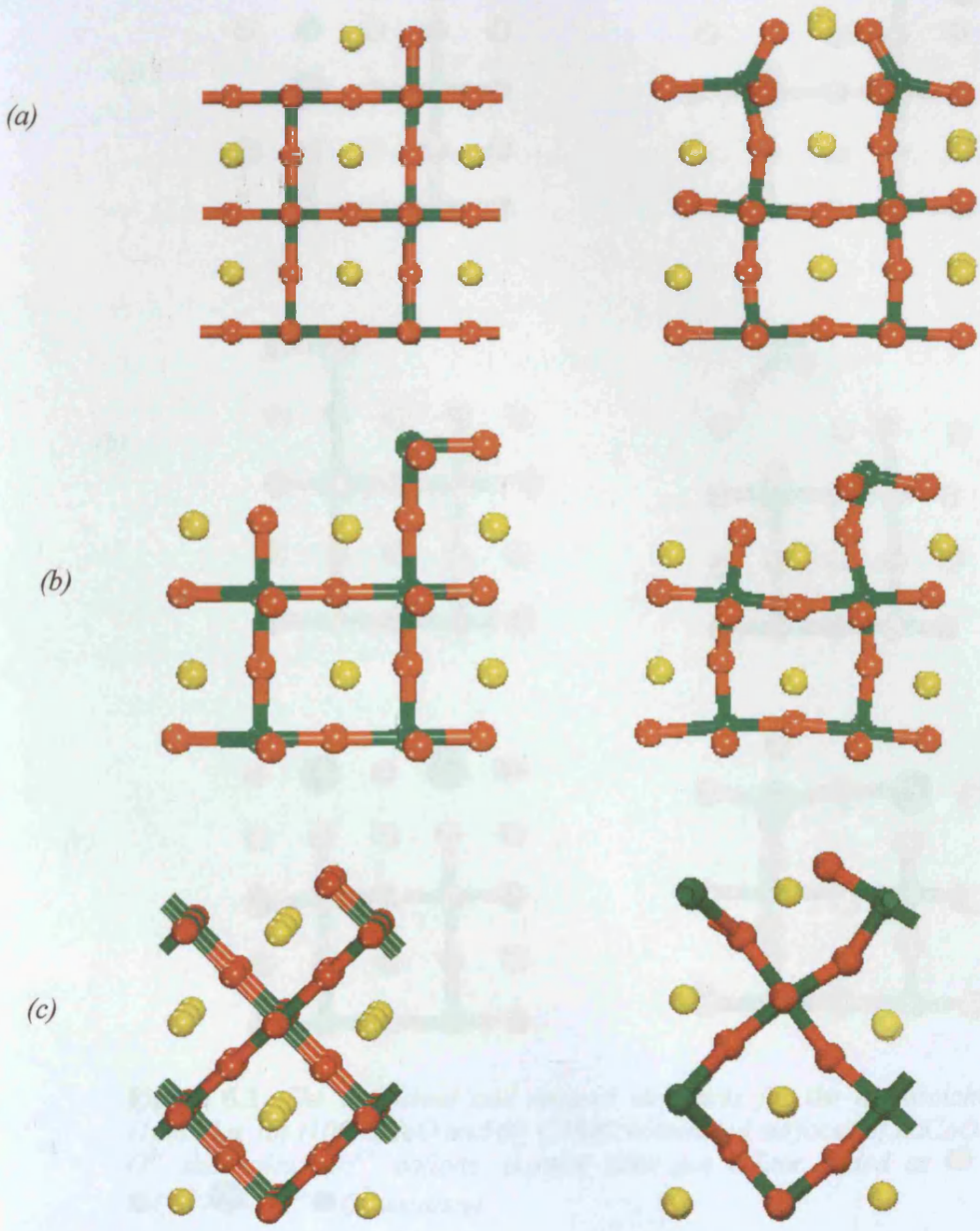

Figure 6.1. *The unrelaxed and relaxed structures for the stoichiometric (a) (100)OLa, (b) (100)OCoO and (c) (110)O terminated surfaces (Lattice sites are colour coded as* La^{3+} O^{2-} Co^{3+}*)are also shown in* **Figure 5.4**.

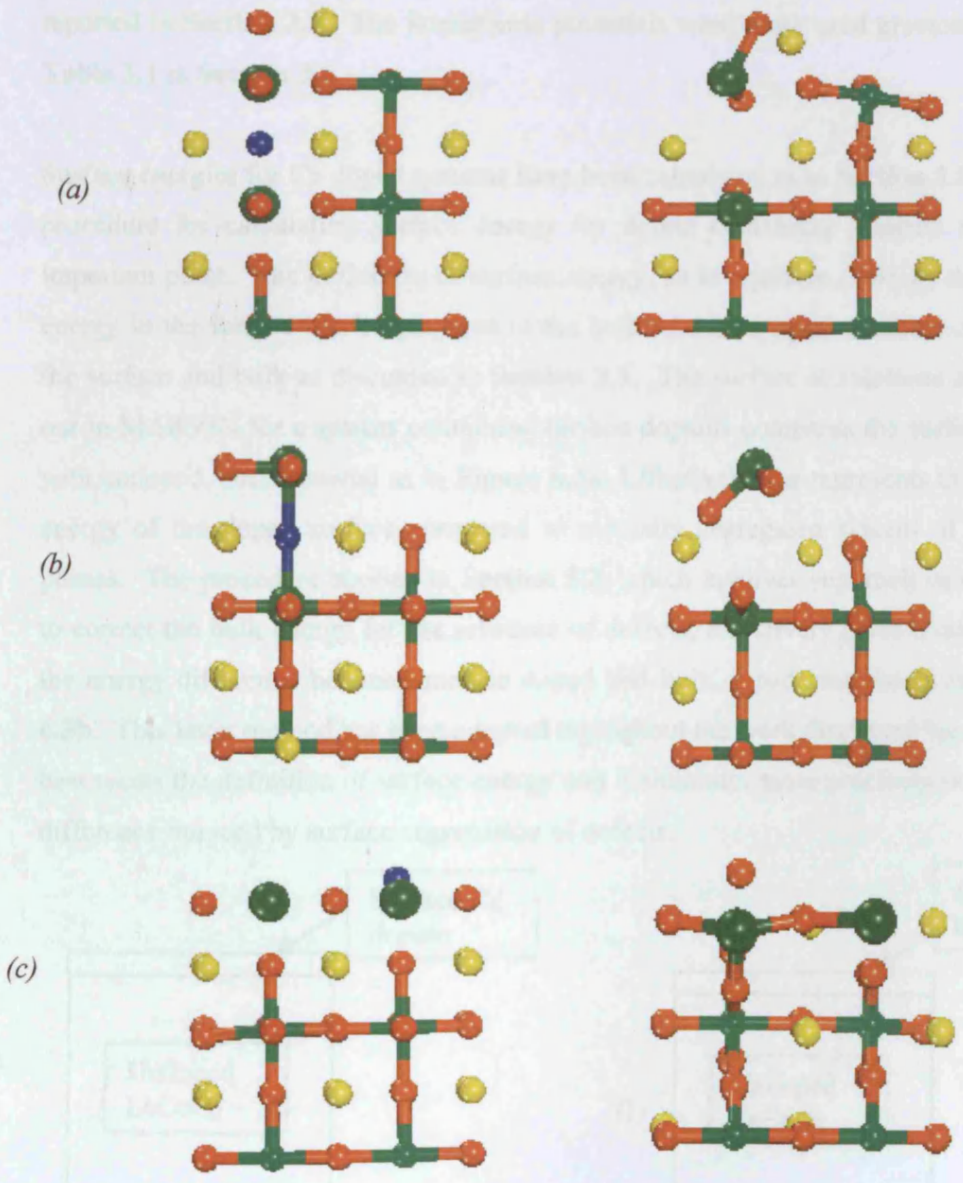

Figure 6.2. *The unrelaxed and relaxed structures for the non-stoichiometric (a) (100)OLa, (b) (100)OCoO and (c) (110)O terminated surfaces of $LaCoO_3$ containing O^{2-} vacancies/ Co^{2+} cations. (Lattice sites are colour coded as La^{3+} O^{2-} Co^{3+} Co^{2+} O^{2-}vacancy)*

The surface simulations for the Ce doped material were carried out using the MARVIN code as discussed in **Section 3.5.3**. The surfaces were reconstructed to quench the dipole perpendicular to the surface plane, as described in **Section 3.5.2** and **Section 5.1**, before energy minimization is performed using a (2x1) vector. In order to achieve insensitivity to region size, the sizes for regions I and II required for

simulation of the (100) and (110) surfaces were 6 and 12 unit cells respectively as reported in **Section 3.5**. The interatomic potentials were those used previously from **Table 3.1** in **Section 3.6**.

Surface energies for Ce doped systems have been calculated as in **Section 5.2**[5]. This procedure for calculating surface energy for defect containing systems raises an important point. The definition of surface energy, as in equation (5.3), as the excess energy in the surface block compared to the bulk relates to equal numbers of ions in the surface and bulk as discussed in **Section 3.5**. The surface simulations as carried out in MARVIN for a system containing surface dopants compares the surface block with undoped, bulk material as in **Figure 6.3a**. Effectively this represents the surface energy of the doped surface compared to a totally segregated system of separate phases. The procedure applied in **Section 5.2**, which involves supercell calculations to correct the bulk energy for the presence of defects, effectively gives a measure of the energy difference between surface doped and bulk doped material as in **Figure 6.3b**. This latter method has been adopted throughout the work discussed here since it best meets the definition of surface energy and it simulates more precisely the energy difference induced by surface segregation of defects.

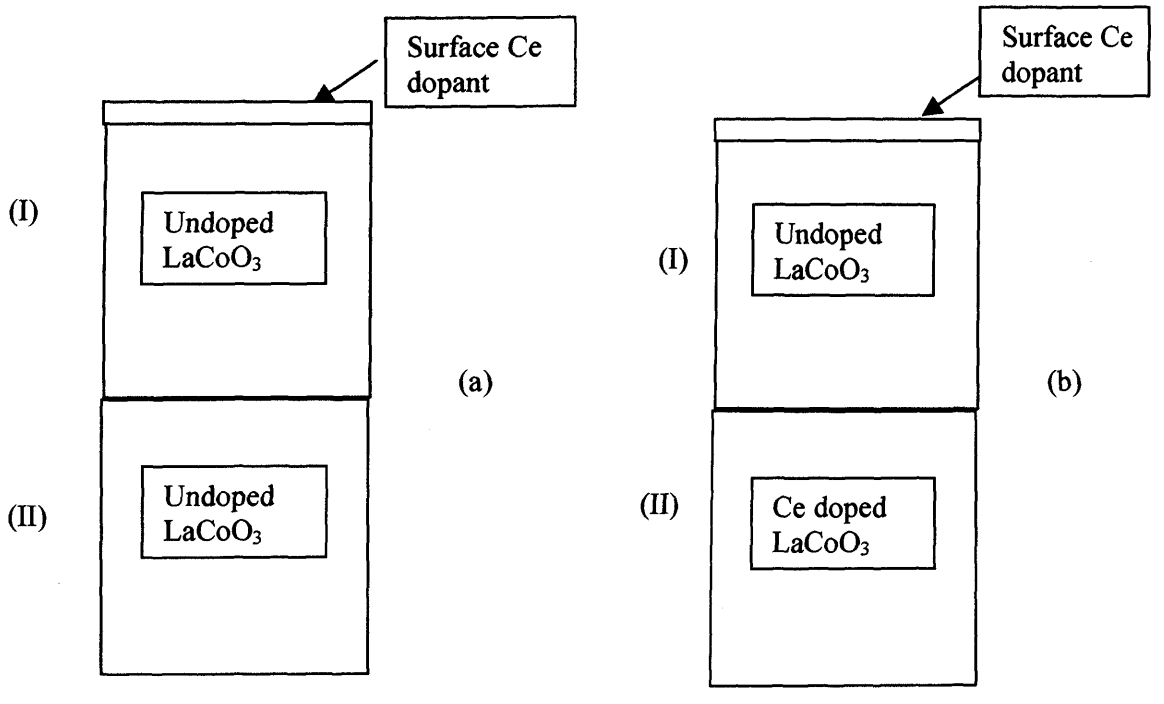

Figure 6.3 *Surface energy calculations for surface Ce doped materials (a) Calculation in MARVIN (b) Correction involving surpercell calculations*

6.2 Solubility of Cerium at Stoichiometric $LaCoO_3$ Surfaces

The relaxed stoichiometric structures shown in **Figures 6.1**, (100)OLa, (100)OCoO and (110)O terminated, which represent the most stable surfaces for stoichiometric $LaCoO_3$, have been selected for further simulations to calculate the solubility energy of Ce substituted at the La site according to the two reactions (6.1) to (6.2) above, involving creation of La vacancies (6.1) or reduction of Co^{3+} to Co^{2+} (6.2). Results for these modelling studies are presented below in **Sections 6.2.1** and **6.2.2**. The calculated solution energies per Ce^{4+} ion from equations (4.8) and (4.9) are presented in **Table 6.2** and the corresponding surface energies are tabulated in **Table 6.3**. For comparison, the bulk Ce^{4+} solution energies calculated in **Section 4.3** are also included in **Table 6.2**.

6.2.1 Creation of La Vacancies

According to equation (6.1) above, substitution of three Ce^{4+} ions at La^{3+} sites results in the creation of one lanthanum vacancy in order to maintain a charge balance. **Figure 6.4** shows Ce doped in the $LaCoO_3$ surface lattice according to this regime for each of the three surfaces selected for this study, together with the relaxed structures after energy minimization of the Ce doped surfaces.

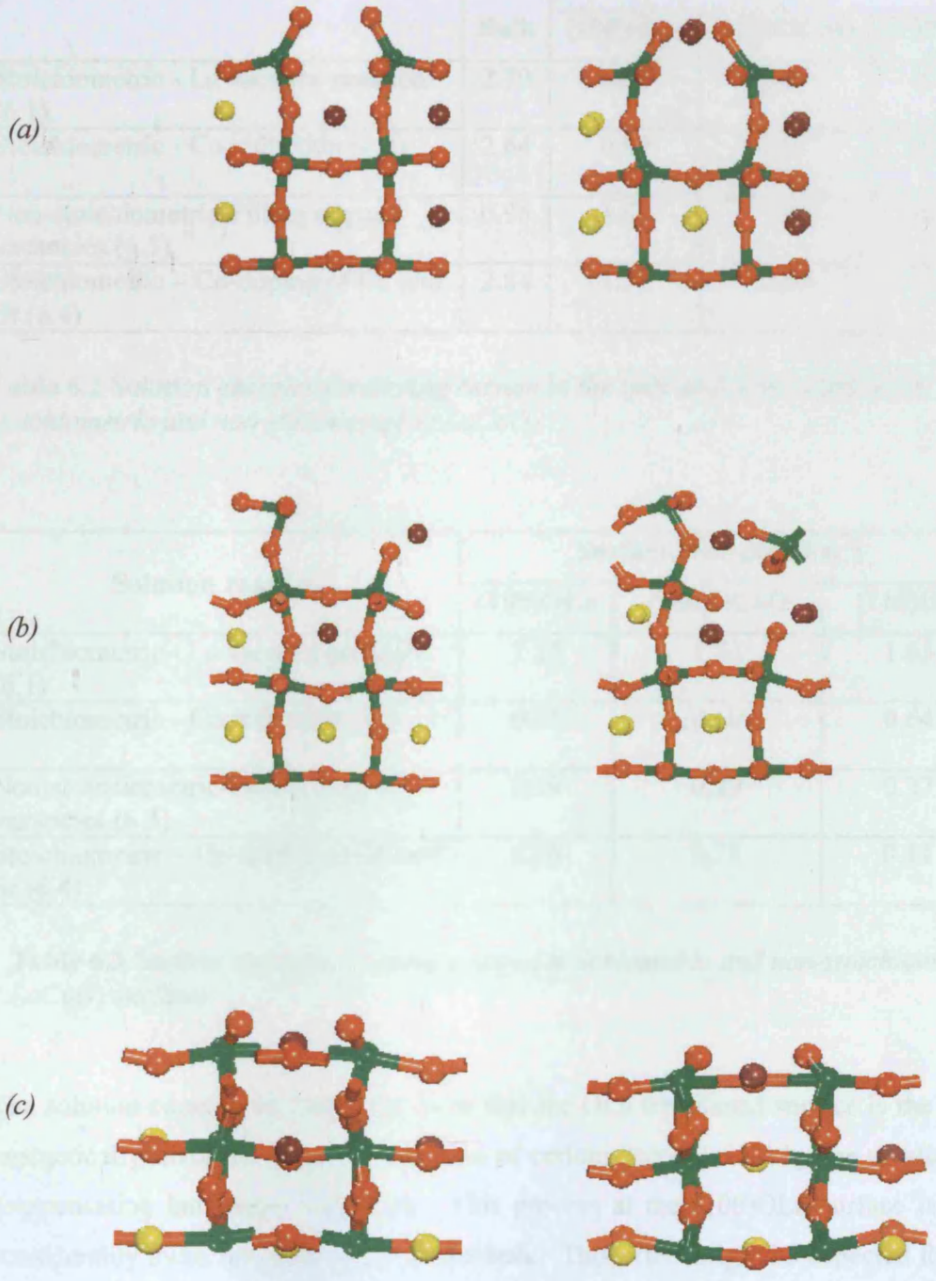

Figure 6.4 *The unrelaxed and relaxed structures for the Ce doped (a) (100)OLa, (b) (100)OCoO and (c) (110)O terminated surfaces of stoichiometric LaCoO containing La^{3+} vacancies (Lattice sites are colour coded as La^{3+} O^{2-} Co^{3+} Ce^{4+})*

Solution reaction	Ce^{4+} solution energies (eV)			
		Surfaces		
	Bulk	(100)OLa	(100)OCoO	(110)O
Stoichiometric - La vacancy creation (6.1)	2.70	0.64	2.27	2.74
Stoichiometric - Co reduction (6.2)	2.64	0.99	0.03	0.69
Non-stoichiometric-Filling oxygen vacancies (6.3)	0.95	1.55	1.34	0.97
Stoichiometric – Co-doping of Ce and Sr (6.4)	2.84	1.98	2.00	1.28

Table 6.2 Solution *energies for doping cerium in the bulk and at the surface for stoichiometric and non-stoichiometric $LaCoO_3$*

Solution reaction	Surface energies (J/m^2)		
	(100)OLa	(100)OCoO	(110)O
Stoichiometric - La vacancy creation (6.1)	1.15	1.52	1.63
Stoichiometric - Co reduction (6.2)	0.71	0.60	0.64
Non-stoichiometric-Filling oxygen vacancies (6.3)	0.99	0.89	0.37
Stoichiometric – Co-doping of Ce and Sr (6.4)	0.26	0.78	0.11

Table 6.3 Surface *energies for cerium doped stoichiometric and non-stoichiometric $LaCoO_3$ surfaces*

The solution energies in **Table 6.2** show that the OLa terminated surface is the most energetically favoured for the dissolution of cerium accompanied by the creation of compensating lanthanum vacancies. This process at the (100)OLa surface is also considerably more favourable than in the bulk. This effect might be expected for the (100)OLa termination as the lanthanum vacancy is created at the exposed surface, which is likely to be easier compared to the other terminations where the lanthanum vacancy is below the exposed surface. It can also be shown that the saturation of the oxygen vacancies can be a contributing factor for the stability of the structure. In addition, a calculation for a Ce doped (100)OLa terminated surface, with the La vacancy created below the exposed surface, gives a solution energy of 2.32eV, which

is considerably higher compared to the solution energy where the vacancy is exposed at the surface. The dissolution of Ce therefore occurs preferentially at the surface.

Figure 6.4a shows the relaxed (100)OLa surface structure with the lanthanum vacancy created at the surface and the three cerium ions in the sub surface layers. Relaxation causes the cerium to be displaced towards the lanthanum vacancy. This displacement of the cerium ion causes rearrangement of the lower layers away from the bulk structure.

Figure 6.4b shows the relaxed (100)OCoO surface where the lanthanum vacancy is below the exposed surface. Substituting the three cerium ions into the relaxed structure causes major rearrangement of the ions and leads to a less stable configuration as shown in **Figure 6.4d**.

Similarly **Figure 6.4c** shows the relaxed surface structure for the (110)O termination, where the lanthanum vacancy is also below the exposed surface which shows the displacement of the cerium ions away from the bulk and there is a displacement of the CoO_6 octahedra.

It has therefore been shown that for both the (100)OCoO and (110)O terminations, cerium is less soluble since the lanthanum vacancy is created below the exposed surface atoms requiring more extensive relaxation in the sub-surface and therefore higher solution energies which approach the bulk value.

Table 6.3 shows that the Ce doped (100)OLa termination has the lowest surface energy for reaction (6.1) confirming that the (100)OLa termination is the most favoured plane for this reaction. The comparison of the undoped stoichiometric material with the Ce doped material can be made from **Tables 6.1** and **6.3**. It can be seen that the surface energies for the stoichiometric surfaces in **Table 6.1** are higher compared to the Ce doped surface in **Table 6.3**. Therefore it is apparent that doping with cerium creates a more stable surface. From **Table 6.2** it is interesting to see that the solution energies follow the same trend as the surface energies for the different surfaces in **Table 6.3**.

6.2.2 Reduction of Co^{3+}

The second reaction for the dissolution of Ce in stoichiometric $LaCoO_3$ involves reduction of one Co^{3+} to Co^{2+} for each Ce^{4+} substituted at a La^{3+} site as in equation (6.2). **Figure 6.5** shows Ce doped in the $LaCoO_3$ surface lattice according to this regime for each of the three surfaces selected for this study, together with the relaxed structures after energy minimization of the Ce doped surfaces.

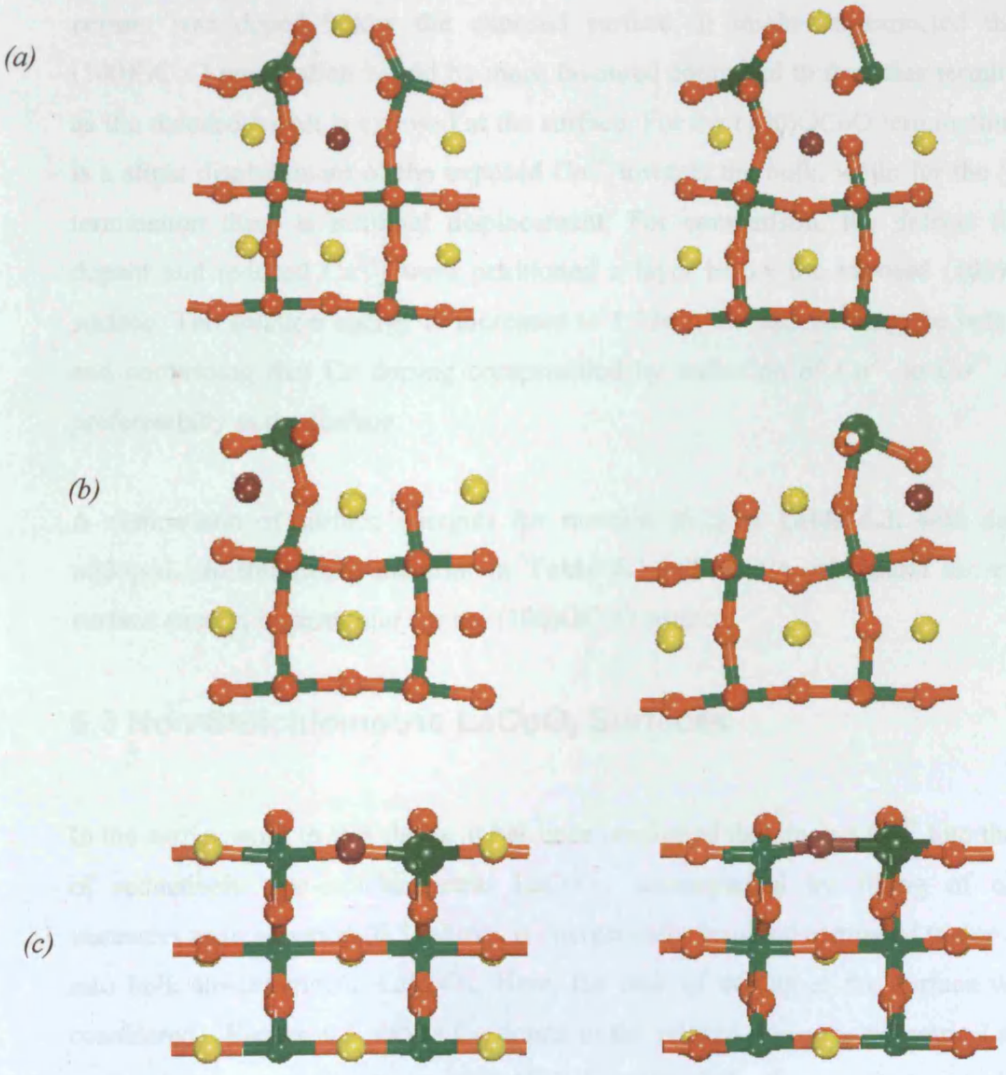

Figure 6.5 *The unrelaxed and relaxed structures for the Ce doped (a) (100)OLa, (b) (100)OCoO and (c) (110)O surfaces of stoichiometric $LaCoO_3$ containing Co^{2+} cations. (Lattice sites are colour coded as La^{3+} O^{2-} Co^{3+} Co^{2+} Ce^{4+})*

From the solution energies in **Table 6.2** we note that doping cerium and reducing Co^{3+} to Co^{2+}at the surface is a more favoured reaction compared to the bulk for all three surface terminations studied, with (100)OCoO being significantly more favoured compared to the others. The difference between bulk and surface doping may stem from the greater ease of relaxation at the surface to reach a more stable energy minimized structure. For the (100)OLa termination it was shown that when cerium was doped at the exposed surface the solution energy increased to 1.10eV. Therefore, the most favoured structure for the (100)OLa termination was when the cerium was doped below the exposed surface. It might be expected that the (100)OCoO termination would be more favoured compared to the other terminations as the reduced cobalt is exposed at the surface. For the (100)OCoO termination there is a slight displacement of the exposed Co^{2+} towards the bulk, while for the (110)O termination there is minimal displacement. For comparison, the defects (cerium dopant and reduced Co^{2+}) were positioned a layer below the exposed (100)OCoO surface. The solution energy is increased to 1.97eV, i.e. approaching the bulk value and confirming that Ce doping compensated by reduction of Co^{3+} to Co^{2+} occurs preferentially at the surface.

A comparison of surface energies for reaction (6.2) in **Table 6.3,** with data for undoped, stoichiometric material in **Table 6.1** indicates a substantial decrease in surface energy, in particular for the (100)OCoO surface.

6.3 Non-Stoichiometric $LaCoO_3$ Surfaces

In the earlier work in this thesis, it has been confirmed that doping Ce^{4+} into the bulk of reductively non-stoichiometric $LaCoO_3$, accompanied by filling of oxygen vacancies as in equation (6.3) above, is energetically favoured compared to doping Ce into bulk stoichiometric $LaCoO_3$. Here, the case of doping at the surface will be considered. **Figure 6.6** shows Ce doped in the relaxed non-stoichiometric $LaCoO_3$ surface lattice according to equation (6.3) for each of the three surfaces selected for this study, together with the relaxed structures after energy minimization of the Ce doped surfaces. Solution energies from equation (4.11) and surface energy results are

presented in **Tables 6.2** and **6.3** respectively together with the corresponding bulk solution energy data.

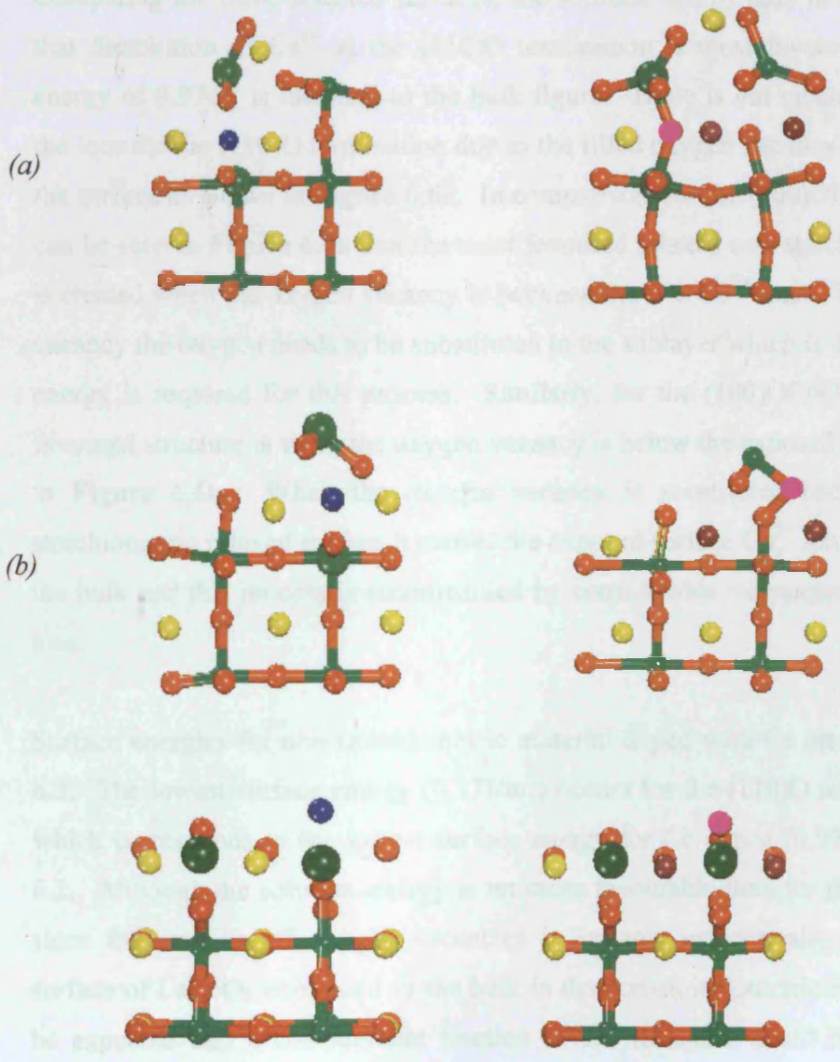

Figure 6.6 *The unrelaxed and relaxed structures for the Ce doped (a)(100)OLa, (b) (100)OCoO and (c) (110) O terminated surfaces non-stoichiometric $LaCoO_3$ resulting in filling of oxygen vacancies. (Lattice sites are colour coded as La^{3+} O^{2-} Co^{3+} Ce^{4+} Co^{2+} O^{2-} vacancy filled oxygen site*

The results for solution energies in **Table 6.2** show that doping Ce into the reductively non-stoichiometric surfaces is no more favourable energetically than the

equivalent process in the bulk but is still more favourable than for bulk dissolution processes in the stoichiometric material.

Comparing the three selected surfaces, the solution energy data in **Table 6.2** shows that dissolution of Ce^{4+} at the (110)O termination is most favoured. The solution energy of 0.97eV is identical to the bulk figure. There is not much displacement of the ions for the (110)O termination due to the filled oxygen vacancy being exposed at the surface as shown in **Figure 6.6c**. In comparison, for the (100)OLa termination, it can be seen in **Figure 6.6a** that the most favoured relaxed non-stoichiometric surface is created when the oxygen vacancy is between the two Co^{2+} ions. To fill the oxygen vacancy the oxygen needs to be substituted in the sublayer which is difficult and more energy is required for this process. Similarly, for the (100)OCoO termination, the favoured structure is when the oxygen vacancy is below the exposed surface as shown in **Figure 6.6b**. When the oxygen vacancy is substituted back into the non-stoichiometric relaxed surface it causes the exposed surface Co^{2+} ion to move towards the bulk and this process is accompanied by considerable rearrangement of the other ions.

Surface energies for non-stoichiometric material doped with Ce are shown in **Table 6.3**. The lowest surface energy ($0.37J/m^2$) occurs for the (110)O terminated surface which corresponds to the lowest surface energy for Ce doped (0.97eV) as in **Table 6.2**. Although the solution energy is no more favourable than for the bulk material, since the creation of oxygen vacancies is strongly energetically favoured at the surface of $LaCoO_3$ compared to the bulk in the non-stoichiometric material, it might be expected that a considerable fraction of the vacancies could be 'filled' at the surface as a result of Ce doping.

6.4 Co-doping of Ce and Sr

According to equation (6.4), one Sr^{2+} ion must be substituted at a La^{3+} site for each Ce^{4+} substituted in stoichiometric $LaCoO_3$ to maintain a charge balance. **Figure 6.7** shows Ce and Sr doped in the $LaCoO_3$ surface lattice according to this regime for each of the three surfaces selected for this study, together with the relaxed structures after energy minimization. Solution energy results from equation (4.13) and surface energy

data are shown in **Tables 6.2** and **6.3** respectively together with the solution energy for the bulk process.

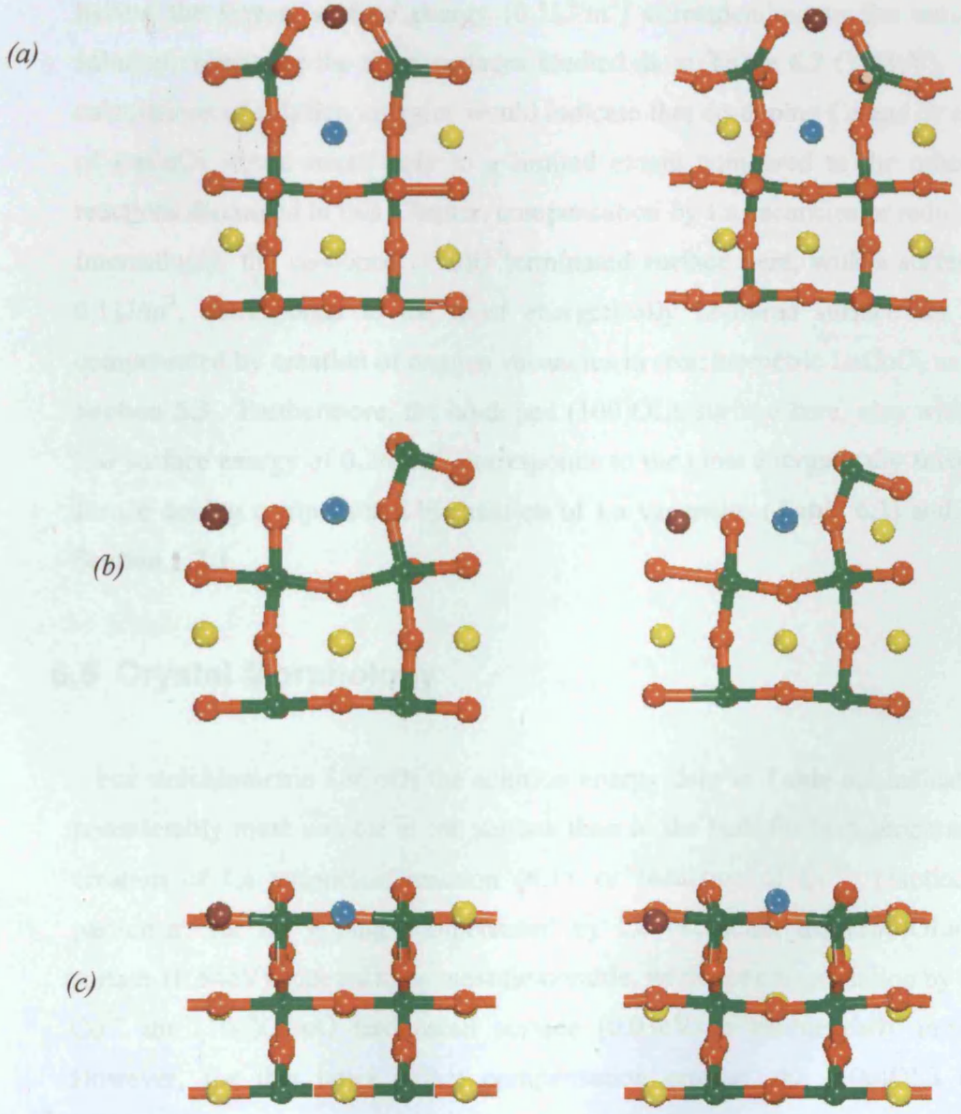

Figure 6.7 *The unrelaxed and relaxed structures for the Ce and Sr (a) (100)OLa, (b) (100)OCoO and (c) (110)O terminated surfaces of stoichiometric $LaCoO_3$ (Lattice sites are colour coded as La^{3+} O^{2-} Co^{3+} Sr^{2+} Ce^{4+})*

The results in **Table 6.2** indicate that the solution energy for Ce^{4+} co-doped with Sr^{2+} at the (110)O surface of stoichiometric $LaCoO_3$ is more favourable than in the bulk but it

is not energetically favoured compared to the other defect compensation reactions simulated as in equations (6.1) and (6.2). However, for surface co-doping, the data in **Table 6.3** shows substantial reduction in surface energies compared to those for undoped, stoichiometric $LaCoO_3$, (**Table 6.1**), with the (110)O terminated surface having the lowest surface energy ($0.11J/m^2$) corresponding to the most favourable solution energy for the three surfaces studied as in **Table 6.2** (1.28eV). Overall, the calculations of solution energies would indicate that co-doping Ce and Sr at the surface of $LaCoO_3$ would occur only to a limited extent compared to the other Ce doping reactions discussed in this Chapter, compensation by La vacancies or reduction of Co^{3+}. Interestingly, the co-doped (110)O terminated surface here, with a surface energy of $0.11J/m^2$, corresponds to the most energetically favoured surface for Sr^{2+} doping compensated by creation of oxygen vacancies in stoichiometric $LaCoO_3$ as discussed in **Section 5.3**. Furthermore, the co-doped (100)OLa surface here, also with a relatively low surface energy of $0.26J/m^2$, corresponds to the most energetically favoured surface for Ce doping compensated by creation of La vacancies (**Table 6.2**) and discussed in **Section 6.2.1**.

6.5 Crystal Morphology

For stoichiometric $LaCoO_3$ the solution energy data in **Table 6.2** indicate that Ce is considerably more soluble at the surface than in the bulk for both processes involving creation of La vacancies, reaction (6.1), or reduction of Co^{3+}, reaction (6.2). In particular, for Ce doping compensated by La vacancies, the (100)OLa terminated surface (0.64eV) appears to be most favourable, while for compensation by reduction of Co^{3+} the (100)OCoO terminated surface (0.03eV) is energetically most favoured. However, for this latter defect compensation process, the (100)OLa and (110)O terminated surfaces also show lower energies for Ce dissolution compared to the bulk. The solution energy data are mirrored in the surface energy data in **Table 6.3**.

In reconciling the data for solution energies and surface energies it is important to remember that the surface energy defines which faces are likely to occur in a crystal, while solution energy determines how easily Ce will dissolve in a particular surface. For example here, from the surface energy data in **Table 6.3**, it can be seen that the

(100)OLa termination is likely to dominate the crystal morphology for the material containing La vacancies, while for reduction of Co^{3+} the (100)OCoO terminated surface is only marginally more stable than the other two faces studied. However we should note that in the undoped stoichiometric material, (100)OCoO was the least stable of the three selected surfaces (**Table 6.1**), i.e. the high degree of solubility of Ce^{4+} corresponds to a higher level of stabilization. Predicted morphologies, using the equlibrated morphology method as discussed in **Section 5.4**, for both options for doping Ce^{4+}, La vacancy creation or Co^{3+} reduction, are depicted in **Figure 6.8.**

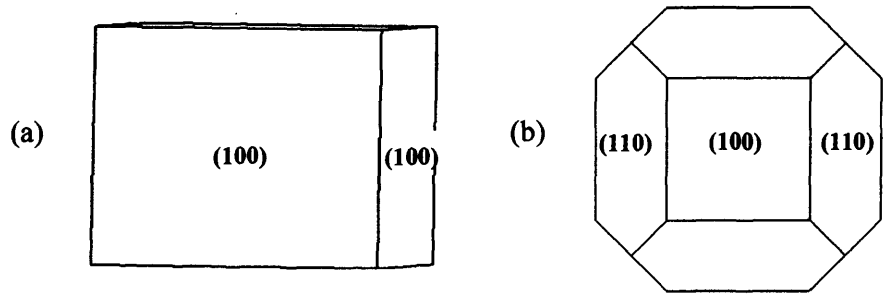

Figure 6.8 *The relaxed crystal morphologies for Ce doped stoichiometric $LaCoO_3$ (a) Creation of La vacancies (b) Reduction of Co^{3+}.*

In the case of non-stoichiometric $LaCoO_3$, where dissolution of Ce^{4+} results in filling oxygen vacancies, the solution energy data in **Table 6.2** shows that the surface process is no more favourable than in the bulk. However, since the concentration of oxygen vacancies at the surface of the prepared material is predicted to be greater than in the bulk, it is probable that a significant fraction of doped Ce will be concentrated at the surface. The resulting predicted crystal morphology is shown in **Figure 6.9** indicating dominance by the (110)O terminated surface. The predicted crystal morphology for materials co-doped with Ce and Sr is also shown in **Figure 6.9** indicating a predominance of the (110)O terminated and (100)OLa terminated faces.

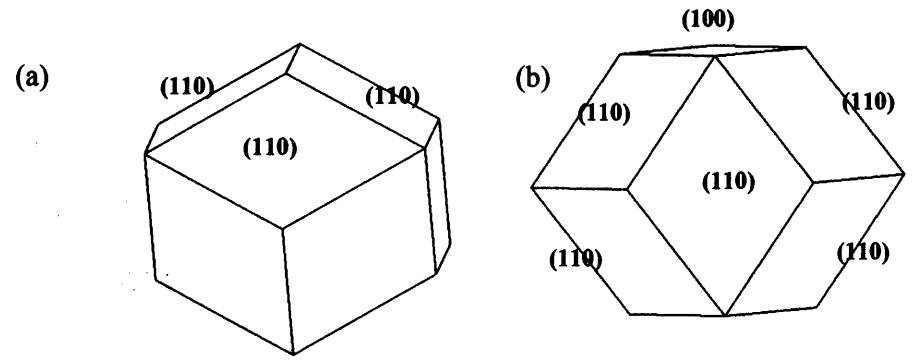

Figure 6.9 *The relaxed crystal morphologies for Ce doped $LaCoO_3$ (a) Filling oxygen vacancies in non-stoichiometric material (b) Co-doping of Ce and Sr in stoichiometric material.*

6.6 Implication for Catalysis

The data in **Table 6.2** and **6.3** represents a complex pattern of results. In order to interpret these data in terms of the implications for catalysis, three areas require discussion. The first is the extent to which Ce can be concentrated at the surface in order to have a significant effect on catalysis. Second is a discussion on which of the several competing Ce dissolution processes represented by equations (6.1) to (6.3) is most likely to occur during the preparation of real catalytic materials. Finally, possible reactions for the involvement of Ce in catalytic oxidation processes need to be explored.

Therefore, it is instructive first of all to quantify the potential levels of surface dopant, Ce, in real, polycrystalline $LaCoO_3$ catalytic materials. In this respect, Kaliaguine *et al* have carried out a series of $LaCoO_3$ preparations as part of a study on oxygen exchange at $LaCoO_3$ surfaces as discussed in **Section 2.3.4**[6]. In this work, the authors observed a strong correlation between calcination temperature, the development of crystallinity as expressed by the XRD pattern, the increase in crystallite size derived from X-ray peak widths according to the Scherrer equation and the decrease in N_2 adsorption, BET surface area. However, there was poor agreement

between absolute, XRD crystallite size measurements and that derived from BET surface areas, which has been attributed to grain boundary contacts between crystallites making a substantial fraction of the surface inaccessible to adsorption of N_2 molecules. It is important, therefore, to take the crystallite size from XRD to estimate surface dopant levels[6]. Taking a typical catalytic $LaCoO_3$ material calcined at 900°C with a BET surface area of ~$1m^2/gm$[7] and interpolating the data of Kaliaguine *et al* leads to an estimate of crystallite size of ~50nm with a true surface area of ~$17m^2/gm$. For a crystallite of this size, the outer layer one unit cell deep is equivalent to ~5% of the volume of the material which is shown in **Appendix 1.**

In relation to Ce doping, the point at which Ce segregation begins is not known but the overall solubility with reference to the bulk, as determined by XRD, has been shown to be very low and no higher than 5%[8] in accordance with the dissolution reaction proposed by French *et al* and confirmed here[3]. If we assume substitution at a level of 5% of the total La sites in stoichiometric $LaCoO_3$ with respect to the bulk, nearly 7% of the total La sites would actually be involved in the situation where defect compensation occurs via creation of La vacancies according to equation (6.1) since for every three Ce^{4+} ions dissolved, one La^{3+} vacancy is created. This level of doping cannot be accommodated in the outer surface extending to a depth of one unit cell but requires a depth of two unit cells. A more realistic model would be an enriched surface layer with a Ce concentration gradient extending into the subsurface. This model, which has not been verified experimentally, is idealised in **Figure 6.10**. For comparison, the computational model with Ce substitution compensated by La vacancy creation in **Section 6.2.1** assumes all of the surface La sites are involved which is derived in **Appendix 2A**.

In the case of defect compensation by reduction of Co^{3+}, a substitution level of 5% would involve 5% of the total La sites as in equation (6.2). This level could be accommodated in a surface layer one unit cell deep, but there have been no careful doping experiments supported by XPS or LEIS measurements to confirm this proposal. Again, a more realistic model would be segregation of defects at the surface but with a concentration gradient, which extends into the subsurface as in **Figure 6.10**. For comparison, the computational model in **Section 6.2.2**, based on

compensation by reduction of Co^{3+}, assumes a lower level of Ce substitution equivalent to ~33% of the surface La sites corresponding to reduction of half the surface Co ions shown in **Appendix 2B**.

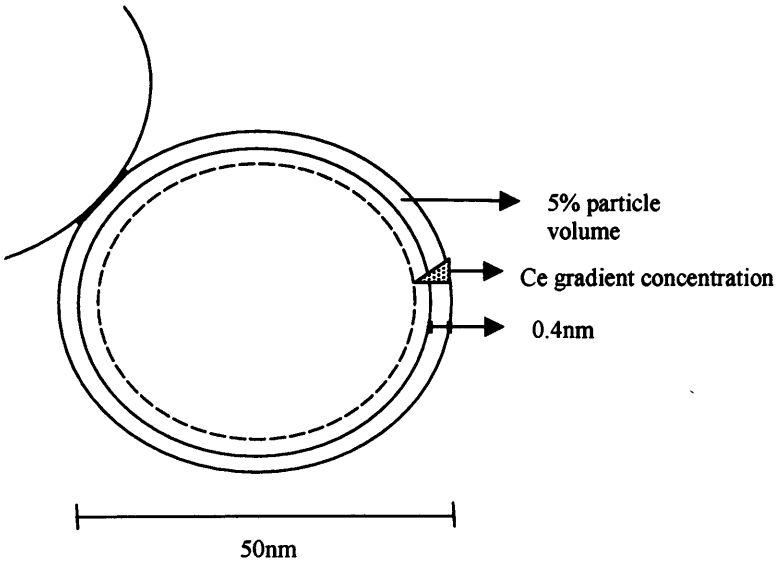

Figure 6.10 *Idealised model for particles of Ce doped $LaCoO_3$*

Now let us consider non-stoichiometric material, which typically has a composition between $LaCoO_{2.94}$ and $LaCoO_3$[9]. This level of reductive non-stoichiometry corresponds to loss of ~1% of the total oxygen anions while ~6% of the total Co^{3+} cations are reduced to Co^{2+} as in equation (6.5):

$$2Co_{Co}^{x} + O_{o}^{x} \rightarrow 2Co_{Co}^{'} + V_{o}^{\bullet\bullet} + 1/2\,O_2 \qquad (6.5)$$

The results in **Section 5.3.2** predict that oxygen vacancies are preferentially created at the surface. However, the limiting factor in dispersion of the resulting oxygen vacancies is the availability of compensating Co^{2+} cations. In principle, the non-stoichiometry could be accommodated in the outermost layer to a depth of two unit cells. The presence of such a concentration of Co^{2+} at the surface has not been verified by careful XPS measurements. However, a more realistic model would be segregation of oxygen vacancies at the surface, compensated by Co^{2+}, but with a gradient of non-stoichiometry extending towards the bulk. For comparison, the model

used in the computational studies in **Section 5.3.2** corresponds to a level of ~13% of the surface oxygens removed as vacancies shown in **Appendix 2C**.

In the case of Ce doping in non-stoichiometric $LaCoO_3$, containing oxygen vacancies and Co^{2+} cations, two Ce^{4+} cations are required to balance the filling of one oxygen vacancy as in equation (6.3). The end result will be effectively similar to the case discussed above where Ce^{4+} dissolution in stoichiometric $LaCoO_3$ is compensated by formation of Co^{2+} cations. Since formation of oxygen vacancies in non-stoichiometric material and Ce^{4+} doping in stoichiometric $LaCoO_3$ balanced by Co^{3+} reduction are both energetically favoured processes at the surface, it is probable that in a real preparation involving air calcination at 900°C Ce will be enriched at the surface.

The above discussion indicates that the formation of a Ce enriched surface on particles of $LaCoO_3$ prepared by typical precipitation and calcinations methods is feasible. The details in terms of concentration and dispersion will depend on calcination temperature, which controls both crystallite size, i.e. surface area through sintering, and the potential number of oxygen vacancies, which enhances Ce solubility.

For the various Ce doping reactions discussed above, and represented by equations (6.1) to (6.3), caution is required in deciding which will be most energetically favoured from the solution energy data in **Table 6.2** since some of the parameters in the equations (4.8), (4.9) and (4.11) used to derive solution energies may not be sufficiently precise. The most important consideration in determining which process dominates is the oxygen partial pressure during material preparation. From equation (6.2) we can see that Ce doping compensated by Co reduction would be strongly favoured at lower oxygen partial pressures. Also, it has been established experimentally that typical preparations of catalytically active $LaCoO_3$ via precipitation from solution followed by air calcination at 900°C produce slightly reductively non-stoichiometric material according to equation (6.5). Therefore in a real preparation involving Ce doping it is probable that the resulting material will be Ce^{4+} enriched at the surface via the process represented by equation (6.3) and

compensated by the presence of Co^{2+}. In order to produce material where Ce^{4+} doping occurs with defect compensation by formation of La^{3+} vacancies as in equation (6.1), calcination under pure oxygen, possibly under pressure, would be required.

The role of Ce as a dopant in oxidation catalysis has been considered by Wu *et al*, who have proposed that Ce^{4+} enhances oxidation of ammonia in a linked redox process with Co as shown in **Figure 2.15** via the redox equations:

$$2Co_{Co}^{3+} + O_O^{2-} \Leftrightarrow 2Co_{Co}^{2+} + V_O^{\bullet\bullet} + O^{\bullet} \quad (6.6)$$

$$2Co_{Co}^{2+} + V_O^{\bullet\bullet} + O_s^{2-} \Leftrightarrow 2Co_{Co}^{3+} + O_O^{2-} \quad (6.7)$$

$$2Ce_{La}^{4+} + O_O^{2-} \Leftrightarrow 2Ce_{La}^{3+} + V_O^{\bullet\bullet} + O_s^{2-} \quad (6.8)$$

$$2Ce_{La}^{3+} + V_O^{\bullet\bullet} + 1/2\,O_2 \Leftrightarrow 2Ce_{La}^{4+} + O_O^{2-} \quad (6.9)$$

where the active oxygen species $O^{\bullet}$ reacts with ammonia (or methane) and O_s^{2-} is a mobile oxygen anion transported from the oxygen capture site (Ce) to the oxidation reaction site (Co) through the subsurface via the ion redox model for intrafacial catalysis as depicted in **Figure 2.9**. The catalytically active Co site and the Ce site responsible for oxygen capture could of course be adjacent to one another. We should note that the activation processes for reaction substrates such as NH_3 or CH_4 are not understood. For example, it is not certain whether CH_4 activation occurs via adsorption or directly via interaction with an active adsorbed oxygen species[10].

This description implies that Ce enhances the gas phase oxygen capture process while the oxidation reaction occurs at the Co site. However, Wu *et al* have not considered the defect compensation processes required to balance the inclusion of Ce^{4+} in the $LaCoO_3$ lattice[11]. In the case of defect compensation by reduction of Co^{3+} to Co^{2+}, one redox active species, Co^{3+}, is effectively replaced by another, Ce^{4+}. It can be argued that this process would reduce catalytic oxidation activity rather than enhance it since, in relation to the $Ce^{4+} \Leftrightarrow Ce^{3+}$ and $Co^{3+} \Leftrightarrow Co^{2+}$ redox reactions, the fourth ionization potential for Ce is 3.3eV greater than the third ionization potential for

Co[12]. This difference in redox potential is reflected in the higher enthalpy of reduction per reduced cation for CeO_2 reduction to Ce_2O_3 compared to Co_3O_4 reduction to CoO. The enthalpies for Ce^{4+} and Co^{3+}reduction in an oxide environment have been estimated to be 191 kJ/ion and 89 kJ/ion respectively (i.e. half of (6.10) and (6.11)) from the enthalpies of formation for the individual solid oxides as in the equations below[12]:

$$2CeO_2 \rightarrow Ce_2O_3 + 1/2\,O_2 \qquad \Delta H = 381.2\text{kJ} \qquad (6.10)$$

$$Co_3O_4 \rightarrow 3CoO + 1/2\,O_2 \qquad \Delta H = 177.3\text{kJ} \qquad (6.11)$$

These values would indicate that Ce would be more effective at oxygen capture while Co would be more active as a catalytic oxidation site. However, the higher energy required to reduce Ce^{4+} would impact on the oxygen transport process required to re-oxidise Co^{2+}.

In contrast, the alternative defect compensation process, Ce substitution at the La site accompanied by creation of La vacancies in equation (6.1), could enhance the overall redox capability of the surface. In this second reaction, La^{3+}, which effectively acts as a bystander in the catalytic process, is replaced by the redox active species Ce^{4+}. Other factors, which could enhance catalysis, are an increase in surface disorder, which would promote oxygen anion transport to the reaction site, and the creation of La vacancies, which may influence adsorption processes.

The discussion above on possible involvement of Ce in the catalytic oxidation process suggests that Ce^{4+} may be less effective in terms of redox behaviour than Co^{3+}. In this respect, Kirchinerova *et al* have shown that phase segregated CeO_2 in Ce doped $LaCoO_3$ formulations would have relatively low activity for CH_4 combustion compared to $LaCoO_3$[13]. However, the important comparison is not with Co^{3+} rich stoichiometric $LaCoO_3$ surfaces but between catalytic behaviour over undoped, reductively non-stoichiometric $LaCoO_3$ surfaces and Ce doped surfaces prepared under real conditions. The former material presents a surface rich in oxygen vacancies compensated by Co^{2+} as in **Figure 6.11a**. In contrast, the Ce doped surface is rich in oxygen, since oxygen vacancies are filled, and some La^{3+} is replaced by redox active Ce^{4+} cations as in **Figure 6.11b**. This oxygen rich surface is effectively fully charged

for high temperature, intrafacial catalytic oxidation whereas the oxygen vacancy containing, undoped non-stoichiometric surface requires activation by capture of oxygen from the gas phase or transport of oxygen anions from the subsurface.

Interestingly, this model for enhancement of high temperature, intrafacial oxidation catalysis by Ce^{4+} incorporation in the $LaCoO_3$ surface suggests that more effective materials might be produced by preparation under more oxidising conditions, i.e. calcinations under pure oxygen. In the case of undoped $LaCoO_3$, preparation under strongly oxidising conditions would result in an oxygen vacancy free surface as in **Figure 6.11c**, where Co is present as Co^{3+}. For Ce doped materials, a significant fraction of 'inert' La^{3+} would be replaced by redox active Ce^{4+} cations, compensated by creation of La vacancies, as in equation (6.1) and shown in **Figure 6.11d**. These surfaces should be highly active for high temperature, intrafacial oxidation catalysis such as CH_4 combustion and NH_3 oxidation. Co-doping by Ce^{4+} and Sr^{2+} would also enhance activity since La^{3+} is replaced by a redox active species.

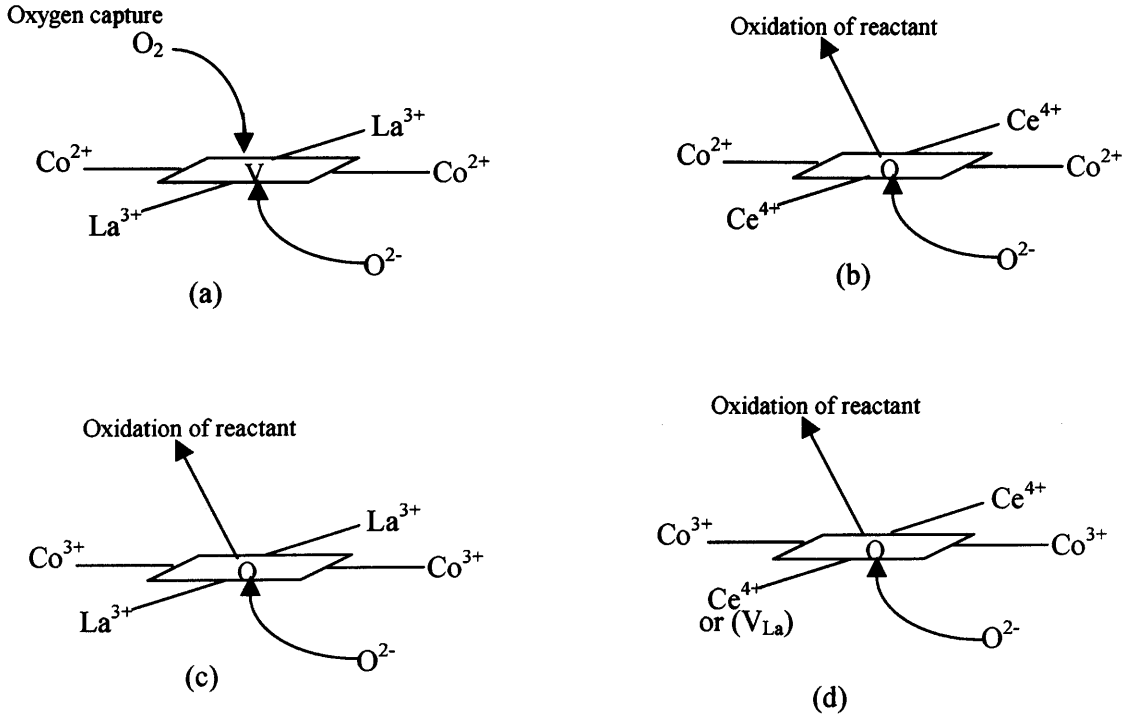

Figure 6.11 *Intrafacial oxidation catalysis over $LaCoO_3$ surfaces (a)Non- stochiometric (b)Air calcined, Ce doped (c) Stoichiometric (d) Oxygen calcined, Ce doped.*

The proposed model for Ce doped $LaCoO_3$ surfaces in high temperature, intrafacial oxidation may also explain behaviour under lower temperature, suprafacial conditions where experimental results indicate that Ce doping can reduce activity. In the suprafacial process, it has been proposed that oxygen is activated as O_2^- by adsorption of gaseous oxygen at oxygen vacancies. However the effect of Ce doping, for air calcined materials is to fill oxygen vacancies. The surface oxygens only become active at higher temperatures when the lattice anion mobility increases.

6.7 Summary and Conclusions

Previously in **Chapter 4,** Mott Littleton calculations were reported for doping Ce in bulk $LaCoO_3$. These bulk calculations showed that Ce has low solubility in stoichiometric $LaCoO_3$. However, it was shown that Ce is more soluble in the non-stoichiometric material resulting in filling oxygen vacancies.

Since catalysis is a surface process, in this Chapter Ce doping has been considered at the surface for the (100)OLa, (100)OCoO and (110)O terminated surfaces. Our calculations have shown in **Table 6.2** that Ce is more soluble at the surface for stoichiometric $LaCoO_3$ compared to the bulk. The surface energy data (**Table 6.3**) mirrors the solution energy data (**Table 6.2**). It can be seen for the La vacancy reaction (6.1) that the (100)OLa terminated surface will be the most energetically favoured, and for the Co^{3+} reduction reaction (6.2), the (100)OCoO termination is slightly more favoured compared to the other terminations. The calculation for dissolution of Ce in non-stoichiometric $LaCoO_3$ surfaces shows that the (110)O termination is the most favoured. These terminations can be visualised in the crystal morphology as shown in **Figures 6.8** and **6.9**.

From XRD and surface area data in the literature, a model has been proposed for air calcined, Ce doped, $LaCoO_3$ particles consisting of crystallites of ~50nm in diameter with a surface enriched Ce layer, as predicted by our calculation, but with a concentration gradient extending in to the subsurface. Such a model would accommodate a maximum level of 5% Ce in total with respect to the bulk as indicated by experiment.

In considering which of the competing Ce doping reactions in equations (6.1) to (6.3) is likely to occur during preparation of real materials, the most important factor is oxygen partial pressure. For air calcined materials at 900°C, where reductively non-stoichiometric $LaCoO_3$ containing oxygen vacancies balanced by Co^{2+} cations would be produced in the absence of Ce, we suggest that Ce doping occurs at the surface to give a material equivalent to that formed via equation (6.2). This process, which is favoured at lower oxygen partial pressure, would produce oxygen vacancy free material where Co^{2+} compensates Ce^{4+}. It is predicted that Ce^{4+} doping compensated by La^{3+} vacancies would occur under strongly oxidising conditions, i.e. pure oxygen, possibly under pressure.

The role of Ce as a dopant in enhancing high temperature, intrafacial, oxidation catalysis has been discussed in relation to the model proposed by Wu *et al* involving a linked redox cycle for Ce and Co. In comparison to undoped, reductively non-stoichiometric $LaCoO_3$ surfaces, Ce doping results in replacement of 'inert' La^{3+} cations by redox active Ce^{4+} and the surface (and sub-surface) is fully charged with oxygen. A consideration of ionization potentials and enthalpies of reduction for pure Ce and Co solid oxides suggests that Ce would be most effective in oxygen capture while Co would be most effective in the oxidation process in the intrafacial, ion redox catalytic cycle discussed in **Section 2.3.4**. In addition, we predict that materials prepared under strongly oxidising conditions, i.e. undoped fully stoichiometric $LaCoO_3$ or Ce doped, La vacancy containing material will also be effective in high temperature, intrafacial oxidation.

The proposed model for Ce doped $LaCoO_3$ could also explain behaviour under low temperature, suprafacial oxidation conditions, where Ce reduces activity. In the suprafacial reaction, oxygen is proposed to be activated as O_2^- by adsorption in oxygen vacancies. The absence of anion vacancies in Ce doped materials would inhibit this process and surface lattice oxygen would only become active at higher temperature when anion mobility increases.

REFERENCES

(1) V.A.Sadykov; L.A.Isupova; I.A.Zolotarskii; L.N.Bobrova; A.S.Noskov; V.N.Parmon; E.A.Brushtein; T.V.Telyatnikova; V.I.Chernyshev; V.V.Lunin. *Appl. Cat A: Gen.* **2000**, *204*, 59.

(2) L.Forni; J.Rossetti. *Appl. Cat B: Environ.* **2002**, *38*, 29.

(3) S.A.French; C.R.A.Catlow; R.J.Oldman; S.C.Rogers; S.A.Axon. *Chem.Commun*, **2002**, 2706.

(4) D.H.Gay; A.L.Rohl. *J.Chem.Soc. Faraday Trans.* **1995**, *91*, 925.

(5) S.Hamad; S.Cristol; C.R.A.Catlow. *J. Phys.Chem. B* **2002**, *106*, 11002.

(6) S.Royer; D.Duprez; S.Kaliaguine. *Journal of Catalysis* **2005**, *234*, 364.

(7) S.A.Axon; B.Wolfindale. *Johnson Matthey,Private Commuincation*, **2006**.

(8) T.Nitadori; M.Misono. *J. Catal.* **1985**, *93*, 459.

(9) K.Haung; H.Y.Lee; J.B.Goodenough. *J.Electrochem.Soc.* **1998**, *145*, 3220.

(10) D.Hirabayashi; T.Yoshikawa; K.Mochizuki; K.Suzuki; Y.Sakai. *Catal. Letters* **2006**, *110(3-4)*, 269.

(11) Y.Wu; B.Dou; C.Wang; X.Xie; Z.Yu; S.Fa; Z.Fan; L.Wang. *J.Catal* **1989**, *88*, 120.

(12) D.R.Lide *"Handbook of Chemistry and Physics"*, 83rd edition ed.; C.R.C Press.

(13) J.Kirchinerova; M.Alifanto; B.Delmon. *Appl. Cat A: Gen.* **2002**, *231*, 65.

CHAPTER 7

7. QUANTUM MECHANICAL STUDIES OF $LaCoO_3$

Quantum mechanical (QM) methods allow the calculation of ground and excited state properties (including energies and structures, transition states and charge distribution as discussed in **Section 3.2**. In contrast, atomistic methods do not consider the explicit electronic properties of the system and the atomistic method is strongly dependent on the effectiveness of the parameterization used; they are however, far cheaper computationally.

However, owing to the complexity of the problems examined, this thesis has been mainly based on atomistic techniques; but in this chapter QM simulations will be carried out on bulk $LaCoO_3$ using density functional theory (DFT) for a 2x2x2 unit cell, as discussed in **Section 3.2.2**[1]. Following the bulk calculations, defect calculations involving oxygen vacancies will be reported, which are discussed in **Section 7.3**.

7.1 Quantum Mechanical Bulk Studies Of $LaCoO_3$

All calculations used the $DMol^3$ code[1] employing the generalized gradient approximation PW91 functional, which, has been described in detail in **Sections 3.3**. The basis set employed was double numerical with polarisation (DNP), also discussed in **Section 3.2.3**, and calculations were carried out by employing spin polarisation. The integration grid determines the number of mesh points required to evaluate the energies numerically[1]. The grid can have different levels: coarse, medium, fine and xfine. The grid "coarse" has the fewest mesh points and therefore the results are less accurate; however they require less computational time. By contrast, an "xfine" grid gives the greatest accuracy and takes the most computational time. The "medium" grid was initially employed for the calculations carried out in this study.

The first step was to determine the most stable structure by manually adjusting the lattice parameters, which ranged between 7.52Å -7.92Å. **Figure 7.1** reports the

variation with lattice parameter of the binding energy, which is the energy of the solid with respect to free atoms. The quality of the results is clearly insufficient to allow us to identify an energy minimum.

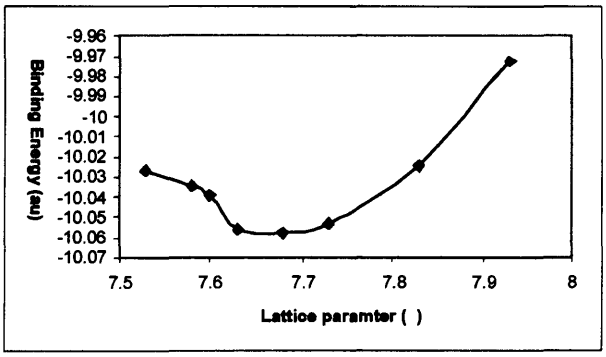

Figure 7.1 *The binding energy data for lattice parameters from 7.52Å-7.92Å*

Therefore, an extensive study was carried to identify the minimum energy structure, initially by increasing the sampling frequency parameter to 0.05Å and taking the lattice parameters to be between 7.55-7.75Å. However, these calculations still did not identify the energy minimum, but produced discontinuities as shown in **Figure 7.2a**. To remove these discontinuities different parameters were changed, for example in (1) the grid was changed from medium to fine as shown in **Figure 7.2b** (2) the functional was changed from PW91 to PBE and a dspp pseudopotential was introduced due to the heavy elements in the $LaCoO_3$ which has been discussed in **Section 3.2.4;** results are shown in **Figure 7.2c.**

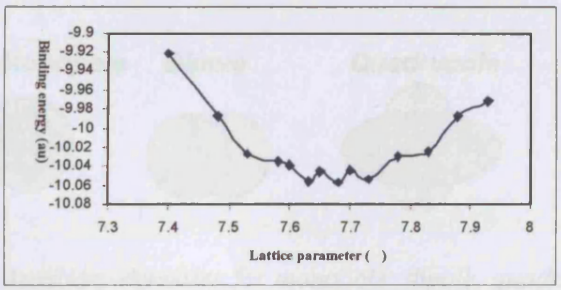

(a)

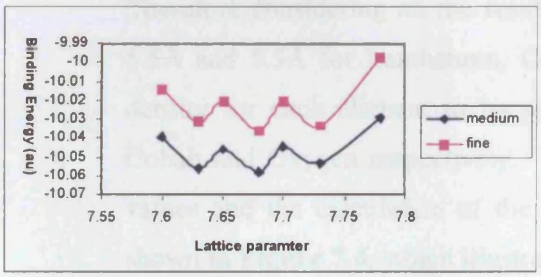

(b)

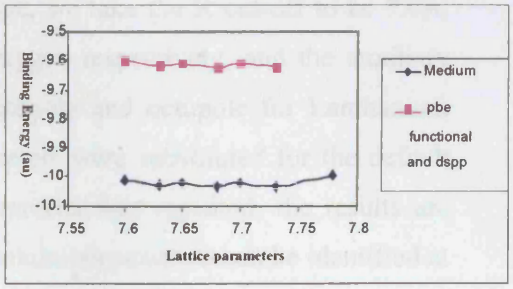

(c)

Figure 7.2 *To identify the minimum structure (a) lattice parameters were increased from 7.60Å-7.79Å(b) The integration grid was changed from medium to fine (c) The functional was changed to PBE and a pseudopotential (dspp) was added.*

However, **Figure 7.2** shows that adjusting the different parameters given above did not solve the problem. Therefore, finally, the R cut-off and auxiliary densities were adjusted. The former is applied when there are a large number of interatomic interactions, which are truncated at the value of the specified R cut-off. In $DMol^3$ the default R cut-off is 5.5Å. The R cut-off for each element, and then for each pair of ions was considered which showed that the best cut-off for La, Co, O ions was 7.0Å, 5.5Å and 5.5Å respectively. However, adjusting the cut-off still did not give a well-defined energy minimum; therefore the auxiliary densities for each element were considered. The latter distributes the charge density of an element, which can be calculated depending on the angular momentum (*l*) of the basis set. (n.b. typically a value of *l* one greater than in the basis set gives a good precision for the auxiliary distribution)[2]. In $DMol^3$ the default auxiliary density is an octupole. The hexadecapole and User 5 auxiliary densities use a higher level of electron distribution, which distributes the electron in further directions. A few of the basic auxiliary densities are shown in **Figure 7.3**

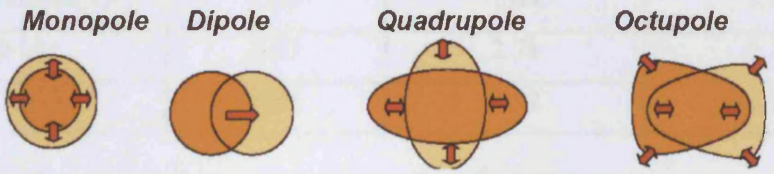

Figure 7.3 *Auxiliary densities for monopole, dipole, quadrupole and octupole*[2].

Therefore considering all the results given above, we take the R cut-off to be 7.0Å, 5.5Å and 5.5Å for Lanthanum, Cobalt and Oxygen respectively, and the auxiliary density for each element to be user 5, hexdecapole and octupole for Lanthanum, Cobalt and Oxygen respectively. There parameters were substituted for the default values and the calculation of the unit cell parameter was repeated; the results are shown in **Figure 7.4**, which illustrates that the minimum structure can be identified at 7.68Å. Experimentally it has been shown that the most favoured structure has a lattice parameter of 7.64Å. Therefore our computational data compares well with the experimental data[3]. There is also a good agreement with lattice energy calculations employing GULP as shown in **Table 7.1**.

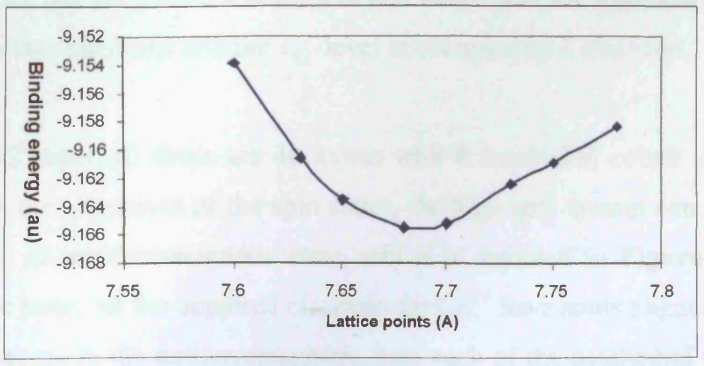

Figure 7.4 *The binding energy data for lattice parameters from 7.60Å-7.78Å*

	DMol^3	GULP	Exp
Lattice Parameter (Å)	7.68	7.64	7.64
La-O (Å)	2.67	2.71	2.70
Co-O (Å)	1.91	1.92	1.91

Table 7.1 *Comparisons of bond lengths of DMol^3, GULP and experimental work*[3]

7.2 Results for Bulk Calculations

After identifying the energy minimum structure of $LaCoO_3$, we need to determine which electronic spin state is most favoured. For $LaCoO_3$ there are three possible states for the Co^{3+} ion in the octahedral site: (1) low spin (LS) diamagnetic ($t_{2g}^6 e_g^0$), (2) intermediate spin (IS) paramagnetic ($t_{2g}^5 e_g^1$) (3) high spin (HS) paramagnetic ($t_{2g}^4 e_g^2$). The ground state of $LaCoO_3$ is known to have a low spin state at low temperatures and a mixed state of high and low spins at higher temperatures. In the low spin state the t_{2g} levels are fully occupied by six electrons and the e_g level is empty. The intermediate state, is where only one electron has been transferred from the t_{2g} to the e_g, has not been considered in this thesis. For the high spin Co^{3+} ion, the e_g is filled by two electrons and the t_{2g} level is occupied by 4 electrons.

For the 2x2x2 supercell there are 40 atoms with 8 octahedral cobalt atoms. Now, depending on the alignment of the spin states, the high spin system can have either a ferromagnetic or antiferromagnetic state, which is depicted in **Figure 7.5**. In the ferromagnetic state, all the unpaired electrons for Co^{3+} have spins aligned in the same direction, whereas in the antiferromagnetic state each of the octahedral Co^{3+} have an opposite alignment of spin to its neighbour.

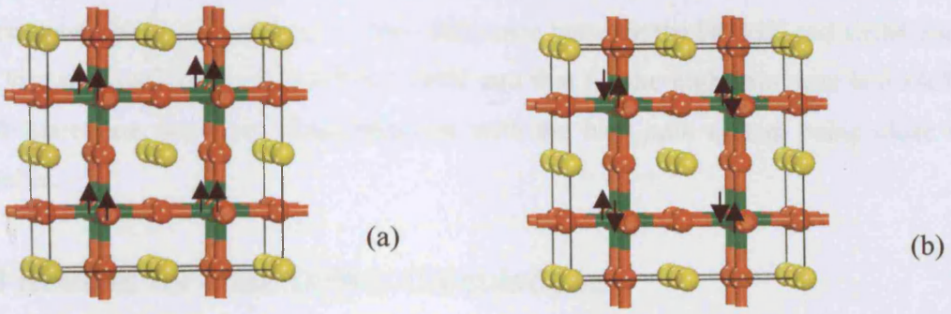

Figure 7.5 *(a) Ferromagnetic and (b) Antiferromagnetic states of $LaCoO_3$ where ↑ is the spin of the unpaired electrons*

For the low spin state, both spin restricted and unrestricted calculations were carried out. In spin restricted calculations the same orbitals are used for the alpha and beta electrons. In spin unrestricted calculations different orbitals are used for each electron. For closed shell systems, spin restricted calculations are used and for open shell systems, spin unrestricted calculations are employed. For the high spin state, only the unrestricted spin calculation can be considered. Low spin $LaCoO_3$ is of course, diamagnetic and has only one configuration, but, as noted, for the high spin system, two calculations are needed, i.e. for the ferromagnetic and antiferromagnetic states. The results for all the calculations are given in **Table 7.2**.

	Unrestricted binding energy (au)
LOW SPIN	-9.167
HIGH SPIN (Ferromagnetic)	-8.895
HIGH SPIN (Antiferromagnetic)	-8.783

Table 7.2 Results *for the Low and High spin states of $LaCoO_3$*

The results in **Table 7.2** show that the low spin state calculation is favoured compared to the high spin state calculations. For the high spin calculations, the ferromagnetic state is slightly more favoured compared to the antiferromagnetic state.

Information on the electronic properties of the perovksite material can be obtained by comparing the energy differences between the highest occupied molecular orbital (HOMO) and the lowest unoccupied molecular orbital (LUMO). A large difference

would indicate that the material would be an insulator and a small difference corresponds to a semi-conductor. The difference between the HOMO and LUMO for the low spin $LaCoO_3$ considered is 1.49eV and that for the high spin state is 0.34eV. Both states are therefore semiconductors with the high spin system being close to metallic.

7.3 Results for Bulk Defect Calculations

As discussed in **Section 2.3**, the oxygen vacancy plays a key role in oxidation catalysis. When an oxygen vacancy is created by abstraction of an oxygen atom, two electrons can remain in the crystal. There are three different possibilities for these electrons: (1) they can go in the conduction band; (2) an F centre can be created (where the electrons remain localised in the vacancy) (3) the electrons can be localised on the nearest cobalt creating a Co^{2+} ion. Our DFT calculations give insight into this problem. The calculations were performed for the lowest energy structure with the lattice parameter of 7.68Å, which was identified in **Section 7.1**. The calculations were initialized assuming that the electrons moved to the closest cobalt ions which are thereby reduced to Co^{2+} and which can have a low spin (LS) and high spin (HS) configuration i.e. configuration ($t_{2g}^6 e_g^1$ with one unpaired spin) and ($t_{2g}^5 e_g^2$ with three unpaired spins). Therefore as with the bulk calculations, ferromagnetic and antiferromagnetic configurations are possible. The ferromagnetic state of the low spin configuration has two unpaired electrons per unit cell while the antiferromagnetic state has a net spin of zero. In the same way, for the high spin ferromagnetic state, there will be six unpaired electrons, while the antiferromagnetic state will be zero spin. The other Co^{3+} ions in the supercell were considered to have the low spin configuration. For each of the above spin states, unrestricted calculations have been carried out.

The values reported below refer to the reaction to create an oxygen vacancy in the $LaCoO_3$, which is given as follows:

$$LaCoO_3 \rightarrow LaCoO_{3-\lambda} + V_O^{\bullet\bullet} + 2e' + \tfrac{1}{2}O_2 \qquad (7.1)$$

The energy to create an oxygen vacancy from (7.1) can then be calculated as:

$$E_{DEF} = (E_{NON-STOICH} + E_{1/2D_{O_2}}) - E_{CRY} \tag{7.2}$$

where E_{DEF} = Defect energy for creation of oxygen vacancy

$E_{NON-STOICH}$ = Energy of non-stoichiomeric structure

$1/2\,E_{DO_2}$ =Half Dissociation energy of oxygen

E_{CRY} = Energy of pure crystal

We note that equation (7.2) includes the binding dissociation energy of oxygen (-0.123au), which is calculated using the DMol[3] code with similar settings as for the bulk and defect calculations. The defect energy for creating the oxygen vacancy can be calculated using equation (7.2) and the lattice non-stoichiometric defect binding energies from **Tables 7.3.** All the results have been tabulated in **Table 7.4**; the binding energy for the perfect lattice was –9.167au.

	Non-stoichiometric lattice binding energy (au)
LOW SPIN	
Ferromagnetic (2)	-8.916
Antiferromagnetic (0)	-8.921
HIGH SPIN	
Ferromagnetic (6)	-8.927
Antiferromagnetic (0)	-8.919

Table 7.3 *Non-stoichiometric lattice binding energies.*

	Unrestricted (eV)
LOW SPIN	
Ferromagnetic (2)	3.41
Antiferromagnetic (0)	3.33
HIGH SPIN	
Ferromagnetic (6)	3.17
Antiferromagnetic (0)	3.38

Table 7.4 *Defect energies to create an oxygen vacancy*

Overall **Table 7.4** shows that the high spin ferromagnetic state (3.17eV) is the most favoured structure, although the energy differences between the different configurations are small. However, the results suggest that there is some coupling between the spins on the two Co^{2+} ions. We now address the question of the distribution of the two "excess" electrons on creation of the vacancies. To investigate the problem by direct calculation of the charge in the electron density map problematic. A simpler (if less precise) procedure is to employ a Mulliken population analysis, which gives an approximate charge on each individual element in the $LaCoO_3$ structure. Therefore, initially, we need to take the Mulliken charge analysis for the $LaCoO_3$ structure without the defect, from which we subtract from the charges shown in the calculation on the defective crystal. The results are displayed diagrammatically in **Figure 7.6**, where the greater the negative charge excess the larger and darker are the balls. The figure refers to the lowest energy high spin ferromagnetic state.

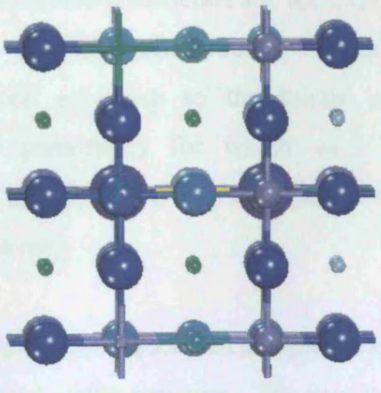

Spin 6

Figure 7.6 *Schematic diagram of the electron distribution when the electrons reduce* Co^{3+} *to* Co^{2+}

Figure 7.6 shows that for the high spin (6) ferromagnetic arrangement the electrons are distributed more towards the closest cobalt ions.

We note that our calculations do not permit us to investigate 'F centre' like configuration (which would require us to include basis functions of the vacancy site).

Such configurations are, however, unlikely in this system, which contains readily reducible Co^{3+} ions.

Although there are no data with which to make a direct comparison, the value of the calculated defect energies are reasonable. They will be reduced after relaxation is included. However, owing to technical difficulties with the DMol^3 code, such calculations were not possible during the course of this work, and will need to be investigated in future studies.

7.4 Summary and Conclusions

Previously, in **Chapters 4, 5** and **6,** atomistic methods have been employed for the $LaCoO_3$ structure. These chapters did not give information regarding the electronic properties of the structure. Therefore, in this chapter, quantum mechanical methods were employed using Density Functional Theory, which has been discussed in **Sections 3.3**. Initially, the lattice parameters for the 2x2x2 supercell were manually adjusted to determine the most favoured structure. We found that the R cut-off and auxiliary densities required adjusting so the lowest energy structure could be identified, the structural parameters for which were in good agreement with experiment as shown in **Table 7.1**. We also showed that for the bulk system the low spin state has the lowest energy.

Following the bulk calculations, defect calculations were carried out by creating oxygen vacancies in the most stable structure. The results for the defect calculations in **Table 7.4** show that the lowest energy structure has the antiferromagnetic spin state for the low spin and ferromagnetic for the high spin. As the high spin ferromagnetic state has the lowest energy it was considered in more detail. The Mulliken analysis was then used to investigate the charge redistribution as shown in **Figure 7.6** which illustrates that for the high spin state the electrons are localised on the closest two Co ions.

The calculations reported here represent a useful initial study. Future work may find it necessary to explore other techniques and codes.

REFERENCES

(1) Accelrys.Inc. DMol^3 program, 1999.
(2) P.W.Atkins *"Physical Chemistry"*, 4th ed.; Oxford University Press, 1994.
(3) M.Cherry; M.S.Islam; C.R.A.Catlow. *J. Solid State Chem.* **1995**, *125*, 118.

CHAPTER 8

8. OVERVIEW AND FUTURE WORK

In this thesis, atomistic and quantum mechanical simulation techniques have been applied to investigate defect structures for one of the most important catalytically active perovskites, $LaCoO_3$. Oxygen vacancies in $LaCoO_3$ have shown to play a key role in oxygen adsorption and oxygen isotopic exchange and are considered to strongly influence catalytic oxidation performance. Therefore, the defect calculations presented here involve the creation of oxygen vacancies by two methods, (1) doping Sr^{2+} at the La site and (2) reduction of Co^{3+} to Co^{2+}. Other calculations have involved the solution of Ce^{4+} as it has been shown experimentally that doping $LaCoO_3$ enhances catalytic oxidation performance for both methane combustion and ammonia oxidation although the degree of solubility is apparently low. Four reactions have been considered for cerium doping, the first two of which initially assume a stoichiometric host $LaCoO_3$ lattice, where (1) the substitution of Ce^{4+} for La^{3+} is compensated either by creation of La^{3+} vacancies or (2) reduction of Co^{3+} to Co^{2+}. In the third case (3), cerium is doped into the reductively non-stoichiometric $LaCoO_3$ lattice containing oxygen vacancies, resulting in filling those vacancies. Finally in the fourth case (4), co-doping Sr^{2+} and Ce^{4+} at La sites was carried out in $LaCoO_3$. These calculations have been carried out to determine the most favoured compensating defect process for Ce solution.

Atomistic methods have been used for all the initial bulk defect and surface calculations. The GULP code was employed for the treatment of the bulk defective structure and the MARVIN code for the surface defect calculations. Two different approaches have been used to calculate the defect energies in bulk $LaCoO_3$ employing the GULP code, the supercell method and the Mott Littleton method representing the concentrated and dilute cases respectively, with the aim of determining the factors, which could affect the ease of creation of oxygen vacancies or the solubility of cerium in $LaCoO_3$.

The results for the supercell method for creating the oxygen vacancies and for Ce^{4+} doping show that the stability of the structure may not only depend on the nearest neighbour Columbic interactions but also on interactions between defect clusters. These interactions can be best visualised by creating an effective charge model for the given reactions showing all the interactions between the defects. In contrast, for the Mott Littleton method it has been shown, in most cases that, for the various reactions for creating the oxygen vacancies and for Ce^{4+} doping, interactions between nearest neighbours in a defect cluster according to Coulomb's law determine stability. Therefore, as the distances between individual defects in a cluster are increased, the stability of the structure is decreased. An important exception to this simple view is the case of doping Ce^{4+} into non-stoichiometric $LaCoO_3$ resulting in filling of oxygen vacancies. The most favoured case is where the filled oxygen site is stabilised by the highly oxidised Ce^{4+} nearest neighbours while the reduced Co^{2+} cations are further away. In addition, the calculations have confirmed that Ce is not very soluble in bulk stoichiometric $LaCoO_3$ but is more soluble in the non-stoichiometric material resulting in filling oxygen vacancies.

However, catalysis is normally considered to be largely a surface process although in the case of perovskite oxides, sub-surface processes in relation to oxygen availability for intrafacial catalysis are also important. Therefore surface computational simulations have been carried out employing the MARVIN code to investigate the creation of oxygen vacancies and the solubility of Ce^{4+} at the surface of $LaCoO_3$. The calculations presented in this thesis have used the low index surface terminations, i.e. (100), (110) and (111), for stoichiometric $LaCoO_3$.

The calculations for creating oxygen vacancies via Sr doping or reduction of Co^{3+} at the surface for the (100), (110) and (111) planes showed that the surface stability is higher when there is a close separation between defects of opposite charge as would be expected on simple electrostatic grounds. Moreover, the results also showed that in many cases there is a strong driving force for surface segregation of oxygen vacancies. However, the factors controlling surface stability are complex, as noted in several cases, e.g. the (110)LaOCo surface, where the coordination chemistry of cobalt drives extensive surface reconstruction.

For materials containing oxygen vacancies, the results clearly confirm that the presence of defects strongly influences crystal morphology and surface chemistry. Therefore for creation of oxygen vacancies coupled with Sr doping it appears that the relaxed (110)O terminated surface alone becomes energetically favoured and for creation of oxygen vacancies by reduction of Co^{3+} to Co^{2+}, the calculations show that the (100)OCoO terminated and (110)O terminated planes have the lowest surface energies. These results contrast with stoichiometric $LaCoO_3$ where the (110)O and (100)OLa terminated surfaces dominate.

These crystal surfaces can then be distinguished regarding their intrafacial activity in terms of the ease of creating oxygen vacancies. For Sr^{2+} doped $LaCoO_3$ the situation is simpler since the (110)O terminated surface is predicted to dominate the crystal morphology and the energy for creating oxygen vacancies is relatively low. For as prepared, undoped reductively non-stoichiometric $LaCoO_3$, which is predicted to display (110)O terminated and (100)OCoO terminated surfaces, the latter is most likely to dominate intrafacial activity since creation of vacancies is energetically highly favoured.

Similar calculations have been carried out to determine the solubility of Ce at the surface for the (100)OLa, (100)OCoO and (110)O terminated surfaces. Computational modelling has shown that Ce is more soluble at the surface for stoichiometric $LaCoO_3$ compared to the bulk. It can be seen for the La vacancy reaction that the (100)OLa terminated surface will be the most energetically favoured, and for the Co^{3+} reduction reaction, the (100)OCoO termination is slightly more favoured compared to the other terminations. The calculation for dissolution of Ce in non-stoichiometric $LaCoO_3$ surfaces shows that the (110)O termination is the most favoured. These terminations can be visualised in the crystal morphology. Furthermore, the results have highlighted that the possibility of controlling morphology through selective creation of surface defects by doping.

A model for Ce doped $LaCoO_3$ particles produced by a typical route involving precipitation and air calcination at ~900°C has been proposed consisting of 50nm crystallites with a Ce enriched surface layer extending into the subsurface. In this

model, Ce^{4+} is compensated by reduction of Co^{3+}under air calcination. A comparison with undoped material prepared under similar conditions indicates enhanced high temperature, intrafacial catalytic oxidation in the presence of Ce dopant but decreased low temperature, suprafacial activity in agreement with experiment. This conclusion represents a substantial advance in our understanding of the role of the Ce dopant. We should note that catalytic behaviour of Ce is likely to depend on preparative conditions such as temperature and oxygen partial pressure, which influence crystallinity, oxygen non-stoichiometry and defect compensation processes. It is predicted that the material produced by calcination under pure oxygen would show enhanced intrafacial oxidation activity.

The atomistic methods, which have been employed for the $LaCoO_3$ structural simulations discussed above, do not give information regarding the electronic properties of the structure. Therefore, in a preliminary study of bulk material, DFT quantum mechanical methods have been employed using DMol[3] for a 2x2x2 supercell model. The structural parameters for the best structure derived by adjusting the R cut -off were in good agreement with experiment giving a lattice a parameter of 7.68Å. The low spin state was shown to be more favoured compared to the high spin state.

Following the stoichiometric calculations, defect calculations were carried out by creating oxygen vacancies in the most stable structure. The results for the defect calculations show that the most favoured structure is the ferromagnetic spin state for the high spin. To get a better visualisation of the electronic charge distribution a Mulliken analysis was carried out which showed that, for the high spin, the electrons are distributed more towards the Co, i.e. reduction, and, for low spin, the electrons are distributed towards the closest oxygens.

The work presented above has made a number of predictions, which require discussion and verification experimentally. In the case of oxygen vacancy creation the computational studies here confirm surface science experimental results for Sr doping but no such verification exists for undoped, reductively non-stoichiometric $LaCoO_3$. Such a study would require extremely precise XPS measurements to distinguish perhaps low levels of Co^{2+} in the presence of Co^{3+}[1]. In addition, careful consideration of the surface preparation in terms of the effect of adsorbed oxygen as

discussed by Kaliaguine *et al* would be required[2]. Before embarking on such an experimental programme, further computational work would be desirable using QM as for bulk $LaCoO_3$ to examine electron distribution effects.

In the case of Ce doping, verification of a surface enriched layer would require careful, low concentration level doping experiments combined with sensitive XPS or LEIS measurements as in the work on doped ZrO_2 by Brongersma *et al*[3]. A major complication here is the low solubility of Ce and its propensitivity to segregate to give a multi-phase preparation. As a control, high resolution, analytical TEM, equipped with energy dispersive X-ray analysis (EDXA) or electron energy loss spectroscopy (EELS) would be required as illustrated by the work of Shannon[4]. These are not trivial experiments, hence the importance of the computer simulations. This comment applies also, to confirming the changes in crystal morphology for real preparations of defect containing materials.

In terms of the computational studies themselves a number of aspects require further amplification. For example, in the study investigating bulk defects in **Chapter 4**, the supercell calculations could be extended by employing a greater supercell size, (3x3x3) and (4x4x4) so that the defect interactions would have less effect and a more accurate result could be obtained. Furthermore, the radial distribution factor could be employed as a more accurate way of analysing the defect interactions at different distances. Similarly, in the case of the atomistic surface simulations in **Chapter 5** and **6**, choice of a larger two-dimensional surface repeat than 2x1 would reduce effects due to the long range defect cluster interactions.

For the QM bulk defect calculations in **Chapter 7**, a better representation for the distribution of the electrons can be achieved by plotting the electron densities. This was not possible with DMol here possibly due to the due to the level of DFT imposed in the calculation. Therefore the calculation may need to be repeated employing an alternative package such as CRYSTAL.

The work discussed in this thesis provides an excellent basis for further computational investigation, most importantly to study the behaviour of oxygen at $LaCoO_3$ surfaces, which will require QM calculations. Following on from bulk calculations in **Chapter**

7, surface calculations using a slab model need to be carried out to derive a QM representation of stoichiometric and oxygen vacancy containing $LaCoO_3$ surfaces, taking the atomistic simulations in **Chapter 5** as a staring point. Oxygen adsorption can then be considered in relation to confirming the importance of oxygen vacancies, identifying the electronic state of the most stable adsorbed oxygen species and investigating the role of Co in terms of influencing the adsorption process and the resultant distribution of electrons.

The best approach would be to employ the quantum mechanical/molecular mechanical (QM/MM) method as illustrated by the work of French *et al*[5]. In the QM/MM model the atoms are partitioned into two regions as in **Figure 8.1**. An electronically important region consisting of relatively few atoms and containing the adsorption defect site, which is treated by QM is embedded in a larger number of ions which can be treated classically. In addition to studying the behaviour of oxygen, such a model could be extended to investigate the mode of activation of molecules such as CH_4 and NH_3 over oxide surfaces.

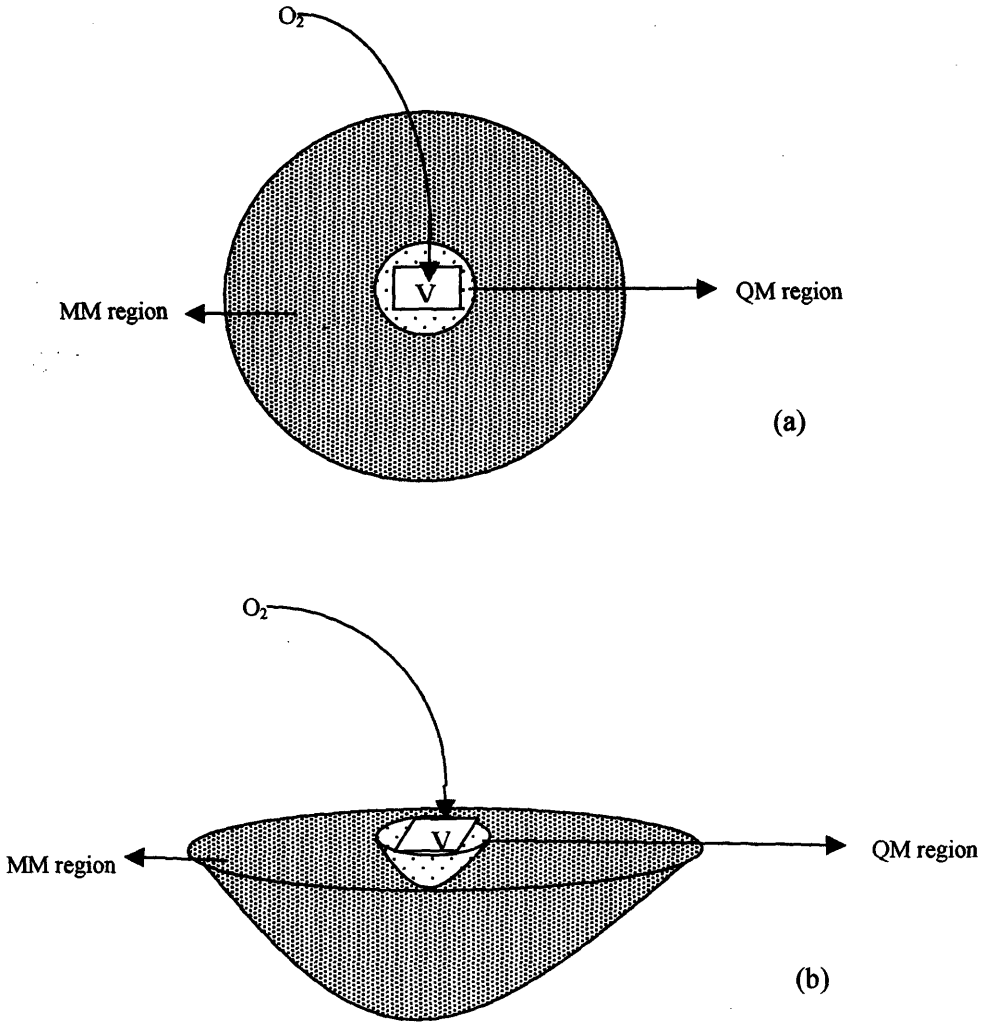

Figure 8.1 *Schematic diagrams showing the quantum mechanical and molecular mechanical regions for a QM/MM system (a) top view (b) side view*

REFERENCES

(1) W.R.Flavell; A.G.Thomas; J.Hollingworth; S.Warren; S.C.Gna; P.M.Dunwoody; C.E.J.Mitchell; P.G.D.Marr; D.Techan; S.Downes; E.H.Seddon; V.R.Dhanak; K.Asai; K.Koboyashi; N.Yamada. *Faraday Disc* **1999**, *114*, 407.

(2) S.Kaliaguine; AVan.Neste; V.Szabo; J.E.Gallot; M.Bassir; R.Muzychik. **2000**, *209*, 345.

(3) M.DeRidder; A.G.J.Vervoort; R.G.VanWelzenis; H.H.Brongessma. *Solid State Ionics* **2003**, *158*, 67.

(4) M.D.Shannon. Johnson Matthey Symposium on Catalyst Technology 2005, Nottingham.

(5) S.A.French; A.A.Sokol; S.T.Bromley. *Topics in Catalysis* **2003**, *24*, 161.

APPENDIX 1-

Comparison of $LaCoO_3$ particles prepared by Johnson Matthey with literature data

For the purpose of estimating surface area and crystallite size for industrially prepared material ex Johnson Matthey (JM), literature data was taken from Royer *et al*[1] as shown below in **Table 1** where the theoretical surface area is derived from the XRD size data and the BET crystallite size is derived from the BET surface area aauming spherical particles[1]:

Calcination temp.	Theoretical area (m^2/gm)	BET(m^2/gm)	Theoretical area/ BET
700°C-Royer *et al*	25.6	3.5	7.3
900°C-JM	16.8	1.18	14.2
1000°C-Royer *et al*	11.1	0.4	27.8

(a)

Calcination temp.	XRD(nm)	BETsize (nm)
700°C-Royer *et al*	32	235
900°C-JM	48.7	691.5
1000°C-Royer *et al*	74	2058

(b)

Table 1 *Comparison of JM data and with Royer et al (a) Surface area (b) Crystallite size.*

In **Table 1** the ratio of the theoretical area to the BET area increases with temperature since the calcinations temperature governs the degree of inter crystallite contact.

1A. Calculation of the volume of the first unit cell layer in a particle

This calculation assumes the crystallite size for JM material, which is 48.7 nm as derived above, with a theoretical surface area of 16.8 m^2/gm. The unit cell size is assumed to be 4Å.

[1] S.Royer; D.Duprez; S.Kaliaguine. *Journal of Catalysis* **2005**, *234*, 364

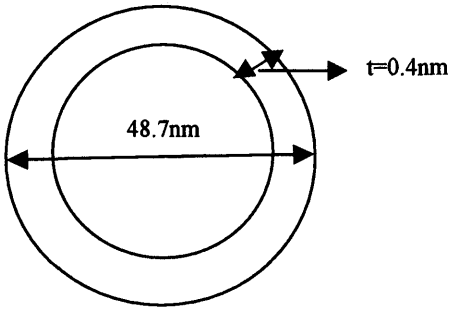

Figure 1. *Schematic diagram of a JM particle with diameter 48.7nm and surface layer 0.4nm thick.*

Volume of particle = $\frac{4}{3}\pi r^3$

Volume of surface layer = $4\pi r^2 t$

% volume = $\frac{4\pi r^2 t \times 3}{4\pi r^3} \text{x}100 = 300\frac{t}{r}$

$= \frac{300 \times 0.4}{24.35}$ =4.93% by volume

Therefore the volume occupied by the surface layer is ~5%.

1B. Calculation of the volume fraction as a function of thickness of a surface as shown below.

$$V = \frac{4\pi r^3}{3}$$

$$V_b = \frac{4\pi(r-t)^3}{3}$$

$$\frac{V_b}{V} = \frac{(r-t)^3}{r^3} = (1-\frac{t}{r})^3$$

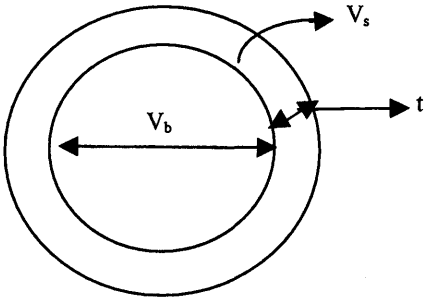

Figure 2 *Schematic diagram showing the surface volume fraction V_s and the bulk volume V_b*

Unit cell layer	t (nm)	V_b(%)	V_s (%)
1	0.4	95.2	4.8
2	0.8	90.5	9.5
3	1.2	85.9	14.1
4	1.6	81.6	18.4
5	2.0	77.3	22.7
10	4.0	58.4	41.6

Table 2 *Comparison of volume fraction of the surface as a function ofthickness of a surface*

APPENDIX 2

Estimate of fraction of Ce surface dopant levels in the MARVIN calculations

In **Chapter 6**, different reactions have been considered for cerium doping at the surface, the first which assumes a stoichiometric host $LaCoO_3$ lattice, where the substitution of Ce^{4+} for La^{3+} is compensated by creation of La^{3+} vacancies as shown:

$$3CeO_2 + 4La_{La}^{x} \rightarrow 3Ce_{La}^{\bullet} + V_{La}^{'''} + 2La_2O_3 \qquad (6.1)$$

The second method is where the substitution of $Ce^{4+}$is compensated by reduction of Co^{3+} to Co^{2+} as shown:

$$4CeO_2 + 4La_{La}^{x} + 4Co_{Co}^{x} \rightarrow 4Ce_{La}^{\bullet} + 4h_{Co}^{'} + 2La_2O_3 + O_2 \qquad (6.2)$$

A third case is also considered where cerium is doped into the $LaCoO_3$ lattice containing oxygen vacancies, resulting in filling of those vacancies according to the equation:

$$2La_{La}^{x} + 2CeO_2 + V_O^{\bullet\bullet} \rightarrow 2Ce_{La}^{\bullet} + La_2O_3 + O_O^{x} \qquad (6.3)$$

In order to estimate the surface Ce dopant levels used in the MARVIN calculations a simple geometric view of the (2x1) surface block was considered as in **Figure 3**.

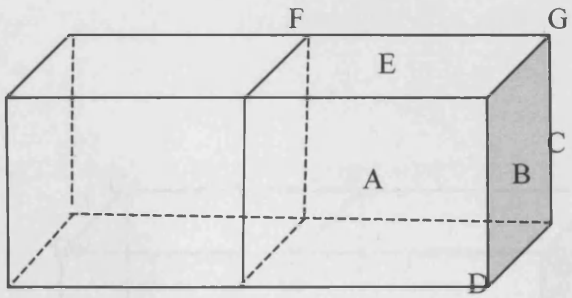

Figure 3 *Schematic diagram of a (2x1) surface cell.*

The different labelling in **Figure 3** corresponds to the face, edge, corner and body sites for the exposed face and subsurface of the outermost unit cell. **Table 3** presents the weighting of these sites in calculating the number of atoms in the surface unit cell.

Site	Sub surface	Exposed surface
Body	A-1	-
Face	B-1/2	E-1
Edge	C-1/4	F-1/2
Corner	D-1/8	G-1/4

Table 3 Weightings *of the different lattice sites in the surface block*

It is important to note that **Figure 3** is highly idealised and in each case more than one defect configuration maybe possible. In any case a real material will display 'roughness' on a number of length scales. It is also important to remember that MARVIN will reproduce the occupancy of the defect sites in the 2x1 block in a 2D symmetric manner.

2A. Cerium doping and lanthanum vacancies

According to equation (6.1) above, substitution of three Ce^{4+} ions at La^{3+} sites results in the creation of one lanthanum vacancy in order to maintain a charge balance. In this case, since there is only one La site per lattice unit cell, the doping needs to extend below the outermost surfaces unit cell. A schematic diagram

of the disposition of the cerium and lanthanum vacancy sites is shown below in **Figure 4**.

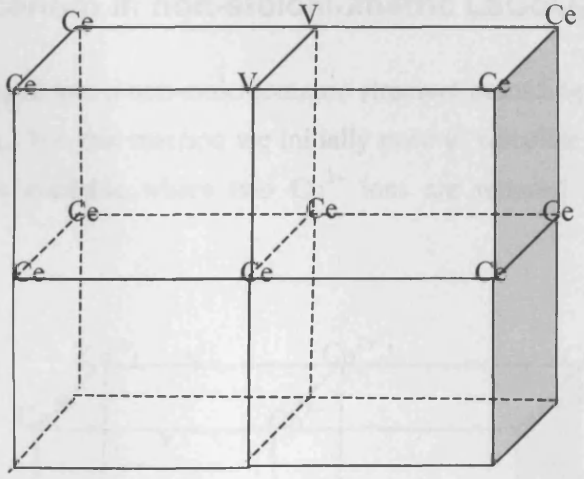

Figure 4 *Schematic diagram showing the positions for the cerium dopant/lanthanum vacancy reaction.*

Taking the weightings in **Table 3** gives a Ce: La vacancy ratio of 3 with all of the La sites in the outer unit cell replaced by substituted Ce or cation vacancies.

2B. Cerium doping and reduction of Co^{3+}

The second reaction for the dissolution of Ce in stoichiometric $LaCoO_3$ involves reduction of one Co^{3+} to Co^{2+} for each Ce^{4+} substituted at a La^{3+} site as in equation (6.2). The doping of cerium and reduction of Co^{3+} can be shown below in **Figure 5**:

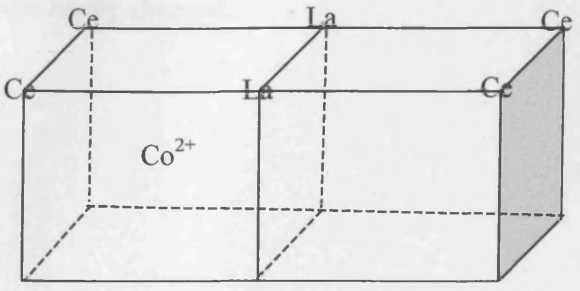

Figure 5 *Schematic diagram showing the positions for the cerium dopant/ Co^{3+} reduction reaction.*

Taking the weightings in **Table 3** the percentage of substituted La sites is 33% and the Co^{2+}: Ce^{4+} ratio equals unity.

2C. Doping cerium in non-stoichiometric $LaCoO_3$ surfaces

Cerium can be doped into a non-stoichiometric structure according to (6.3) by filling oxygen vacancies. For this reaction we initially need to calculate the percentage of oxygen vacancies available where two Co^{3+} ions are reduced for each vacancy created:

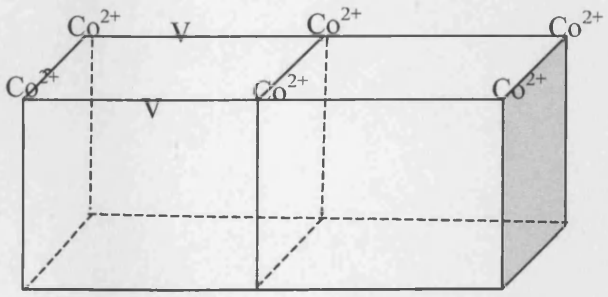

Figure 6 *Schematic diagram showing the positions for the reduction of* Co^{3+} *and oxygen vacancy creation reaction.*

The schematic diagram in **Figure 6** shows the reduced Co^{2+} ions and oxygen vacancy at the exposed surface giving a fraction of oxygen vacancies compared to the total number of anion sites of 12.5% and a Co^{2+}: vacancy ratio of 2. An alternative configuration puts the defects within the body of the surface unit cell but the vacancy fraction at 14% is hardly changed.